

Applied Research Laboratory

Technical Report

AN EXPERIMENTAL EVALUATION OF THE
INTERNAL FLOW FIELD OF AN AUTOMOTIVE HEATING,
VENTILATING AND AIR CONDITIONING SYSTEM

by

G.R. Denger
M.W. McBride
G.C. Lauchle

AD-A227 435

DTIC

ELECTE

OCT 04 1990

S

E

D

PENNSTATE



DISTRIBUTION STATEMENT A

Approved for public release;
Distribution Unlimited

①

The Pennsylvania State University
APPLIED RESEARCH LABORATORY
P.O. Box 30
State College, PA 16804

AN EXPERIMENTAL EVALUATION OF THE
INTERNAL FLOW FIELD OF AN AUTOMOTIVE HEATING,
VENTILATING AND AIR CONDITIONING SYSTEM

by

G.R. Denger
M.W. McBride
G.C. Lauchle



Technical Report No. TR 90-011
July 1990

Accession For	
NTIS CRA&I	<input checked="" type="checkbox"/>
DTIC TAB	<input checked="" type="checkbox"/>
Unannounced	<input type="checkbox"/>
Justification	
By _____	
Distribution/	
Availability Codes	
Dist	Avail and/or Special
A-1	

Supported by:
Ford Motor Company

L.R. Heutche, Director
Applied Research Laboratory

Approved for public release; distribution unlimited

DTIC
ELECTE
OCT 04 1990
S E D

ABSTRACT

↘ A diagnostic study of the internal flow field of a typical automotive heating, ventilation and air conditioning system (HVAC) was conducted. This study consisted of four primary experiments designed to provide a fairly complete description of the governing flow mechanisms. These efforts were aimed at determining the flow paths and sources of inefficiency within the ductwork, as well as identifying possible flow-induced noise sources. Because the root of system inefficiency and noise is the Forward Curved (FC) centrifugal blower, emphasis was placed on determining the blade passage and volute flow of this unit. The goal of this thesis is to present information which may aid in the future design of automotive HVAC systems. *KEYWORDS: AUTOMOTIVE VEHICLES; AIR CONDITIONING EQUIPMENT; HEATING; VENTILATION. (RH)*

↑ This study has shown the internal flow field of a typical HVAC system to contain large separation and stagnant flow zones, turbulent shear layers, and highly inefficient blower performance. It was found that blower performance was significantly affected by the inlet flow condition. Analysis of the data suggests that the bulk of kinetic energy transfer occurs near the root of the impeller blades, while the inlet side of the blades operate inefficiently. This indicates that impeller blades experience large axial loading variations. In addition, the blades also undergo loading fluctuations as a function of circumferential location. Unsteady flow separation occurring over the blades' suction side may be

contributing to overall broadband noise generation and low performance. Visualization of the blower flow field showed extensive blade passage flow separation, re-entrant flow, rotating stall, and location-dependent blade loading.

Accession For	
NTIS GRA&I	<input checked="" type="checkbox"/>
DTIC TAB	<input type="checkbox"/>
Unannounced	<input type="checkbox"/>
Justification	
By	
Distribution/	
Availability Codes	
Dist	Avail and/or Special
A-1	

TABLE OF CONTENTS

LIST OF FIGURES	viii
LIST OF TABLES	xii
NOMENCLATURE	xiii
ACKNOWLEDGMENTS	xvi
Chapter 1: GENERAL PROBLEM DESCRIPTION AND LITERATURE REVIEW	1
1.1 General Problem Description	1
1.2 Centrifugal Fan Noise Generation	6
1.2.1 Noise Mechanisms in Centrifugal Devices	7
1.2.2 Passive and Active Sound Cancellation	9
1.2.3 The Influence of Geometry on Noise Generation	11
1.3 Research Regarding the Fluid Dynamics of FC Blowers	12
1.3.1 Characterization of the FC Blower Flow Field	12
1.3.2 Variations on Centrifugal Blower Design	17
1.4 Thesis Organization and Overview	18
Chapter 2: EXPERIMENTAL METHODOLOGY	20
2.1 Equipment	20
2.1.1 Experimental Water Tank	20
2.1.2 Clear HVAC System	21
2.1.3 Prototype and Three-Times-Size Blower.	21
2.1.4 Illumination Method.	27
2.1.5 Image Processing Workstation	28

2.1.6 Optical-Mechanical Image Derotator	30
2.2 Flow Modelling Methods.	32
2.2.1 Clear HVAC System	32
2.2.2 Three-Times-Size Blower	34
Chapter 3: DATA ACQUISITION AND REDUCTION TECHNIQUES	37
3.1 Blower Performance.	37
3.2 Dye Visualization of the Internal HVAC Flow.	38
3.3 Particle Tracing Velocimetry (PTV)	40
3.3.1 Image Processing/Data Acquisition	40
3.3.2 Data Reduction	47
3.4 Visualization of the Blower Relative Flow	48
Chapter 4: RESULTS	51
4.1 Blower Performance	51
4.2 Dye Visualization of the Internal HVAC Flow	53
4.3 Velocity Flow Field in the Volute Casing	61
4.3.1 Absolute Velocity Field	61
4.3.2 Relative Velocity Field	73
4.4 Visualization of the Relative Flow Field	81
4.4.1 Fresh Inlet Mode	81
4.4.2 Recirc Inlet Mode	96
Chapter 5: CONCLUSIONS	112
5.1 Recommendations for Future Research	116
REFERENCES	118

Appendix A: UNCERTAINTY CONSIDERATIONS . . .	121
A.1 The Effect of Gravity on Velocity Measurements .	121
A.2 Particle Response Time.	122
A.3 Image Acquisition Error.	123
A.4 Image Processing Error.	123

LIST OF FIGURES

1.1	Volute Casing and Impeller (Reproduced from Osborne, [1])	4
1.2	Centrifugal Impeller Velocity Triangles (Reproduced from Osborne, [1])	5
1.3	Sketch of "Inactive" Flow Zone. . . .	13
2.1	Clear Experimental HVAC System	22
2.2	Prototype Blower	23
2.3	Prototype Blower Blade Detail	24
2.4	Front View of Three-Times-Size Blower	25
2.5	Side View of Three-Times-Size Blower	26
2.6	Optical Configuration	29
2.7	Image Processing Setup	31
2.8	Image Derotator Orientation	31
3.1	Data Acquisition Planes for Particle Tracing Velocimetry Experiment	39
3.2	Image Processing Algorithm Flow Chart	45
3.3	Data Reduction Flow Chart	49
4.1	Blower Performance Curves	52
4.2	Static Pressure Distribution at the Volute Wall as a Function of Angular Position from Cutoff. . . .	54
4.3	Sketch of Pathlines Traced by Dye Visualization Method, Blower Discharge	56
4.4	Sketch of Pathlines Traced by Dye Visualization Method, Downstream of Evaporator Core	57
4.5	Sketch of Pathlines Traced by Dye Visualization Method, Plenum Region	59

4.6	Sketch of Pathlines Traced by Dye Visualization Method, Transition Region	60
4.7	Velocity Vectors in Volute, $d/W = 0.186$ (a) Averaged Data (b) Interpolated Data.	64
4.8	Flow Visualization of Cutoff Region $d/W = 0.186$	65
4.9	Velocity Vectors in Volute, $d/W = 0.372$ (a) Averaged Data (b) Interpolated Data	66
4.10	Velocity Vectors in Volute, $d/W = 0.558$ (a) Averaged Data (b) Interpolated Data.	68
4.11	Velocity Vectors in Volute, $d/W = 0.744$ (a) Averaged Data (b) Interpolated Data	69
4.12	Velocity Vectors in Volute, $d/W = 0.930$ (a) Averaged Data (b) Interpolated Data	70
4.13	Tangential Velocity Profiles at $\theta = 320^\circ$	71
4.14	Radial Velocity Profiles at $\theta = 320^\circ$	72
4.15	Relative Velocity Vectors in Volute, $d/W = 0.186$ (a) Averaged Data (b) Interpolated Data	75
4.16	Relative Velocity Vectors in Volute, $d/W = 0.372$ (a) Averaged Data (b) Interpolated Data	77
4.17	Relative Velocity Vectors in Volute, $d/W = 0.558$ (a) Averaged Data (b) Interpolated Data	78
4.18	Relative Velocity Vectors in Volute, $d/W = 0.744$ (a) Averaged Data (b) Interpolated Data	79
4.19	Relative Velocity Vectors in Volute, $d/W = 0.930$ (a) Averaged Data (b) Interpolated Data	80
4.20	Visualization of the Cutoff Relative Flow Inlet Mode "fresh", $d/W = 0.186$	82
4.21	Visualization of the Relative Flow Inlet Mode "fresh", $d/W = 0.186$, $10^\circ < \theta < 150^\circ$	84
4.22	Visualization of the Relative Flow Inlet Mode "fresh", $d/W = 0.186$, $60^\circ < \theta < 200^\circ$	85

4.23	Visualization of the Relative Flow Inlet Mode "fresh", $d/W = 0.186$, $110^\circ < \theta < 250^\circ$	86
4.24	Visualization of the Relative Flow Inlet Mode "fresh", $d/W = 0.186$, $160^\circ < \theta < 300^\circ$	88
4.25	Visualization of the Relative Flow Inlet Mode "fresh", $d/W = 0.186$, $260^\circ < \theta < 40^\circ$	89
4.26	Visualization of the Cutoff Relative Flow Inlet Mode "fresh", $d/W = 0.372$	90
4.27	Visualization of the Relative Flow Inlet Mode "fresh", $d/W = 0.186$, $40^\circ < \theta < 180^\circ$	92
4.28	Visualization of the Relative Flow Inlet Mode "fresh", $d/W = 0.186$, $110^\circ < \theta < 250^\circ$	93
4.29	Visualization of the Relative Flow Inlet Mode "fresh", $d/W = 0.186$, $160^\circ < \theta < 300^\circ$	94
4.30	Visualization of the Relative Flow Inlet Mode "fresh", $d/W = 0.186$, $210^\circ < \theta < 350^\circ$	95
4.31	Visualization of the Cutoff Relative Flow, Inlet Mode: "recirc", $d/W = 0.186$, $10^\circ < \theta < 150^\circ$	97
4.32	Visualization of the Relative Flow, Inlet Mode: "recirc", $d/W = 0.186$, $90^\circ < \theta < 200^\circ$	98
4.33	Visualization of the Relative Flow, Inlet Mode: "recirc", $d/W = 0.186$, $200^\circ < \theta < 310^\circ$	100
4.34	Visualization of the Relative Flow, Inlet Mode: "recirc", $d/W = 0.186$, $270^\circ < \theta < 20^\circ$	101
4.35	Visualization of the Cutoff Relative Flow Inlet Mode: "recirc", $d/W = 0.372$	103
4.36	Visualization of the Relative Flow, Inlet Mode: "recirc", $d/W = 0.372$, $45^\circ < \theta < 180^\circ$	104
4.37	Visualization of the Relative Flow, Inlet Mode: "recirc", $d/W = 0.372$, $90^\circ < \theta < 220^\circ$	105
4.38	Visualization of the Relative Flow, Inlet Mode: "recirc", $d/W = 0.372$, $180^\circ < \theta < 325^\circ$	107

4.39	Visualization of the Discharge Relative Flow Inlet Mode: "recirc", $d/W = 0.372$, $90^\circ < \theta < 220^\circ$	108
4.40	Circumferential Variation of Incidence Angle Inlet Mode: "recirc"	110
4.41	Circumferential Variation of Incidence Angle Inlet Mode: "fresh"	111

LIST OF TABLES

2.1	Fan Dimensions and Operating Details	25
4.1	Average Vector Count and Standard Deviation Values for Data Reduction Cell Blocks	62

NOMENCLATURE

General:

Impeller, Fan, Blower:	A forward curved centrifugal blower
Volute, Casing, shroud:	Nautilus-shaped vaneless diffuser which encloses impeller.
Cutoff:	Point of closest approach of volute to impeller
Blade Passing Frequency: (BPF)	Tone generated by the jet-wake flow structure created by a rotating blade row which acts against the volute casing at the cutoff $BPF = \# \text{blades} * \text{rotation speed}$
Eye:	Area through which fluid is drawn into impeller
Exposure:	Linear distance from the cutoff to the lowest point of the impeller
Blower Discharge:	The point at which the volute attaches to the diffuser

Automotive HVAC System:

Diffuser:	The expansion region downstream of the discharge.
Evaporator Core:	The radiator-type cooling device which is placed at the downstream end of the diffuser
Transition zone:	The point in the system where the flow is directed into the plenum or down into the heater core cavity
Heater Core:	A radiator-type heating device
Plenum:	The zone downstream of the transition zone and heater core which collects the flow before discharge into the ductwork

Greek Symbols:

β	Blade Angle, <i>deg</i>
γ	Flow Incidence Angle, <i>deg</i>
ρ	Fluid Density, kg/m^3
ν	Fluid Kinematic Viscosity, m^2/s
μ	Fluid Absolute Viscosity, kg/ms
Ω	Impeller Angular Rate, rad/s
ϕ	Chapter 2: Flow Coefficient, $V_{\text{rad}}/V_{\text{tip}}$ Chapter 4: Flow Coefficient, $Q/A_{\text{inlet}}V_{\text{tip}}$
ψ	Chapter 2: System Head Coefficient, $2gH/V_{\text{tip}}^2$ Chapter 4: Fan Pressure Coefficient, $2P_{\text{tot}}/\rho V_{\text{tip}}^2$
η	Impeller Efficiency, $P_{\text{tot}}Q/T\Omega$
τ	Characteristic Time, <i>s</i>

English Symbols:

<i>d</i>	Distance from Inlet, <i>cm</i>
<i>u</i>	Velocity, <i>cm/s</i>
<i>v</i>	Velocity, <i>cm/s</i>
<i>w</i>	Relative Velocity, <i>cm/s</i>
<i>C</i>	Impeller Chord Length, <i>cm</i>
<i>D</i>	Impeller Diameter, <i>cm</i>
<i>E</i>	Error
<i>F</i>	Force, <i>N</i>
<i>H</i>	Head Rise or Loss, <i>cm</i>
<i>P</i>	Pressure, <i>Pa</i>

T	Torque, cm-g
V	Velocity, cm/s
W	Total Width of Volute Casing, cm

Subscripts:

1	At Blade Inlet
2	At Blade Exit
B	Buoyancy
D	Drag
G	Gravity
rad	Radial
rel	Relative
stat	Static
tan	Tangential
tip	Tip of Impeller Blades
tot	Total
term	Terminal

Chapter 1:

GENERAL PROBLEM DESCRIPTION AND LITERATURE REVIEW

1.1 General Problem Description

The design of quiet and aerodynamically efficient heating, ventilating and air conditioning (HVAC) systems requires an understanding of the interaction between fluid flows and solid structures. For automotive applications, a range of volumetric flow rates is required as well as a high pressure, or head rise, in order to provide suitable flow conditions. When coupled with irregular geometries, this combination frequently results in an HVAC system in which high velocities occur. Consequently, a system's noise generation increases with fluid velocity as the tendency for turbulent, separated flow becomes greater. Previous research has indicated that one of the most prevalent noise sources in an air moving system is the interaction of fluid forces with the solid boundaries which guide the air flow [1]. In addition, flow separation, vortex shedding, and turbulent shear layers represent phenomena which create fluctuating pressure fields, and thus may be acoustic noise sources. These flow characteristics may also act to reduce overall performance. The following study is aimed at identifying poor flow areas within an automotive HVAC system, and

documenting the flow in a forward curved squirrel cage blower used to move the fluid. The ultimate goal of this work is to provide information to aid in the future designs of aerodynamically efficient and quiet systems.

In addition to aerodynamic and thermodynamic requirements, several other constraints impose upon the design of automotive HVAC systems. Volume, manufacturability, and noise are a few of the considerations which need to be addressed. In many cases, size constraints play a dominant role in a design. Awkward mounting geometries and complex internal components often result in a system configuration that is not conducive to high aerodynamic efficiencies. The resulting poor flow conditions produce acoustic sources as flow instabilities generate local fluctuating pressure zones. Therefore, a firm understanding of the internal flow fields is significant to the development of quiet and efficient HVAC systems.

In order to move the required volume of air, a turbomachine must first convert mechanical energy into fluid energy. The device used in the current system and the focus of this thesis, was a forward-curved (FC), squirrel cage, centrifugal device. A centrifugal blower unit is comprised of two matched components: the impeller and the volute, or scroll casing. The volute encloses the impeller and has a circumferentially expanding profile which diffuses and directs the flow toward the outlet. A properly designed casing will efficiently convert high absolute velocity at

the impeller periphery to static pressure, and allow easy connection to a system of ducting [1]. In the ideal case, air is drawn into the impeller axially, and is discharged through radially shallow blades in the direction of rotation with both radial and tangential velocity components. The scroll casing and impeller positioning is presented in figure 1.1 (reproduced from Osborne, [1]).

Typically, blowers of this type can deliver a higher pressure rise and a higher flow rate than other centrifugal machines and axial-flow fans. This is a result of radial energy increase through the blade row, and the vector addition of the relative and rotational velocity components [1]. In contrast, backward-curved impellers direct the relative flow away from the direction of rotation, and axial flow fans have no radial head increase. The velocity triangles created at the periphery of three centrifugal impeller designs are presented in figure 1.2 (reproduced from Osborne, [1]). As shown, a high tangential velocity is attained at the blade exit of an FC design due to the vector addition of the relative and rotational velocities. However, this gain is not without cost. Typical FC impellers maintain efficiencies of less than 75%, while comparable BC impellers yield efficiencies on the order of 90% [1]. This difference may be attributed to poor blade aerodynamics--i.e. high incidence angles and consequent blade stall.

A complete understanding of the internal flow physics through the ductwork and the turbomachine is essential to the design of quiet and aerodynamically efficient automotive HVAC systems.

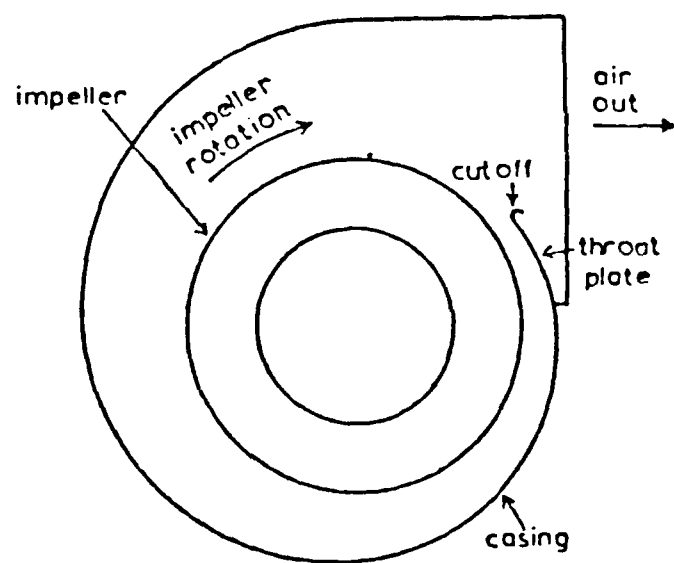


Figure 1.1 Volute Casing and Impeller
(Reproduced from Osborne, [1])

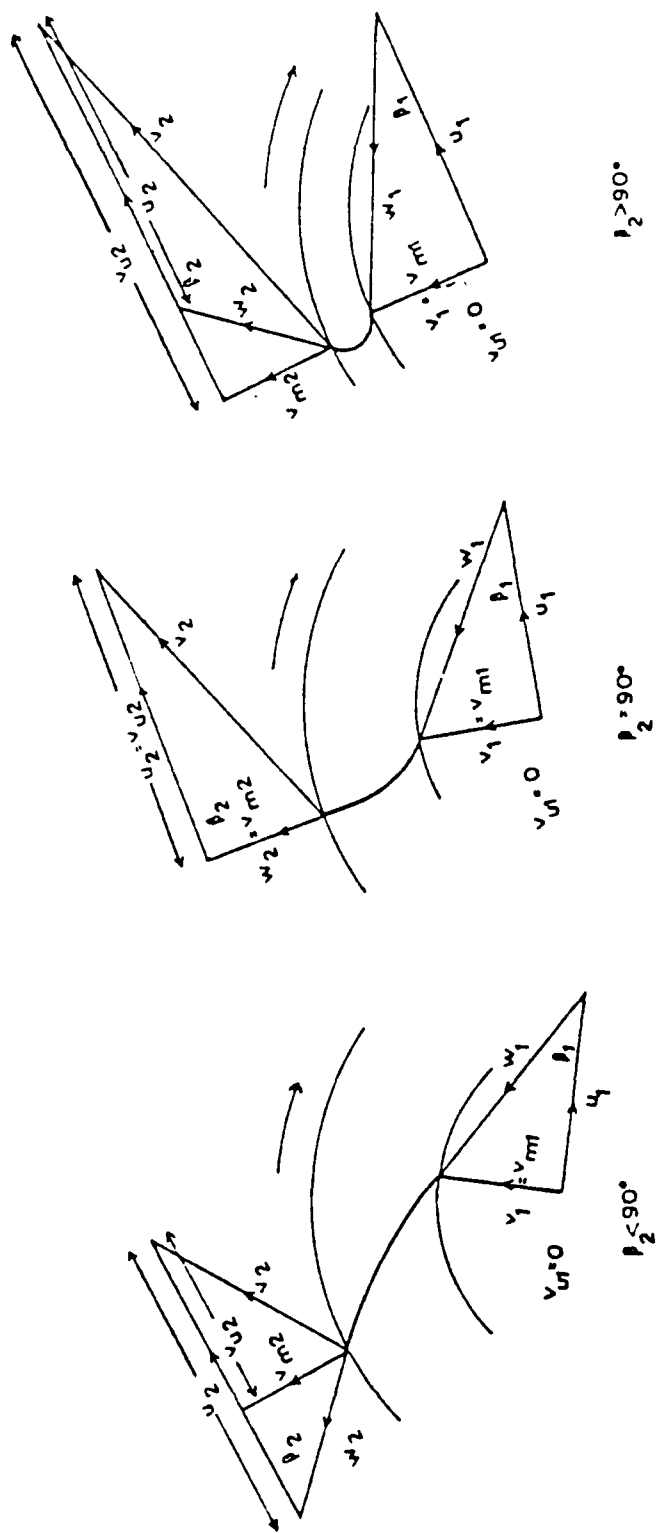


Figure 1.2 Centrifugal Impeller Velocity Triangles
(Reproduced from Osborne, [1])

The energy lost in an inefficient flow may be converted in part to noise energy, and hence the interaction between poor flow and acoustic noise generation is originated. It is the intent of this study to present information which will help guide the future design of HVAC systems and FC centrifugal blowers.

1.2 Centrifugal Fan Noise Generation

Previous work regarding centrifugal blower noise generation may be categorized into three distinct areas: 1) theoretical explanations of the noise mechanisms inherent to whirling blade rows, 2) the influence of blower/volute geometries and, 3) noise reduction techniques with regard to blower performance. Although being comprehensive in nature, these studies indicate that little work has been directed to correlating the fluid dynamics of centrifugal devices to the resultant noise generation. There is also a marginal difference in the investigations dealing with backward and radial curved blowers as compared with those dealing with forward curved blowers (with FC blowers having the least). The following review is presented with the intention of clarifying noise producing flow mechanisms in centrifugal devices, defining optimum fan\volute geometries with regard to noise generation, and presenting current noise reduction techniques. Absent from the following is any detailed acoustical analyses or the methods of acoustical similarity rules as presented in the literature [2].

1.2.1 Noise Mechanisms for Centrifugal Devices

Several noise mechanisms have been identified in centrifugal devices. As for any air moving system, mechanical energy must be converted to fluid energy through some device--in this case an FC centrifugal blower. To accomplish this, the blading must move through a fluid and cause it to interact with the volute. As the blades rotate, they experience periodic lift and pressure fluctuations due to undesirable flow structures and changes in the casing geometry. It is these periodic fluctuations which may be the roots of acoustic noise for the device. For example, the most notable source of noise in centrifugal blowers is unsteady forces acting on the blades [1]. At the point where the volute is closest to the blower, or the cutoff, high amplitude pressure fluctuations act on both the blading and fluid to cause unsteady forces and turbulence, which in turn results in a strong blade passing tone [1,3]. Further, when the impeller operates with a steady but non-uniform inlet flow, each blade experiences unsteady fluid forces due to the circumferential variance of both the magnitude and incidence of the oncoming flow. Accentuating these unsteady forces is the presence of rotating stall cells and leading edge vortices. A rotating stall occurs when a local disturbance stalls the flow in one or more of the blade passages, causing a change in the following blade's incidence angle and stalling this passage. In this manner, the stall cell propagates about the interior of the impeller and

creates low frequency pressure perturbations, noise, and structural vibrations. Rotating stall cells in similar turbomachines have been reported to precess about the interior at half the impeller rotational speed [4].

Another leading cause of noise in an air moving system is the presence of high shear rate turbulence in the flow field and the blade boundary layer. Directly associated with boundary layer turbulence is the occurrence of vortex shedding, which creates noise as tight eddies of air leave the impeller and thus create a fluctuating pressure field at the blade trailing edge. In addition, separated zones created by large expansion angles, 90° bends, and obstacles jutting into the flow generate vorticity, high shear turbulence, and therefore noise to a system [5].

Much of the previous work on centrifugal devices has been aimed at developing noise reduction methods after the blower or system has been designed to meet specific performance goals. In this sense, elements would be added to a system to reduce the noise resulting from a poor acoustic system or blade design. These add on devices may indeed work, but implementation increases manufacturing costs. Therefore, they become unfeasible for mass production applications. Acoustic investigations propose geometric configurations and blade skewing techniques which may be considerably easier to introduce to mass production, but their applications have been limited. It is the intent of the following section to illuminate some noise reduction techniques proposed by several investigators, and point

out both advantages and disadvantages.

1.2.2 Passive and Active Sound Cancellation

The most predominant tone found in a centrifugal machine has been determined to be the Blade Passing Frequency (BPF) generated by the jet-wake/scroll-cutoff interaction. To reduce this tone, Neise and Koopmann [6] have developed several add-on devices. One of their earlier efforts was to place a quarter wavelength resonator at the cutoff. By tuning the resonator to a quarter of the BPF wavelength, destructive interference sound waves were created and effectively deadened this tone. In this study, they found a 10dB reduction in the BPF as well as an overall lowering of the broadband sound pressure level. It was also shown that with a resonator present the pressure fluctuations generated by the blade/cut-off interaction was substantially reduced. In other words, the resonator allowed an outlet for the high pressure generated by the compression zone at the cutoff; therefore, the magnitude of the fluctuations in the pressure field were diminished and consequently the strength of the noise mechanism was diminished.

Neise and Koopmann [7] further expanded the resonator concept by replacing the volute cutoff with an active source cancellation device. This system entailed prompting loudspeakers to generate destructive sound waves, which cancel the blade passing tone as well as an arbitrary harmonic. In some cases, their experiments showed

reductions of as much as 20dB for both the fundamental tone and the first harmonic, with no apparent effect on the broadband spectrum. They hypothesized that the active source directly altered the noise mechanism by stabilizing unsteady fluid forces. Thus the BPF was reduced due to the decrease in unsteady fluid-solid boundary interactions.

While both the active source and resonator concepts reduced the sound pressure level of the BPF, both have several shortcomings. The first of these is the impracticality of assembling such devices on a mass production scale. Because of the diverse use of centrifugal blowers, installing a resonator tuned only to one condition will add considerable cost, while producing only small returns. Likewise, the electronics needed in an active source cancellation device render it unfeasible.

Another problem for resonators is their inapplicability to broadband noise. A properly tuned resonator will reduce the BPF considerably, but the broadband noise emanating from other areas within the volute will not be as greatly affected. Therefore, in a system which broadband noise is predominant, a resonator would have relatively little influence on the overall sound level. Active systems could be made to work, but the complexity and expense of such a system may not justify the reduction of noise.

1.2.3 The Influence of Geometry on Noise Generation

It was shown by Embleton [3] that by skewing the blades opposite to the direction of rotation, electrical power, volume flow rate (at low wheel speeds), and sound pressure level were reduced. However, at rotation rates over 600 rpm, a given volume of air was delivered with less power by the impeller with skewed blading. By comparing the sound pressure level of a skewed blade fan to an unskewed blade fan, it was found that the sound pressure level was reduced 9 to 12 dB at the BPF and at half the BPF. This conclusion was reached by holding the rotor speed constant. A more revealing comparison might have been to compare the sound power level between the two impellers while maintaining volume flow rate. Since the skewed design needs to spin faster to deliver a required flow, one might assume that the broadband noise generation may be higher than the original design.

Similar to Embleton's work, Lyons and Platter [8] also worked to reduce the BPF. Their studies indicated that skewing the cutoff across two blade channels resulted in a 10 dB reduction in the BPF with no appreciable loss in aerodynamic efficiency. Their efforts also indicated that this configuration was most effective when the fan was operating at its maximum efficiency point.

1.3 Research Regarding the Fluid Dynamics of FC Blowers

The following sections document previous research into the flow field created by FC centrifugal impellers. The first section is intended to characterize the FC flow field and set a precedent for the results of the present study. The second section details closely related topics and various design permutations which have been studied.

1.3.1 Characterization of the FC Blower Flow Field

Relatively little work has dealt directly with quantifying the flow field of FC designs. In general, much of the work dealing with centrifugal devices has been concentrated on high performance compressors and backward curved (BC) designs.

A few authors, [9,10,11] have presented results which have dealt specifically with squirrel cage blower designs. The data shows that the flow field may be characterized as having several inefficient flow processes. The first trait typifying the flow field is the presence of an "inactive" zone over the impeller blades near the inlet (shown in figure 1.3). In this region, little or no through flow has been documented, and it has been suspected that the blade passages contain completely separated flow. This zone is believed to be the result of high axial momentum dominating the inlet flow and a static pressure distribution over the hub which is

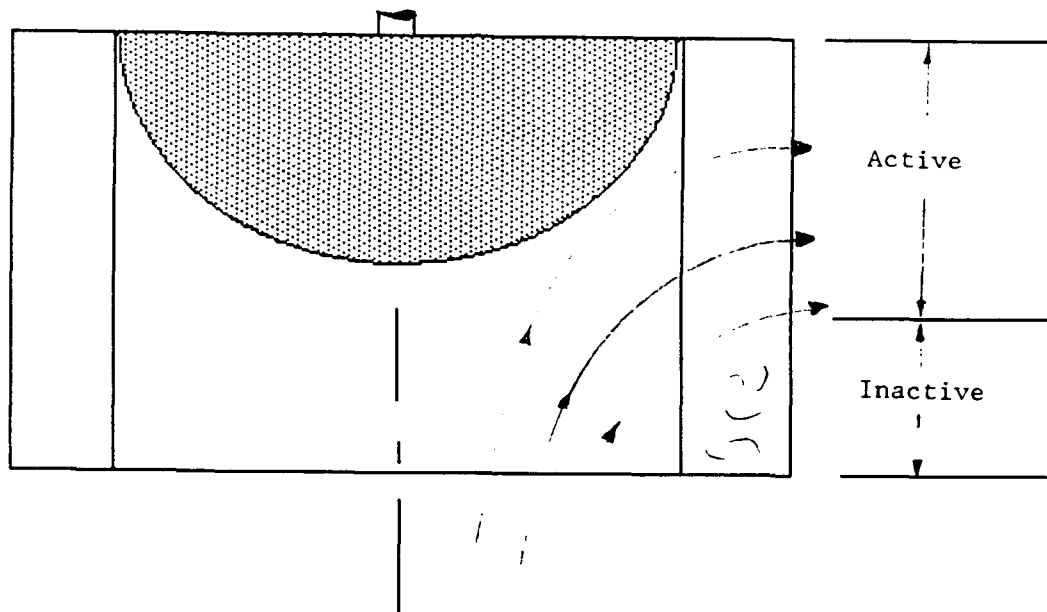


Figure 1.3 Sketch of "Inactive" Flow Zone

insufficient to turn the fluid to the radial direction. Studies have indicated that, due to the "inactive" zone, the volute flow varies significantly with axial location. The near-inlet volute flow has been shown to be largely tangential, in contrast to the more radial flow at the midspan and backplate.

Through use of a five-hole pressure probe, Kind and Tobin [12] were able to show the presence of re-entrant flow near the volute cutoff. Their data indicated that this reverse flow occurred across the span as the blade approached the cutoff and for approximately 90° downstream of the cutoff. This phenomenon was most prevalent at low flow rates.

The "inactive" zone and axial dependence of the volute flow suggest that the blades are non-uniformly loaded across the span. To understand the blade passage flow in greater detail, Raj and Swim [9] visualized the blade boundary layer flow with tufts. The tufts indicated that the suction side of any blade was experiencing boundary layer separation.

Raj and Swim, and Yeager [10] quantified the axial variation of the blade passage discharge relative velocity profiles with single hot wire probes. It was found that the near-inlet blade discharge velocity profiles were nearly linear, in agreement with the observed "inactive" zone, and therefore indicated very little radial kinetic energy being introduced to the fluid by the impeller. Past midspan, the profiles took on the "jet-wake" flow structure, typical of centrifugal impellers. In addition, Yeager's results

showed that kinetic energy transfer is a function of circumferential location as well. The axial and circumferential variance of blade performance implies that the blades are experiencing cyclic blade force fluctuations as they rotate within the volute. Such fluctuations may be one cause of noise generation within the impeller unit.

Cau [13], et al, performed crossed hot-wire velocity measurements on an industrial FC impeller. The test impeller was not of the squirrel cage variety; however, the same flow mechanisms are present as the flow is drawn axially and discharged with radial and tangential velocity components. Results showed that the separation zone near the inlet of the impeller indirectly distorted the primary volute flow. The "inactive" zone caused low through flow which consequently generated secondary flows within the volute. In particular, secondary flow effects influenced return flow in the hub region and variations in vortex structure and wake position.

Some questions arise in regard to the results of the preceding review. Raj and Swim reported that the blades of an FC impeller are always stalled over the suction side--independent of location. This conclusion was reached by observing the behavior of tufts attached to the blades' surfaces. To see flow separation occurring, the blower must be observed in the blade-fixed frame, and be observed at every circumferential and axial location. Even with a clear plexiglas housing, the extreme difficulty of observing every point on a given blade leads one to speculate whether this conclusion is

in fact correct. In addition, standard tufts have non-negligible mass and would be subjected to centrifugal forces created by high blower rotation rates. Therefore, they may falsely indicate flow separation. Fluorescent mini-tufts [14] used with an ultra-violet light strobing device might yield more plausible results, yet optical access would remain as an issue. Further, the use of tufts does not show the extent of separation within the blade passage-- only the separation occurring within the boundary layer. This is a key element in understanding the blade passage flow.

While providing quantitative, three-dimensional data about the impeller flow field, Kind and Tobin did not take into account the effect the five-hole pressure probe has on the flow field. As described, the flow is quite complex, and the five-hole probe may add more instabilities to an already unstable flow. Such instabilities might induce rotating stall cells both in the volute and hub flow. The steady state nature of the data acquired with the probe may also fall short in the description of flow transients and turbulence.

1.3.2 Variations on Centrifugal Blower Design

In addition to internal flow field studies, several authors propose work regarding blower performance as a function of inlet conditions. In many practical applications, uniform inlet flow is unattainable due to size or positioning constraints. Wright, et al [15] found that non-symmetric inlet velocity profiles degraded overall fan performance by several percentage points. Their work suggested that severe inlet flow distortions, i.e. 30-50% in velocity variation, can cause up to 12% reductions in efficiency and head rise, as compared with uniform inflow conditions. Wright [16] also studied the effect of inlet clearance gap on impeller output. Although this work was performed with a BC blower, it may be expected to apply to centrifugal devices in general. It was shown that a decrease in inlet clearance gap resulted in increased blower performance. However, this increase was marginal at best, and increased manufacturing costs might not justify such a design. Senoo and Ishida [17] presented results which agree with the work of Wright in that an optimum inlet clearance gap would be economically unfeasible.

Efforts have also been made to analytically solve the flow field of BC centrifugal blower units [5,18,19]. No apparent research has been aimed at solving the internal flow field of an FC impeller. The documented work has been simplified to such a point that the validity of the results may be questionable. Of the

reviewed literature, only inviscid and potential approximations have been used to solve the flow. As described in section 1.3.3, the FC impeller flow field contains extensive separation zones and is highly chaotic. Wright [18] added viscous losses to an inviscid code, which provided results closer to experimental findings. However, inviscid solutions do not agree very well with experimental data. Therefore, current "ideal" solutions might be best suited for comparative purposes rather than prediction of performance.

1.4 Thesis Organization and Overview

The following thesis documents the experiments performed in order to identify the flow physics within a typical automotive HVAC system. To accomplish this, several experiments were performed, each aimed at different aspects of the system.

The first experiment was aimed at determining the internal flow paths of the HVAC system. This was accomplished by mounting a clear automotive HVAC system in a water tank, and utilizing flow modelling procedures and a dye flow visualization method to trace the flow. This method was chosen over standard smoke wire visualization because of the complex ducting geometry and the highly turbulent nature of the flow.

The second experiment was performed to determine the overall performance of the FC centrifugal blower unit used in the HVAC system. This experiment was aimed at identifying the effect that

the two inlets modes of operation have on blower performance.

A three-times-size model of the HVAC blower was mounted in a water tank in order to perform qualitative flow visualization studies and quantitative, two-dimensional velocity measurements. Both techniques involved seeding the water flow with nearly neutrally buoyant particles and illuminating a region of interest with a laser light sheet. Data acquisition and reduction was performed via image processing routines. Qualitative studies were videotaped.

The final experiment involved a novel technique to visualize the flow within the blower blade passages. An image derotation device and the particle visualization method were used together in order to identify the relative flow through the three-times-size model.

This thesis is organized as follows. Chapter 2 gives a brief description of the equipment used and the modelling procedures followed during the course of the study. The acquisition and reduction techniques used to gather and process data are presented in Chapter 3. The results of the experiments are presented in Chapter 4, and conclusions are found in Chapter 5.

Chapter 2

EXPERIMENTAL METHODOLOGY

2.1 Equipment

The following sections document the equipment used to study the automotive HVAC flow field, and the flow modelling techniques which were followed.

2.1.1 Experimental Water Tank

Flow visualization studies and quantitative measurements were performed on experimental models which were mounted in a clear plexiglas water tank. This tank measured 1.83 m x .914 m x 2 m and held approximately 1900 liters of water. The tank walls and bottom were 1.91 cm thick and were supported by an iron frame and steel banding. Optical distortion of the plexiglas was not a concern for these experiments.

The tank water had a dissolved gas content of 4.5-6.0 ppm on a molar basis, and was filtered by an internal system capable of circulating 946 liters per hour. Two liters of bleach were added to each full tank to prevent bacteria buildup.

2.1.2 Clear HVAC System

A clear automotive HVAC system, shown in figure 2.1, was supplied by a manufacturer to conduct underwater dye flow visualization studies. This unit contained the components of a typical automotive HVAC system: a variable inlet to allow fresh air and recirculated air intake; a centrifugal blower; a cooling, or evaporator core; a heating core; and multi-outlet exit ducts. Inner metallic components were painted white to slow oxidation and provide a high contrast background for dye visualization. The blower rotation rate was controlled via an axle which passed through the test tank walls and connected to a variable speed DC motor.

2.1.3 Prototype and Three-Times-Size Blower

The turbomachine used in the experimental HVAC system was a forward-curved (FC) squirrel cage centrifugal blower. This blower is pictured in figure 2.2. Relevant dimensions are presented in table 2.1. The blade geometry is shown in figure 2.3.

A three-times-size, optically transparent plexiglas model of the prototype, volute casing, and inlet was manufactured to scaled dimensions of table 2.1. The blade orientation was identical to that shown in figure 2.3. Figures 2.4 and 2.5 show the model. The

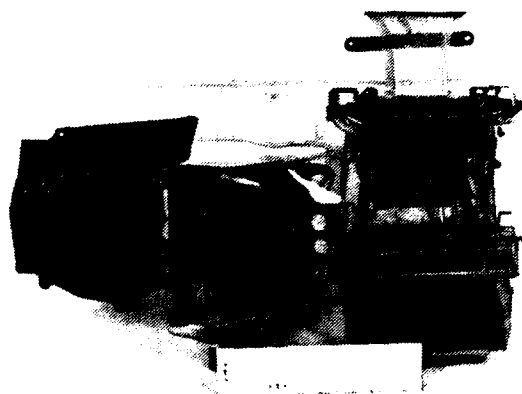
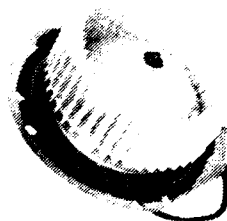


Figure 2.1 Clear Experimental HVAC System



1

2

Figure 2.2 Prototype Blower

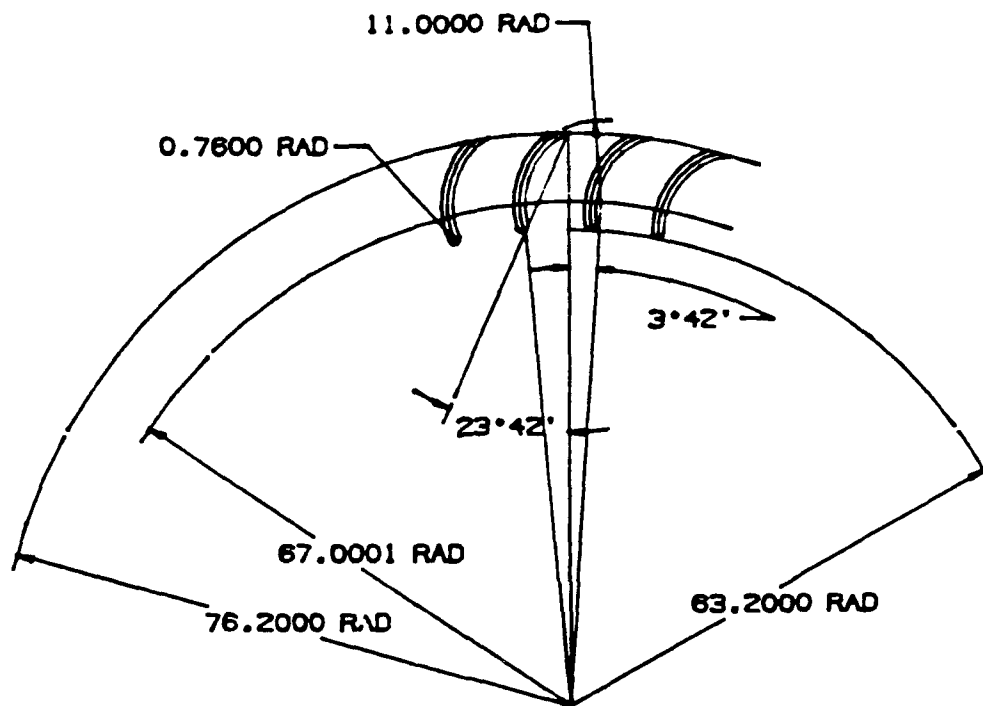


Figure 2.3 Prototype Blower Blade Detail

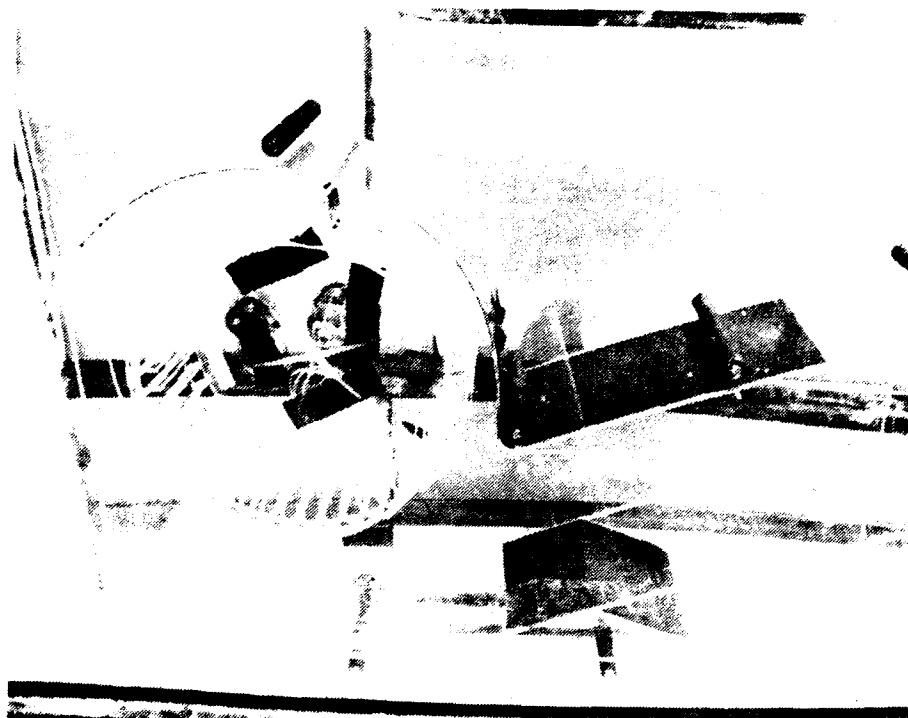


Figure 2.4 Front View of Three-Times-Size Blower

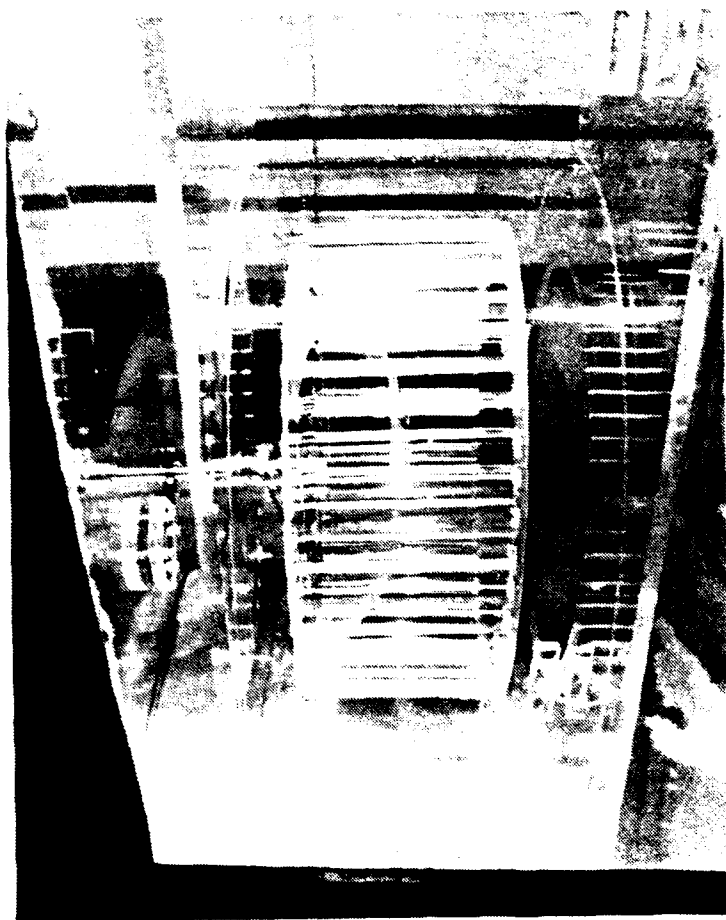


Figure 2.5 Side View of Three-Times-Size Blower

Table 2.1 Fan Dimensions and Operating Details

Rotor Eye Diameter	38.1 cm
Rotor Outlet Diameter	45.7 cm
Rotor Width	18.1 cm
No. of Blades	44
Blade Inlet Angle	15°
Blade Outlet Angle	60°
Volute Casing Width	27.3 cm
Operating Speed	22 rpm
Cutoff Distance	14% of Radius

inlet modes were modelled after those of the HVAC system. Except for the cutoff region and the hub, the assembly was transparent, thus allowing visual access throughout the system.

The model was mounted in the test tank in order to conduct particle streak flow visualization studies, and to quantify the volute flow of one of the operating modes. The rotation rate was controlled by an axle which passed through a tank wall and connected to a variable speed DC motor.

2.1.4 Illumination Method

The light source used in the particle streak flow visualization method was an Argon-Ion laser which delivered roughly 1W of power to the plane of interest. In order to generate the

required optical characteristics, the laser beam was directed through a mechanical beam chopper and a series of lenses. The beam chopper operated at a frequency of 75 chops per second to create series of laser pulses $1/75$ s in duration. Once chopped, the beam was expanded and collimated by a 20mm focal length lens and a 10mm focal length lens, respectively. The beam thickness could be varied by changing the relative positions of these two lenses. The final step was to generate a laser light sheet by passing the expanded beam through a diverging, cylindrical lens. The laser sheet then passed through the clear plexiglas tank walls and oriented perpendicular to the axis of rotation. Figure 2.6 shows the optical schematic.

2.1.5 Image Processing Workstation

A PC based image processing workstation was developed to provide a means of quantifying the volute flow. A PCVISION 640 x 512 x 8 bit (greyscale) resolution frame grabber board was installed in an I/O port of a 386 personal computer. The frame grabber was accessed and controlled by menu-driven, image processing software (OPTIMAS). The OPTIMAS software had many built in features which expedited data acquisition and analysis.

A Sanyo VDC 3860 high resolution, monochrome, CCD image camera with 392,000 picture elements was used to acquire the images needed for image processing and data reduction. This camera required only

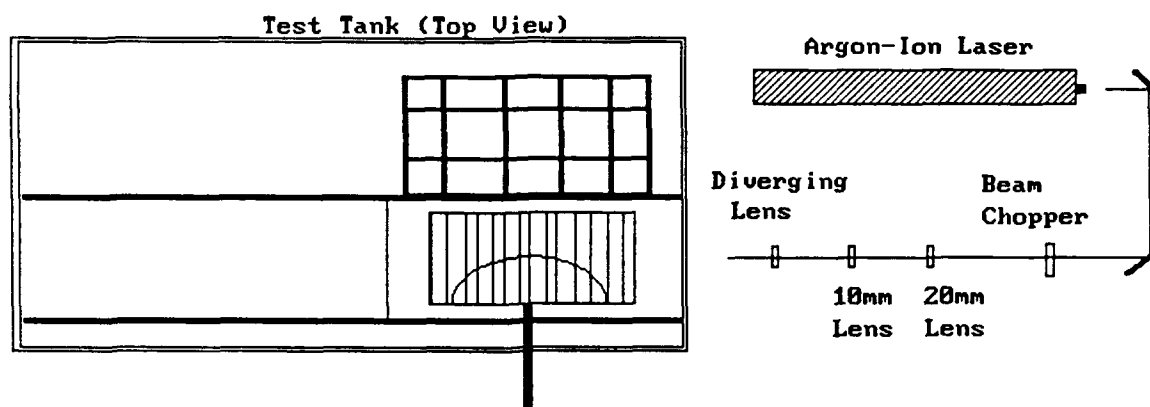


Figure 2.6 Optical Configuration

3 lux illumination with a F1.4 lens for imaging. The electronic shutter time of the CCD was 1/30 s. Two output lines were taken off the camera. One line was directly input to a "live" image monitor to allow real time observation of the field of view. The second line was input to the frame grabber board to allow processing, and the resultant image was displayed on the "processed" monitor. Images were printed by a Hewlett-Packard Laser Jet printer. Figure 2.7 shows the image processing setup.

2.1.6 Optical-Mechanical Image Derotator

An optical-mechanical image derotator was utilized in visualizing the relative flow over the hub region and within the impeller blade passages. The orientation of the experimental model and image derotator device is shown in figure 2.8. This device was oriented along the blower axis of rotation and the optical path was normal to the laser light sheet.

The function of an image derotator is to "provide an effective reflection in a plane containing the optical axis of the system" [20]. The reflecting plane is within the derotator and thus rotates at the speed of the device. Therefore, a stationary image viewed through the device would appear to rotate at twice the derotator angular rate. Likewise, if an object rotates in the field of view at a fixed angular rate Ω , the derotator must rotate at $\Omega/2$ to make the object appear stationary when viewed through the device. It is

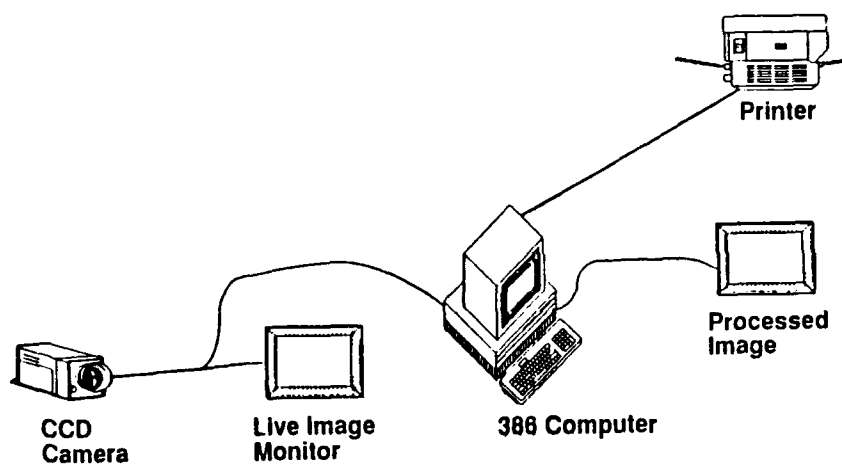


Figure 2.7 Image Processing Setup

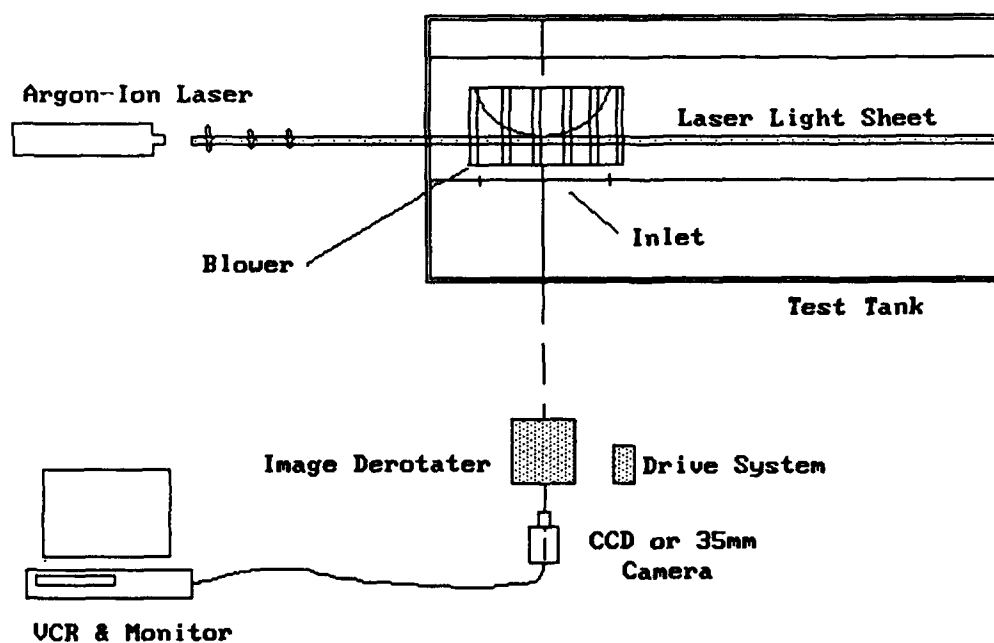


Figure 2.8 Image Derotator Orientation

this "half-speed" operation which results in a reversed, or mirror image of the field of view. In the present study, the image reversal is inconsequential, but could easily be ameliorated by adding one more reflective surface to the optical path. A Compumotor and controller was used to drive the derotator at the necessary angular rate.

2.2 Flow Modelling Methods

The validity of the flow visualization studies which were performed in this study is strongly dependent upon maintaining similar flow between the original system and the experimental systems. Thus flow modelling criteria were followed to ensure dynamically similar flows.

2.2.1 Clear HVAC System

A modelling method was utilized to ensure that the water flow through the clear HVAC system was similar to the true air flow. In the present case, complete geometric similarity was maintained because the clear system is a replica of the standard HVAC system (described in detail, section 2.1). Dynamic similarity was maintained as follows. The chord Reynolds number of the blower

operating in air was determined from the equation:

$$Re_{air} = CV_{tip}/\nu \quad (2.1)$$

To maintain similar flow:

$$Re_{air} = Re_{water} \quad (2.2)$$

To satisfy equation 2.1 and operate the blower in water rather than air, the following correlation between air flow and water flow must be followed:

$$(V_{tip})_{water} = (V_{tip})_{air}\nu_{water}/\nu_{air} \quad (2.3)$$

Thus to maintain similar flow, a blower operating at a speed of 3000 rpm in air would be required to operate at 200 rpm in water. Application of equation 2.1 with any velocity in the system yields the same scaling of equation 2.3. For the modelling method, the flow coefficient is given as:

$$\phi = V_{rad}/V_{tip} \quad (2.4)$$

As velocity scales by a factor of fifteen, the value of the flow coefficient remains constant between models. The head coefficient was maintained constant by a similar argument. The head coefficient

is given by:

$$\psi = 2gH/V_{tip}^2 \quad (2.5)$$

Because head rise, H , is proportional to the square of velocity, determination of equation 2.5 for operating in the blower in either air and water will give identical results.

2.2.2 Three-Times-Size Blower

The three times scale model was geometrically similar to the prototype design. In particular, blade orientation, number of blades, hub, and inlet were similar. Therefore, the primary concern was in maintaining a dynamically similar flow between the model in water and the prototype in air.

To model the flow of the prototype blower, pump scaling laws were applied to determine the similarity coefficients of the design [1,21,22,23]. The chord Reynolds number of the prototype blower was determined by equation 2.1. The three-times-size model must operate in a manner to match this value to maintain a similar flow. Thus

$$(Re)_p = (Re)_{3x} \quad (2.6)$$

The change of operating medium from air to water requires a reduction in rotation rate by a factor of fifteen, as shown by equation 2.3. Because of the size increase, the rotation rate must be reduced again by the square of the size increase. The correlation for similar flow is given by:

$$\Omega_{\text{water}} = \Omega_{\text{air}} D_p^2 \nu_{\text{water}} / D_{3x}^2 \nu_{\text{air}} \quad (2.7)$$

As shown by equation 2.7, a significant reduction in operating speed can be realized by increasing model size and changing the working fluid.

The second criterion in setting similar flow conditions was to determine the head rise needed by the original impeller in order to supply the required flow rate. Centrifugal fans are widely used and are subjected to many different loading conditions, inlet conditions, and operating speeds. To cover the entire spectrum of operation is therefore beyond the scope of this study. A worst-case situation which involved poor inlet flow and high downstream losses was investigated. The downstream losses were estimated by modelling the HVAC system as a pipe-flow with many elbows, expansions and contractions. This information was then used to determine the pressure loss coefficient of the system. In equation form, the pressure loss coefficient is:

$$\psi = 2gH/V_{\text{tip}}^2 \quad (2.8)$$

Having defined this parameter for the original model, the corresponding values of loss coefficient for the three-times-scale model may be determined. A screen which generated the required losses was then placed at the blower exit to simulate the losses incurred in the original system [24].

Similar to the modelling of the HVAC flow, and because of the system loss modelling, the flow coefficient was held constant as the ratio between a typical velocity and the impeller rotation rate was unchanged.

Modelling methods provided geometric similarity as well as dynamic flow similarity; therefore the flow fields of the two centrifugal fans differed only by a scaling constant. In summary, flow similarity is maintained between a prototype blower operating in air and a three-times-size blower model operating in water when the model is subjected to similar head losses and rotates 135 times slower than the prototype.

Chapter 3

DATA ACQUISITION AND REDUCTION TECHNIQUES

3.1 Blower Performance

The prototype centrifugal blower and volute was mounted to discharge into a large plenum chamber with a circular orifice exit in order to establish head rise against flow rate characteristics. The total pressure at blower discharge, and static pressure of the plenum were acquired through use of kiel and static pressure probes, respectively [25]. Pressure data were obtained from a water micromanometer accurate to .003 cm. Impeller rotation rate was obtained from a calibrated stroboscopic light source. Power was supplied to the impeller motor by a DC supply capable of providing 25 amps at 12 volts. Power consumption data were obtained by a calibrated voltmeter and DC ammeter.

The voltage supplied to the impeller motor was maintained at $12 \pm .5$ volts for this set of experiments. However, the exit area (circular orifice diameter) of the plenum was varied to determine the performance of the impeller when operated at different loading conditions. At each condition, blower discharge pressure, plenum pressure, impeller rpm, and electrical power consumption data were obtained. Because the plenum cross-sectional area was significantly

larger than the blower discharge area (1 m^3 as compared with 0.008 m^2), velocities within plenum were considered to be negligible. Once the plenum static pressure was known, a simple calculation determined the flow rate.

The performance of the blower was determined for both of the inlet flow conditions experienced by the automotive HVAC system. The two inlet modes of operation are shown in figure 3.1. As shown, the "fresh" inlet flow is non-axisymmetric and is drawn from above the unit, while the "recirc" inlet flow is drawn from the front of the unit.

3.2 Dye Visualization of the Internal HVAC Flow

An underwater dye injection flow visualization method was utilized to determine the internal flow paths of the HVAC system. For this purpose, the clear HVAC system, shown in figure 2.1, was mounted in the test tank. Following the modelling methods of section 2.2.1, the impeller was rotated approximately 15 times slower in maintaining a dynamically similar flow. Red dye #7 coloring was injected to the flow field via 50 ga hypodermic tubing and a gravity feed system. To ensure that the dye did not significantly disrupt the internal flow, special care was taken to introduce the dye with negligible relative velocity.

The flow visualization was performed with the HVAC system operating under many configurations. In addition, the blower speed

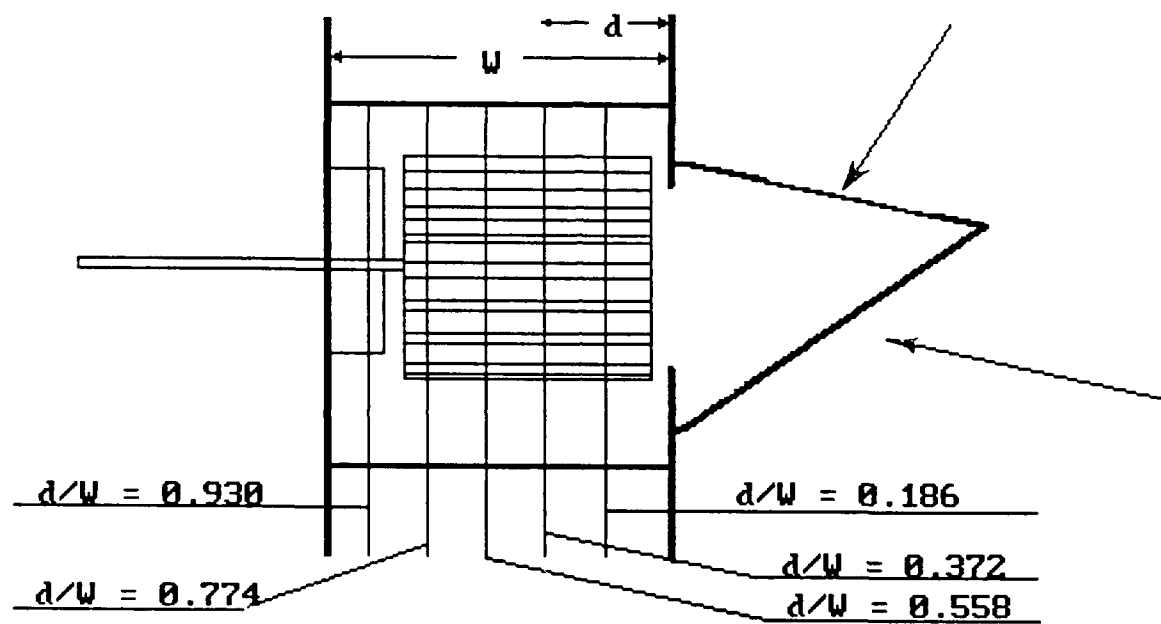


Figure 3.1 Data Acquisition Planes for Particle Tracing Velocimetry Experiment

was varied at every operating condition in order to determine the effect on the downstream flow field. The majority of this qualitative data was recorded on videotape as photographs and sketches fall short in portraying the flow field. Nonetheless, several sketches, which correspond to the highest blower setting, are included in a later section to show the highlights of this experiment.

3.3 Particle Tracing Velocimetry (PTV)

The flow field of the blower volute with the "fresh" impeller inlet condition was quantified by a particle tracing method. This operating condition was chosen because it represents the worst configuration the impeller is faced with--high downstream losses and non-uniform, non-axisymmetric inlet flow. The following sections document the procedure followed in acquiring and analyzing the data.

3.3.1 Image Processing/Data Acquisition

Particle tracing velocimetry is a technique used to obtain fluid velocity data by optically tracing seed particles in the flow. In the past, the method was used primarily as a qualitative tool to better understand complex flow fields. Presently, advances in personal computer (PC) operating speeds and software have reduced the amount of manual labor required for quantitative analysis of a

flow [26,27,28]. Thus, the application of the PTV technique to the quantification of various flow fields has become more widespread.

The success of the PTV method is strongly dependent upon the ability of the seed particles to effectively follow the motion of the local fluid particles. In general, non-neutrally buoyant particles will introduce error to the technique as inertial and gravitational forces increase rapidly with particle size. Small, neutrally buoyant particles are therefore the ideal choice for flow seeds, as they react similar to a fluid particle. The error involved with non-neutrally buoyant particles is documented in Appendix A. Merzkirch [29] documented the response time of a seed particle to a step change in fluid velocity as

$$\tau_p = D^2/18\nu \quad (3.1)$$

For flows varying slower than τ_p , seed particles can effectively trace the local flow. In the present experiment, the flow field near the impeller periphery varies at a rate equal to the inverse of the BPF. Thus the particle response time must be equivalent to, or less than $1/\text{BPF}$ to ensure that the particles are suitable flow seeds (Refer to Appendix A).

Particles used to seed the flow were 250-500 microns in diameter, and had a specific weight of 1.02. As these particles passed through the laser light sheet (LLS), they scattered light through Mie Theory [29] in a direction normal to the plane. It was

this characteristic which allowed optical tracking of the seed particles.

In order to obtain unambiguous particle traces, it was necessary to ensure that a particle did not move out of the LLS during the camera exposure time. The electronic shutter of the camera was fixed at $1/30$ s and a mechanical beam chopper operated at a frequency of 75 chops/s. Due to the chopping frequency, every image contained particle streak sequences of three light patches if the particle did not move out of the LLS during exposure. Traces which contained a short-long-long or short-long-short pattern, indicated that the middle streak remained in the sheet for the duration of the camera exposure time. The length of this trace was thus proportional to the local flow velocity in the radial and circumferential directions.

The LLS thickness could be varied by changing the relative position of the two converging-diverging lenses (sec. 2.1.4). Due to the axial velocity component of the flow, the laser sheet thickness was maintained at 1.0 cm. It was found through experiment that 95% of the trace patterns included the three pulse sequence when the laser sheet was maintained at this thickness. This results in two important properties of the flow field: the axial velocity component of the flow in the volute was no greater than the plane width (1.0 cm) divided by the exposure time of the camera ($1/30$ s), and the middle particle trace was entirely in the sheet for the duration of the pulse. The latter of these was utilized as the

criterion for a valid data point.

The particles were imaged by a Sanyo CCD camera, and images were captured using a frame grabber board controlled through the I/O ports of the PC. Before storing an image, a binary input filter was applied to the incoming video signal. This "prefilter" reduced the image from one which contained eight bits of grey level information to one which contained two grey levels: black and white. This filtering had two useful effects on the process. First, the scattered light noise level was significantly reduced as only strong signals were replaced with white pixels. Background light reflections and particles not fully illuminated by the laser sheet were replaced with black pixels. This removed extraneous light noise and particle streaks which were not entirely in the laser plane. Second, the reduction of grey levels reduced by a factor of two the amount of memory required to store an image on the PC--thereby significantly increasing the amount of data that could be stored.

Because of the size of the experimental unit, data were acquired from several "cells" about the impeller periphery. A complete description of the velocity flow field in the $R-\theta$ plane was obtained when the velocity field from each cell was added to the data base of the particular axial location. At every cell, approximately thirty images were obtained, each containing up to 300 unreduced particle streaks. As the light sheet was only 1.0 cm thick, it was necessary to obtain images at every cell for five axial locations of the impeller, as shown in figure 3.1 (page 39),

to determine the axial variance of the flow field. By performing measurements on five planes and at all grid locations, the three-dimensional flow field characteristics could be defined by two dimensional representations.

An algorithm which involved analytical and image processing steps was developed to process images efficiently. Figure 3.2 shows the steps involved with acquiring and processing images. The upper flow chart shows the image acquiring procedure. Before images were saved to disk, they were visually checked to ensure that the correct trace patterns constituted the majority of the velocity field data. The lower chart shows the steps the image processing algorithm performed when extracting data from images.

The first step in this routine was to define the data which would be extracted from each image. Particle streak vector length and endpoint location values were specified. The image processor was calibrated at each cell and axial location. The second step was to call the correct calibration for each location before opening the images of the location.

A threshold filter was applied to each image in order to allow the software to identify valid particle streaks. Upper and lower threshold values were determined by a pixel intensity histogram of a typical particle streak. This threshold value was determined prior to the start of the data acquisition program. Pixel intensity values which fell within the threshold range were placed in the "foreground" of the image, while intensities outside the threshold

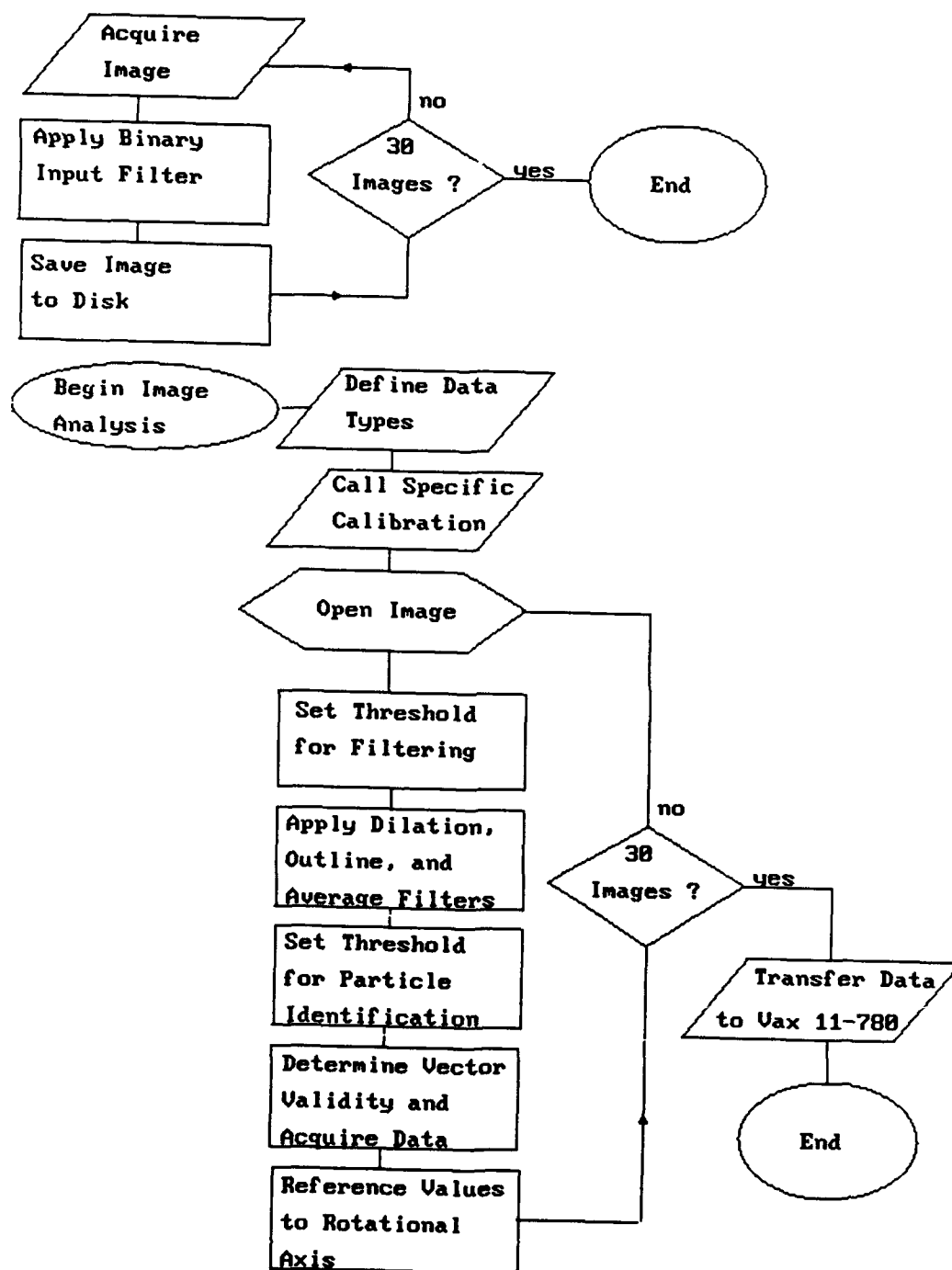


Figure 3.2 Image Processing Algorithm Flow Chart

range were overlooked by the software, or placed in the "background" of the image.

A series of filters were applied to the foreground objects of each image. First, each object was "dilated" to enlarge the streak two pixels along the perimeter. Next, an outline filter was applied. This filter first discerned between foreground and background objects. Foreground pixels in the resulting binary image which are along an intensity gradient remain unchanged, while all other pixels change to background. The net effect of the dilate and outline filters is to replace vector streaks with elongated areas with well defined perimeters. However, the outline filter generates pixel "noise" which may be misinterpreted by the software. To ameliorate this problem, a 3x3 matrix averaging filter was applied. This filter replaces a central pixel with the average value of the neighbor pixels above, below, right, left, and along the four diagonals. Effectively, this filter reduced the outer boundary by one pixel.

Upon completion of the filtering steps, data points were extracted from the image. The software featured automatic area identification which allowed autonomous velocity vector data acquisition. The endpoints and major axis length were extracted for each vector. The major axis length was defined as the longest chord passing through the centroid of the area. The major axis points were referenced to the lower left hand corner of the image.

To ensure that only valid particle streaks were exported to

file, an analytical thresholding criterion was defined. Vector length values which were above or below the set range were discarded. Accepted values were referenced to the axis of rotation to provide proper positioning of the data. Approximately 150,000 velocity vector values were acquired through this process.

3.3.2 Data Reduction

A data reduction analysis algorithm was developed on a Vax 11-780 computer. The routine involved superimposing a polar grid of cell blocks over the raw vector data field. Each block had a radial depth of 5 cm and spanned a 20 degree arc. Vectors were identified to be within a given cell by comparing the tail point with the area the cell covered. Once the data values were segregated into correct cells, the average vector length and x and y velocity components were determined if the cell had more than thirty vector values.

The standard deviation of the x and y components were then computed. Vectors were discarded if their x and y component values were more than two standard deviations from the average value. The reduced data set was processed again to yield the new x and y velocity components. The x and y components were then used to determine the average vector angle for the cell. At this point, the vector magnitude standard deviation was determined.

A transformation from Cartesian to polar coordinates was performed to determine the radial and tangential velocity

components. The absolute and relative velocity magnitudes were likewise computed. A flow chart of the procedure is shown in figure 3.3.

An interpolation routine was then used to determine intermediate values of the volute flow from the averaged data. The routine used the x and y components of the vectors in each data set to calculate a parametric spline fit. Intermediate values were interpolated from the curve and sent to file.

3.4 Visualization of the Blower Relative Flow

Relative flow field data were obtained from axial locations $d/W = 0.186$ and $d/W = 0.372$ with the blower unit operating in both the "fresh" and "recirc" inlet modes. The data is primarily in the form of photographs which contain particle path information. Incidence as a function of circumferential location was extracted from the photographic data. Photographs were taken with a 35mm camera fitted with a 135mm lens and an automatic film advance. Sequences of photographs reflect a constant exposure time as well as a constant time interval between images. The derotator allowed one segment of the impeller to be followed as it rotates in the volute. Thus the same blades are shown in each photo. Due to the shutter time and film advance time, there is some "overlap" between

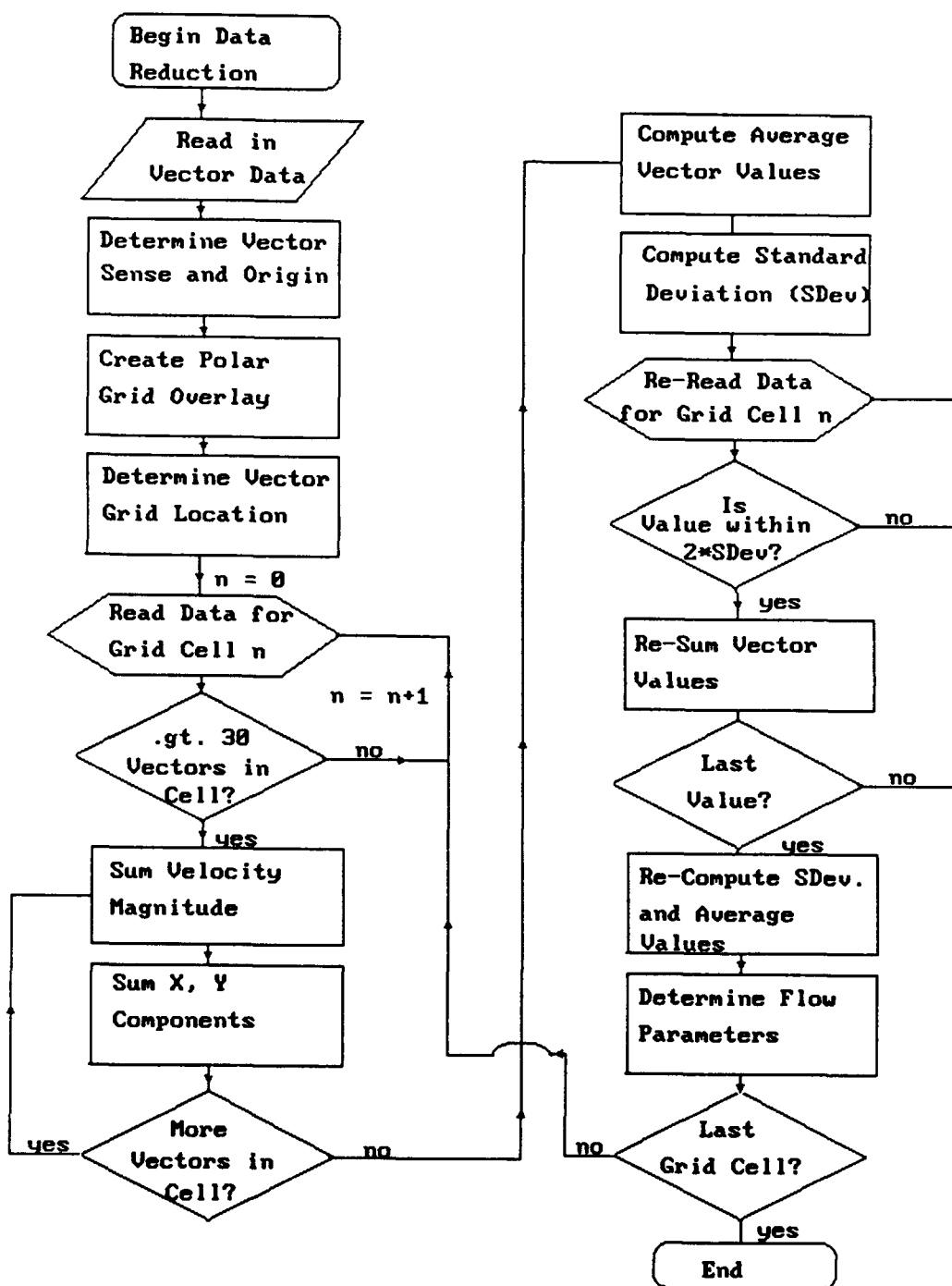


Figure 3.3 Data Reduction Flow Chart

successive photos. In this regard, a portion of figure 5, for example, would contain some information which could be found in figures 4 and 6.

Chapter 4

RESULTS4.1 Blower Performance

Figure 4.1 shows the performance curves and efficiencies of the prototype blower when operating in either inlet mode. The curves are typical of FC centrifugal blowers: high shut off head and a steep slope at high flow rates.

The effect of the inlet configuration on fan performance is shown in figure 4.1. In the "fresh" inlet mode, in which air is drawn from above and through ducting, lower performance occurs at the higher flow coefficients. Assuming a relatively constant rotation rate, the difference in performance may be attributed to several phenomena. One reason may be that the non-uniform inlet flow results in increased head losses within the impeller blade passages. Another reason may be that head losses occurring in the inlet ducting increase with flow rate. Thus the total pressure at the impeller eye is lower for the "fresh" mode than for the "recirc" inlet flow. As shown by Wright [15], distorted inlet flow may cause significant performance reduction. The blower efficiency for either inlet mode does not exceed 50%.

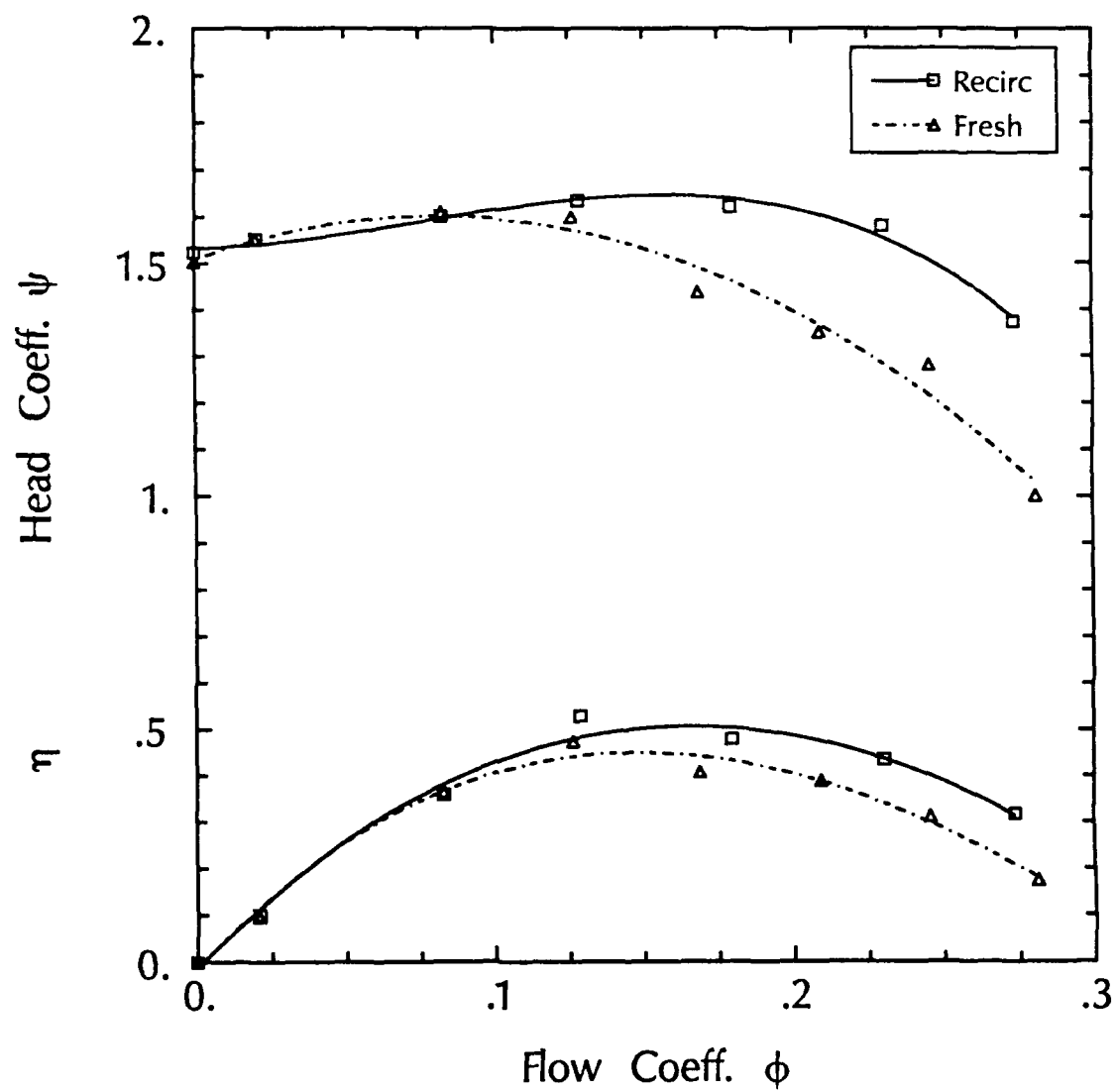


Figure 4.1 Blower Performance Curves

The volute wall static pressure coefficient values for both inlet modes as a function of circumferential location is shown in figure 4.2. This data was obtained through the use of flush mounted static pressure taps. As shown, the "recirc" inlet mode creates higher static pressure per impeller revolution at locations up to $\theta = 270^\circ$. This result agrees with the data shown in figure 4.1, which indicate the impeller produces higher pressure rise when operating in the "recirc" mode. The sharp variance in the data at circumferential location $\theta = 90^\circ$, may indicate that the flow is slowing in this region and therefore the static pressure increases. The general trend of the curves after $\theta = 180^\circ$ indicate that the static pressure in the volute is rising, presumably due to high mass flow near the discharge and energy transfer from the impeller.

4.2 Dye Visualization of the Internal HVAC Flow

The dye injection flow visualization method provided a means to acquire qualitative data about the internal flow paths of the HVAC system. The experimental system contained many geometries which were not believed to be conducive to efficient flow. Some examples include sharp corners, heating and cooling cores, and sudden area expansions. Given the basic geometry, it was expected that the internal flow field would be complex. The dye visualization method confirmed these expectations.

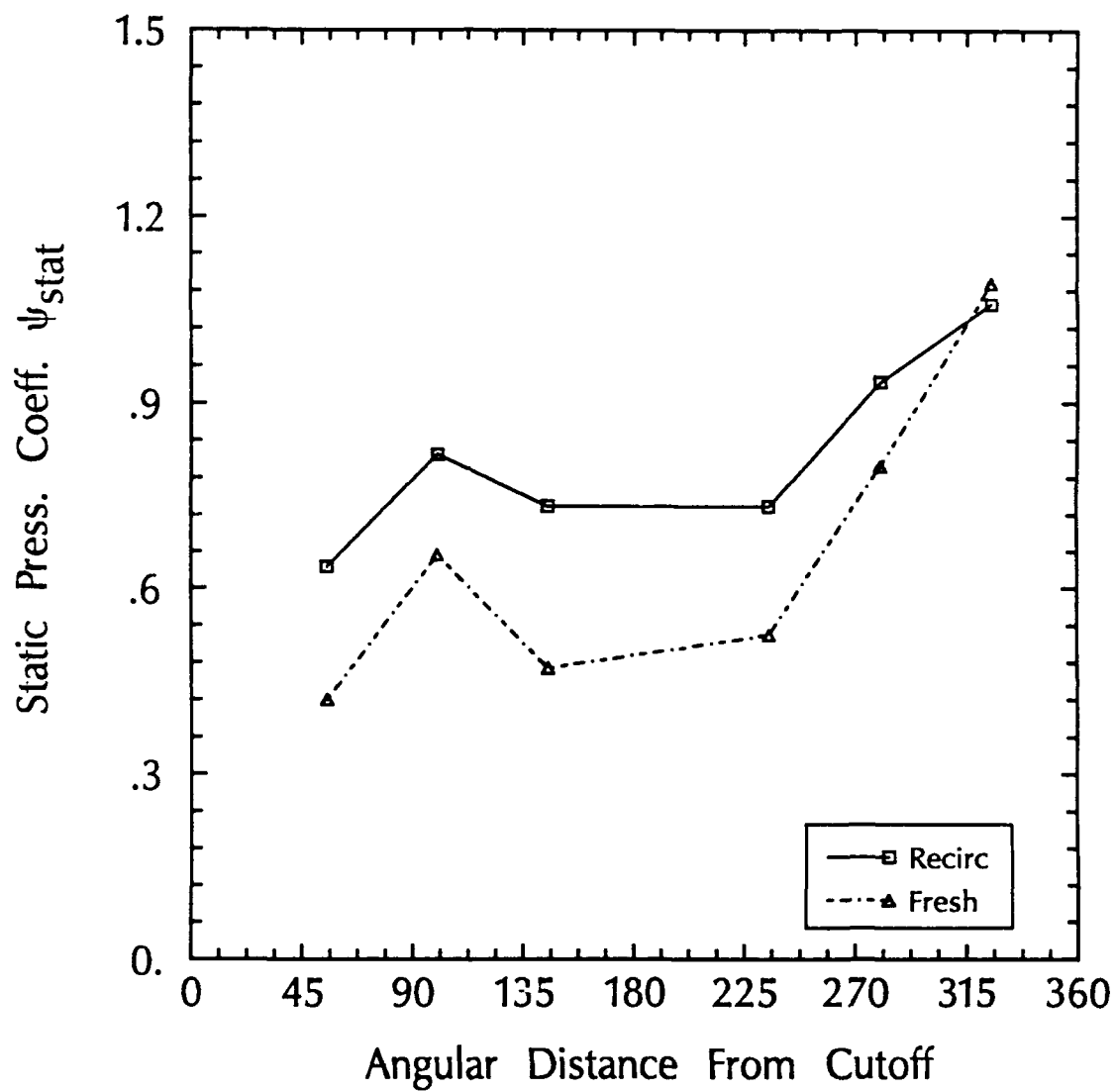


Figure 4.2 Static Pressure Coefficient at the Volute Wall as a Function of Angular Distance from Cutoff

Figure 4.3 shows a sketch of the flow as traced by dye at the blower discharge and upstream of the evaporator core. It was observed that the volute flow boundary layer separated at the blower discharge as a result of a 45° expansion angle. This separation created a circulating flow structure which trapped fluid particles in the diffuser, and impeded the flow path into the evaporator core. The recirculating flow structure reduces the heat transfer process by decreasing the amount of flow passing through the evaporator core. Several authors [22,23,29,30] suggest that expansion angles greater than 7 or 8 degrees tend to introduce severe pressure losses to a system. Therefore, the flow in the blower diffuser zone decreases overall system performance.

Figure 4.4 shows the path lines that dye followed when introduced downstream of the evaporator core with the temperature blend door open. Rather than promote uniform flow, the ductwork apparently forces the fluid to follow a complex flow path. The bulk of the flow was observed to impact the duct wall and circulate before entering the heater core zone. The dye method also allowed visualization of Von Karmen Vortex shedding off the cylindrical coolant tubing which was positioned perpendicular to the local flow direction. Both fluid impingement and vortex shedding are sources of noise in a system (see section 1.2.1); therefore, it was surmised that this region contains significant acoustic sources in addition to inefficient flow. This observation was confirmed through the acoustic experiments of a separate investigation.

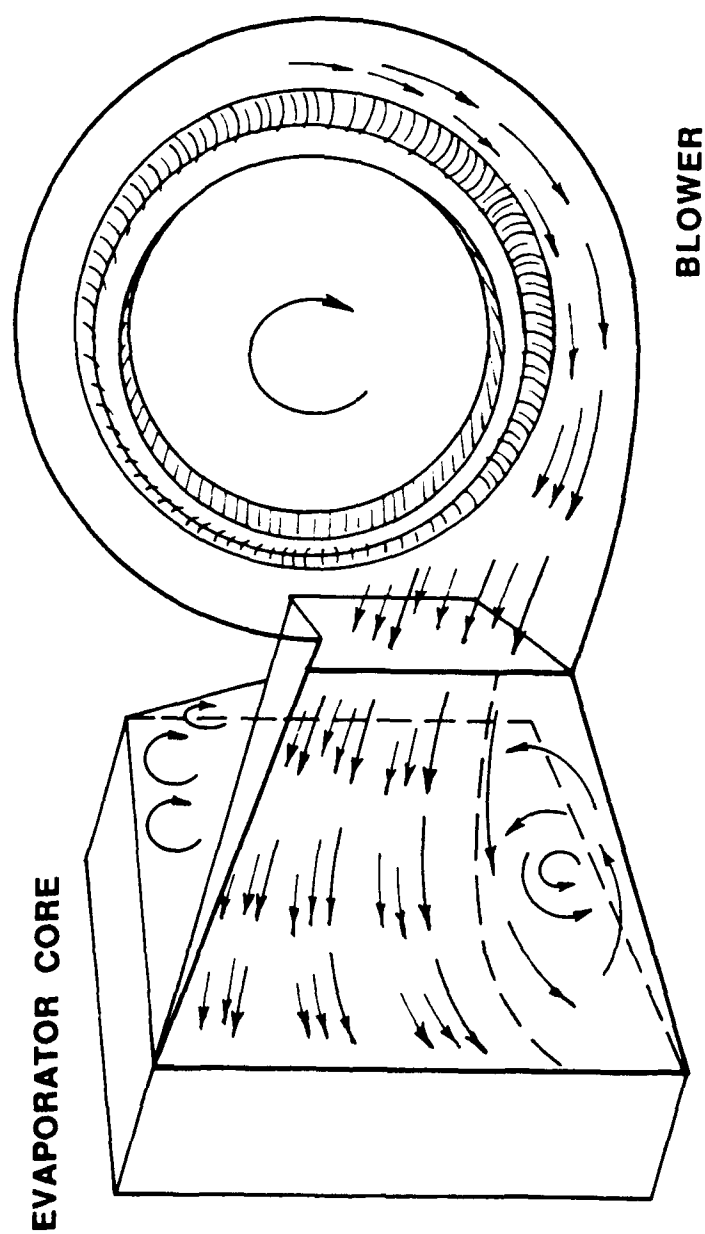


Figure 4.3 Sketch of Pathlines Traced by Dye Visualization Method, Blower Discharge

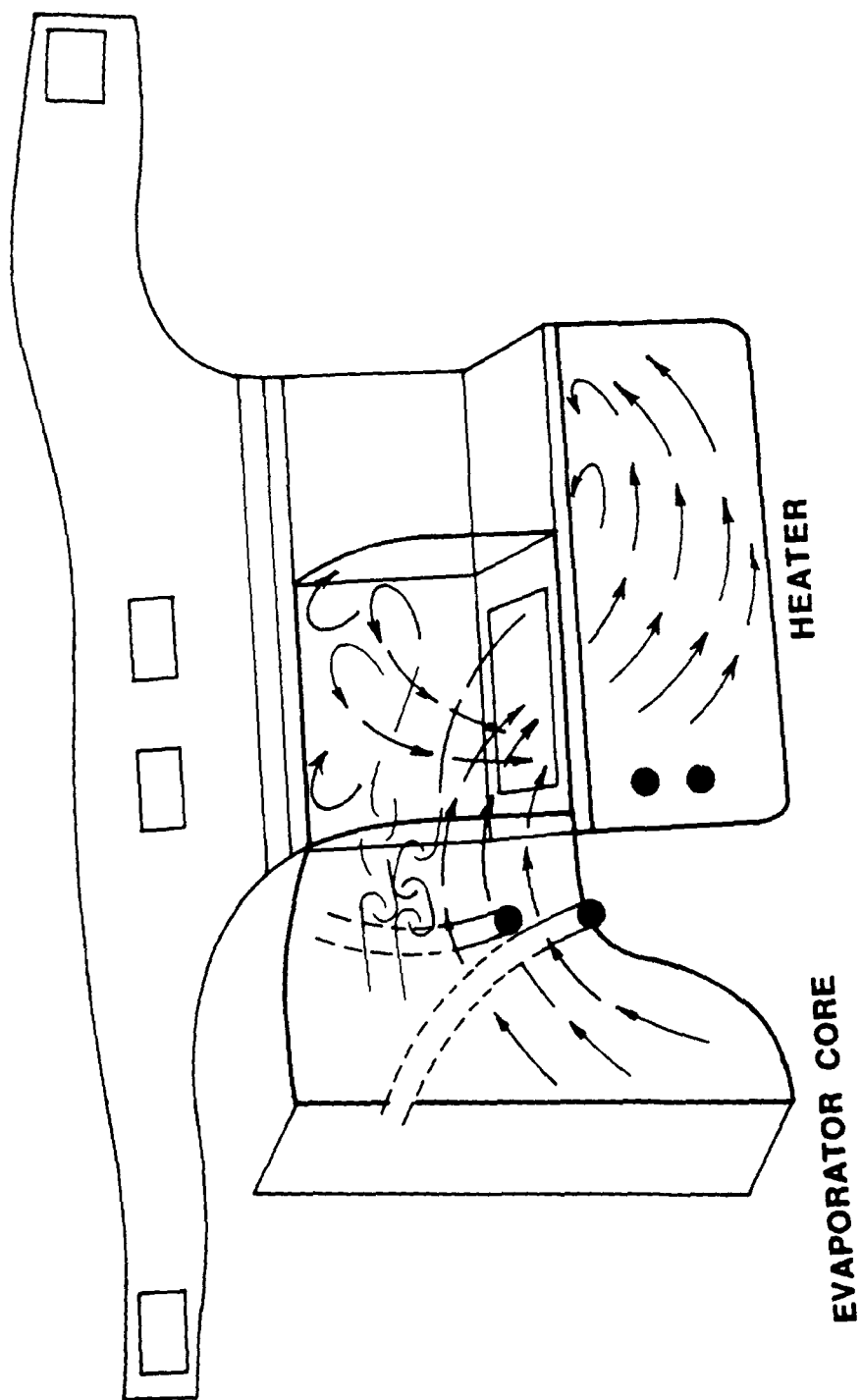


Figure 4.4 Sketch of Pathlines Traced by Dye Visualization Method, Downstream of Evaporator Core

Once the fluid passes through the heater core, it is guided through the plenum and toward the exit ducts. Figure 4.5 shows the results of dye flow visualization in this region. From this figure, it can be observed that the awkward geometries create considerable separation and stagnant flow zones. It was found that dye injected into the largest of the separation zones did not leave this area for several seconds after being introduced to the flow field. The consequence of such a flow structure is that turbulent shear layers form at the boundary between the slow and fast moving fluid. As detailed in section 1.2.1 shear layers are a predominant source of broadband noise production.

The final figure in this series, figure 4.6, shows the path lines through the transition region with the temperature blend door closed. At the high blower setting, the flow does not smoothly enter the plenum region. It was observed that the fluid separated in making the sharp 90° turn into the plenum, and again upon entering the plenum due to the sudden area expansion.

In summary, the dye visualization experiment showed that when the blower operates at a high rotation rate, the bulk of the internal flow is highly complex. In nearly every section of the system, 90° bends and sudden area expansions create significant flow separation zones. These separation zones independently may not produce profound head loss or noise production; but, when these structures act simultaneously within the system, performance is decreased while the overall noise level is increased.

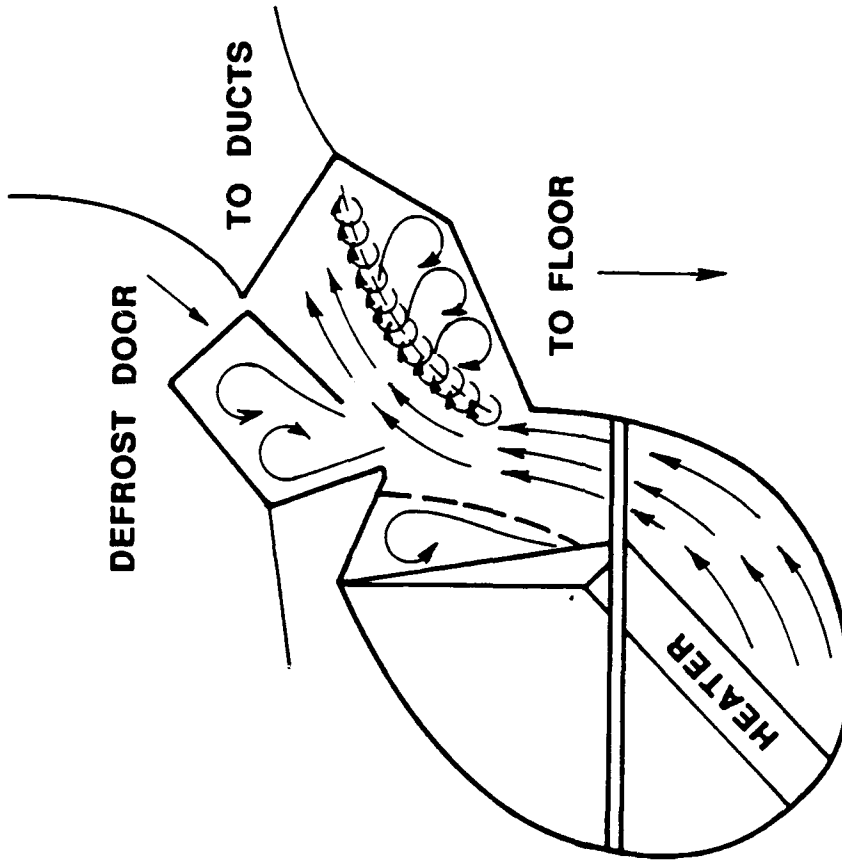


Figure 4.5 Sketch of Pathlines Traced by Dye Visualization Method, Plenum Region

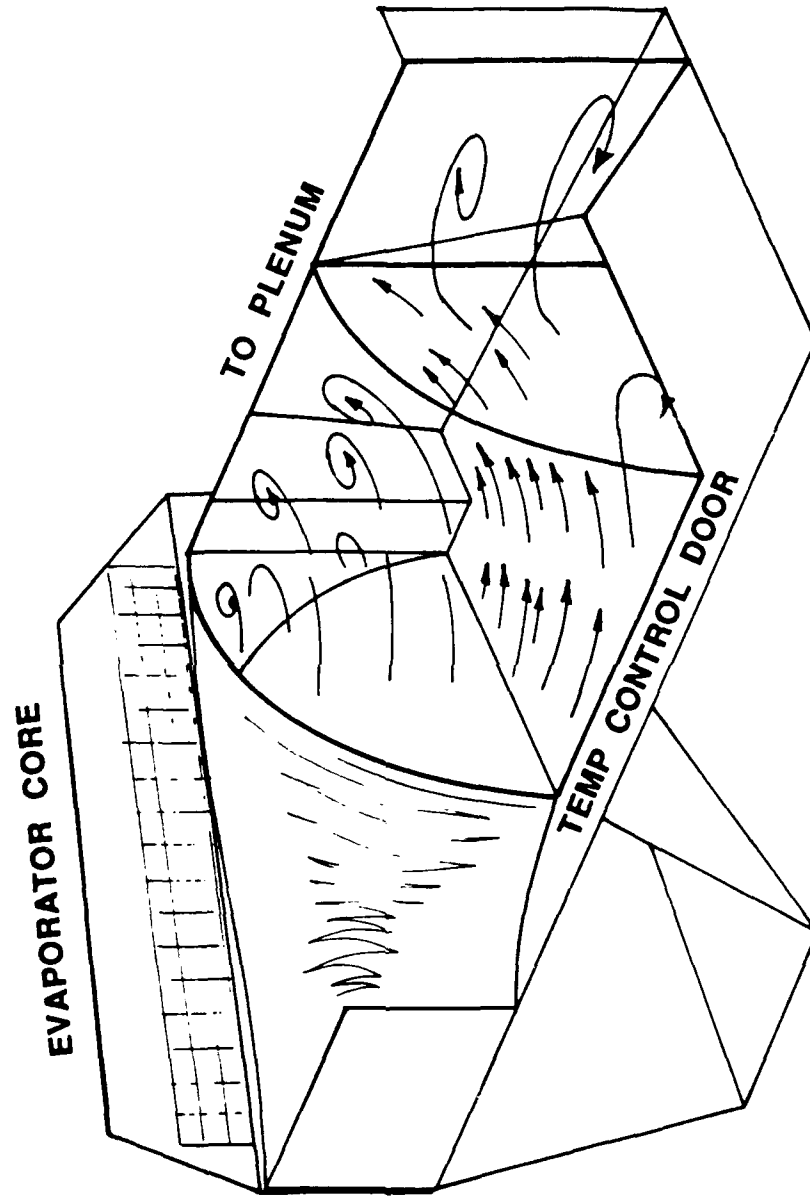


Figure 4.6 Sketch of Pathlines Traced by Dye Visualization Method, Transition Region

4.3 Velocity Flow Field in the Volute Casing

The results of the Particle Tracing Velocimetry experiment are presented in the following sections. In plots of velocity vectors, plot (a) of each figure represents the averaged velocity data as determined by the methods of sections 3.3.1 and 3.3.2. Vector plot (b) of each figure shows the interpolated vector field. It should be noted that the tank structure impeded data acquisition near the impeller, roughly 180° from the cutoff. This is reflected in the plots by the absence of velocity vectors near the impeller in the first two data sets of the lower right quadrant. The effect of this missing data is more pronounced in the interpolated vector plots as the predominantly radial flow near the impeller is not shown.

The average number of vectors per grid cell and standard deviation of the measurements are documented in table 4.1. As shown, the overall standard deviation was about 5.5 cm/s, and each cell contained roughly 100 velocity vectors.

4.3.1 Absolute Velocity Field

Several authors [9,10,32] have found that the near inlet relative velocity profiles produced by FC centrifugal blower blade passages do not exhibit the "jet-wake" flow structure typical of similar centrifugal machines. Due to this observation, it may be expected that the volute flow would not contain an appreciable

Table 4.1 Average Vector Count and Standard Deviation
Values Data Reduction Cell Blocks

Axial Location, d/W	Avg. No. of Vectors	Avg. Standard Deviation cm/s
0.186	102.7	4.95
0.372	110.5	5.12
0.558	101.7	5.50
0.744	103.1	5.78
0.930	96.8	4.94

radial velocity component in this region. This expectation was confirmed through the PTV experiment and is shown by figure 4.7, axial location $d/W = 0.186$. The majority of the volute flow is tangential, with exceptions being immediately at the impeller periphery and the cutoff region. At the cutoff, the velocity vectors indicate that the average flow direction is toward the impeller, rather than radially away. This implies that the flow is oscillating in this region, and that it is re entering the impeller. This poor flow zone is re-emphasized by the flow shown in figure 4.8. A large turbulent flow structure is present at the blades' trailing edges, upstream of the cutoff. In addition, the re-entrant, oscillating flow indicated by the data of figure 4.7 is visualized. The particle traces shown in 4.8 indicate a large vortex at the impeller periphery as well as flow instabilities along the interior of the impeller blading. The presence of the vortex also suggests that the impeller blades are stalled in this quadrant of the volute.

The averaged flow field at the non-dimensional axial distance of 0.372 is shown in figure 4.9. The flow at this axial location is very similar to that at location $d/W = 0.186$. In both figures it is shown that the volute flow is largely tangential; however, the overall flow near the impeller periphery at $d/W = 0.372$ contains a higher radial velocity component. It may be distinguished that the radial velocity component decreases with radial distance. The velocity vectors shown at the cutoff region do not flow inward, as

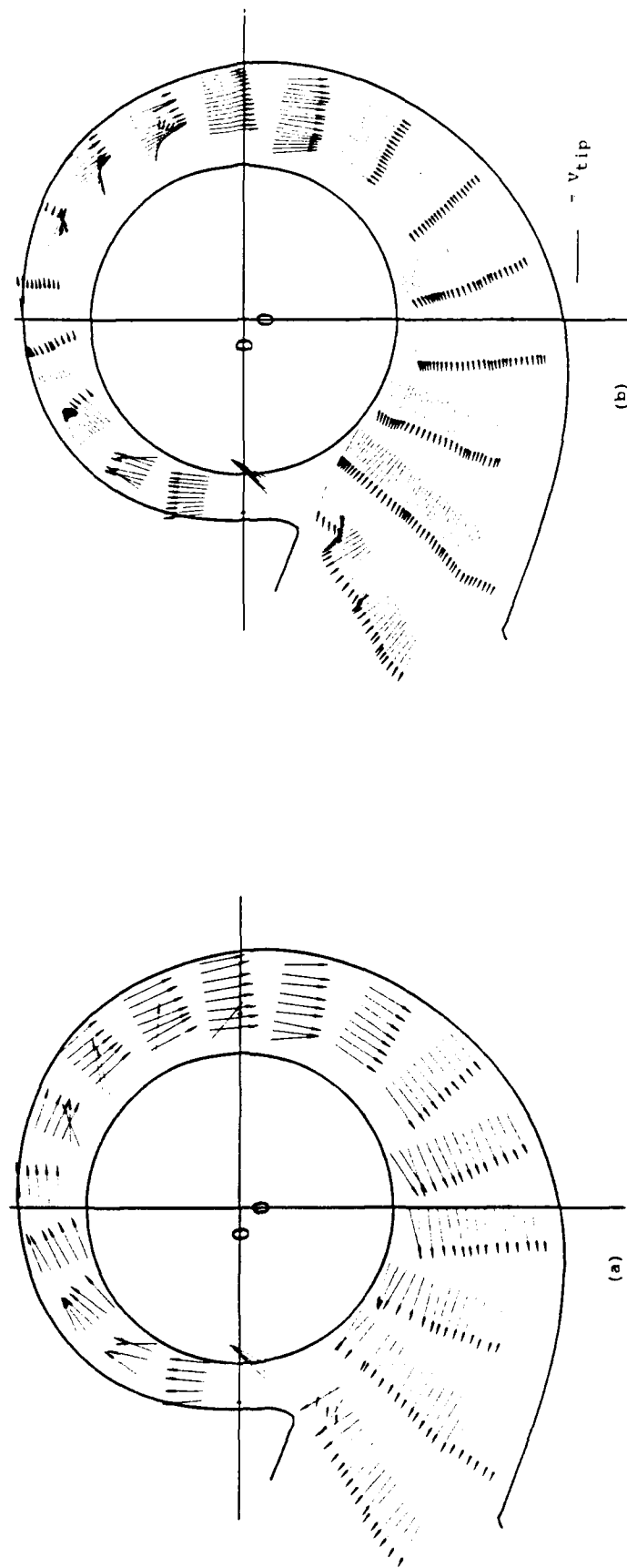


Figure 4.7 Velocity Vectors in Volute, $d/W = 0.186$
 (a) Averaged Data (b) Interpolated Data

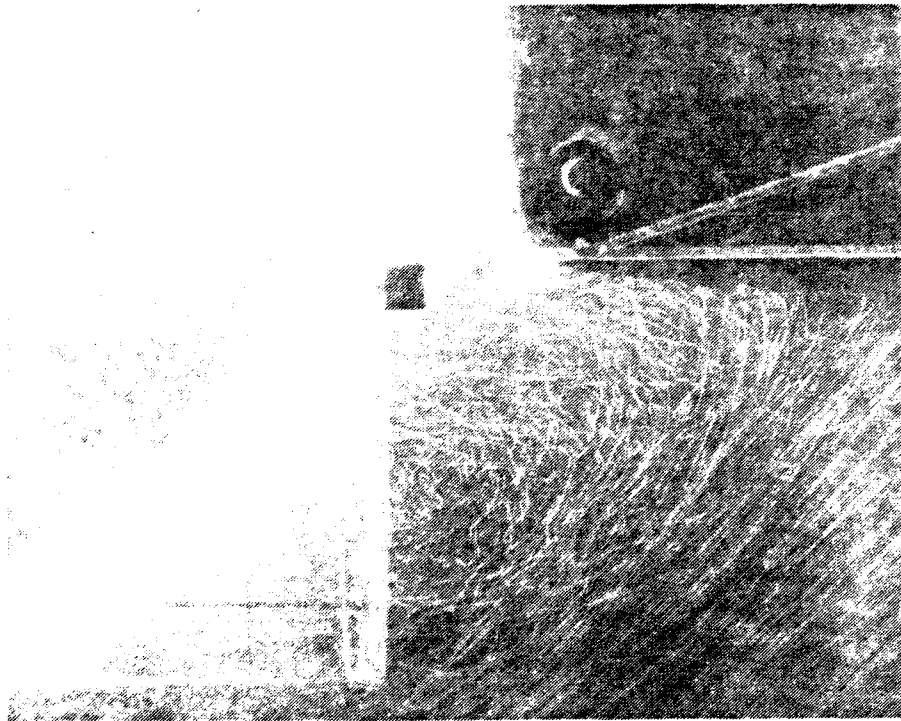


Figure 4.8 Flow Visualization of Cutoff Region, $d/W = 0.186$

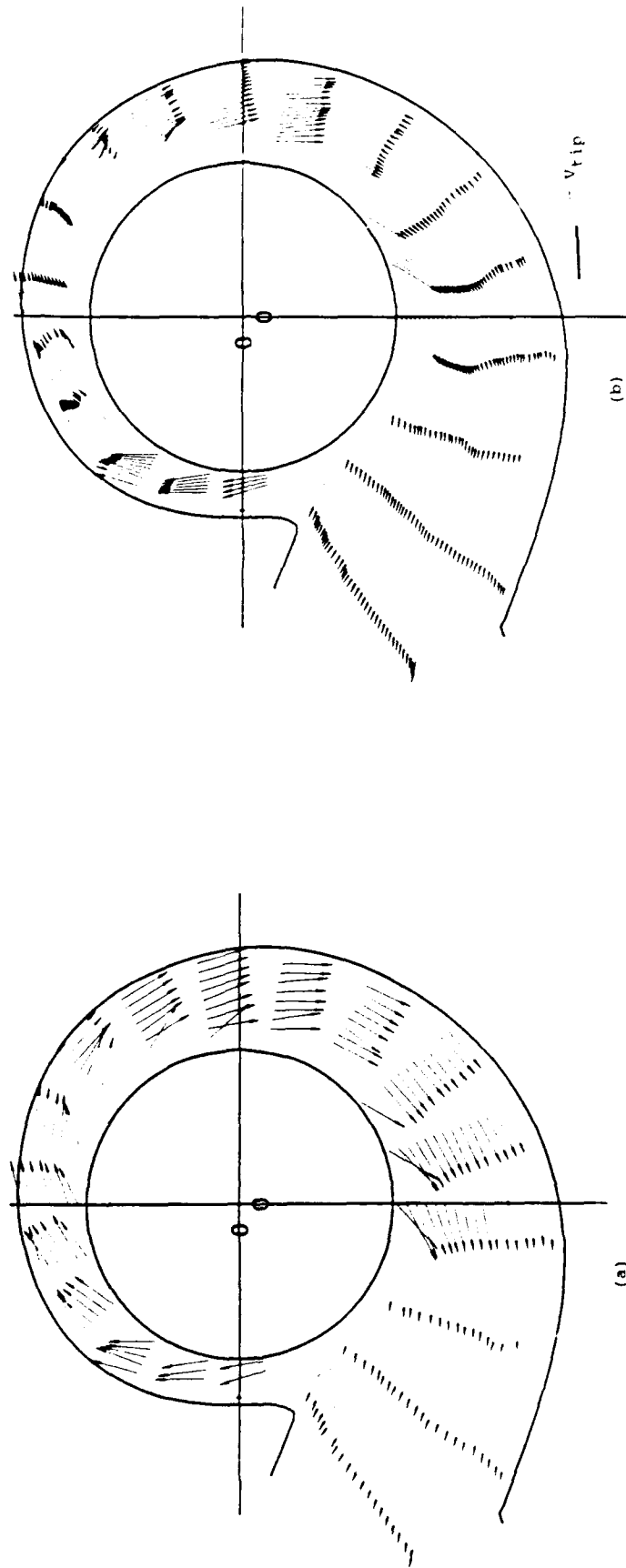


Figure 4.9 Velocity Vectors in Volute, $d/W = 0.372$
 (a) Averaged Data (b) Interpolated Data

was evident of the data presented in figure 4.7. This difference is believed to be the direct result of the amount of radial energy in the volute flow.

The radial variation of the flow field as a function of axial location can be discerned through comparison of figures 4.9, 4.10, and 4.11. These figures show that the effect of radial energy addition from the impeller on the volute flow increases with axial distance from inlet. In figures 4.10 and 4.11, it is shown that the influx of strongly radial flow appears to affect the volute flow from the impeller periphery to the outer volute casing. The axial location dependence of radial velocity suggests that the impeller blades are not uniformly loaded across the span. Typical vector magnitudes near the impeller periphery at axial locations $d/W = 0.558$, and 0.744 are greater than V_{tip} and decrease with radial distance.

Figure 4.12 shows the flow field data for an axial location behind the impeller. The data of this figure indicate that the flow is largely tangential, similar to the data shown in figure 4.7. In contrast to data presented in figures 4.9 and 4.10, the majority of the vector magnitudes are less than the impeller tip velocity.

Figures 4.13 and 4.14 are plots of the tangential and radial velocity components near the blower discharge as a function of distance from the impeller periphery. A least squares curve fit shows the axial dependence of the volute flow. The flow near the impeller inlet is largely tangential, while the measured flow at

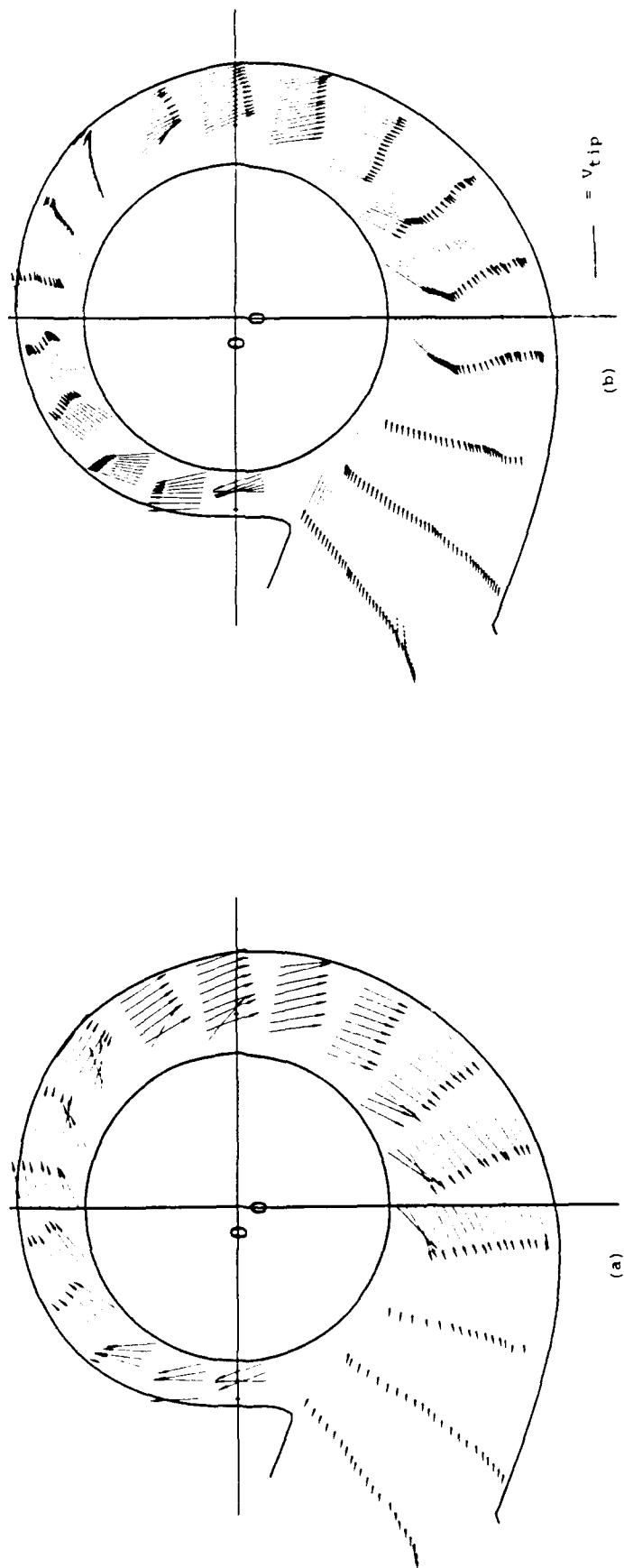


Figure 4.10 Velocity Vector : in Volute, $d/W = 0.558$
 (a) Averaged Data (b) Interpolated Data

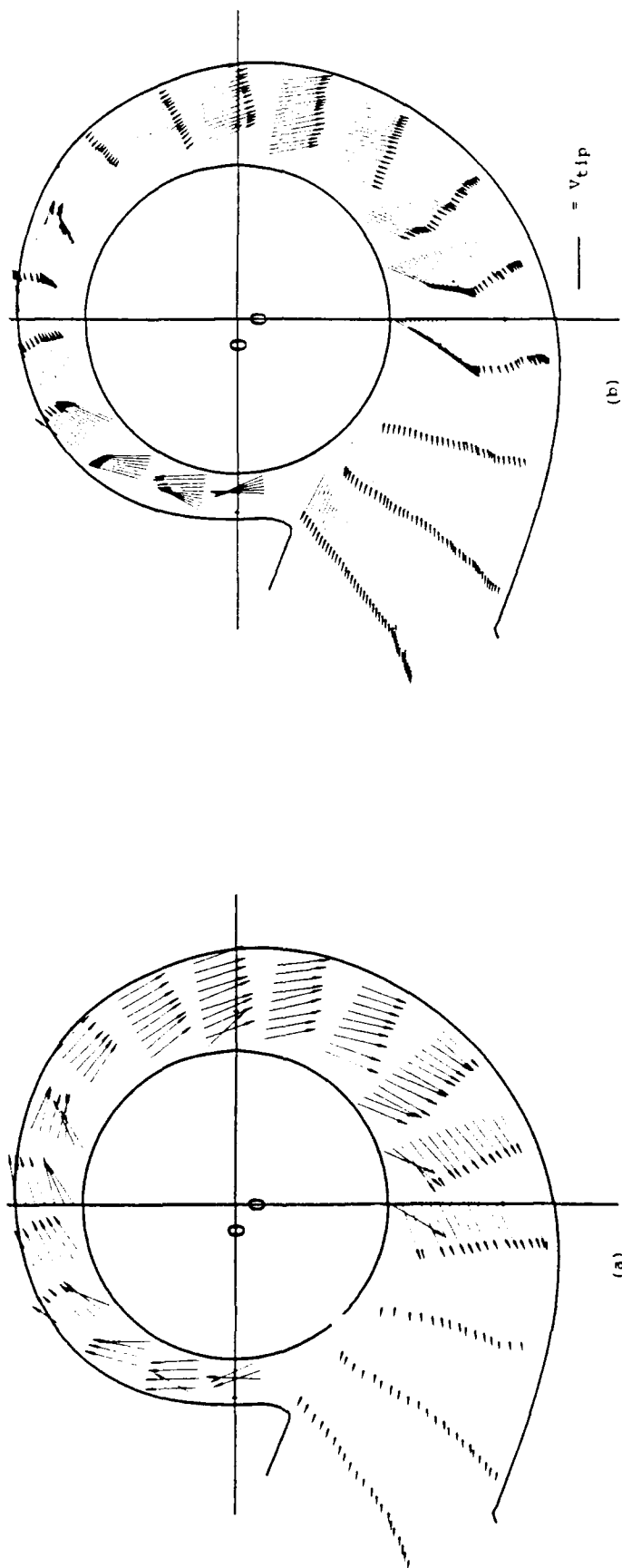


Figure 4.11 Velocity Vectors in Volute, $d/W = 0.744$
 (a) Averaged Data (b) Interpolated Data

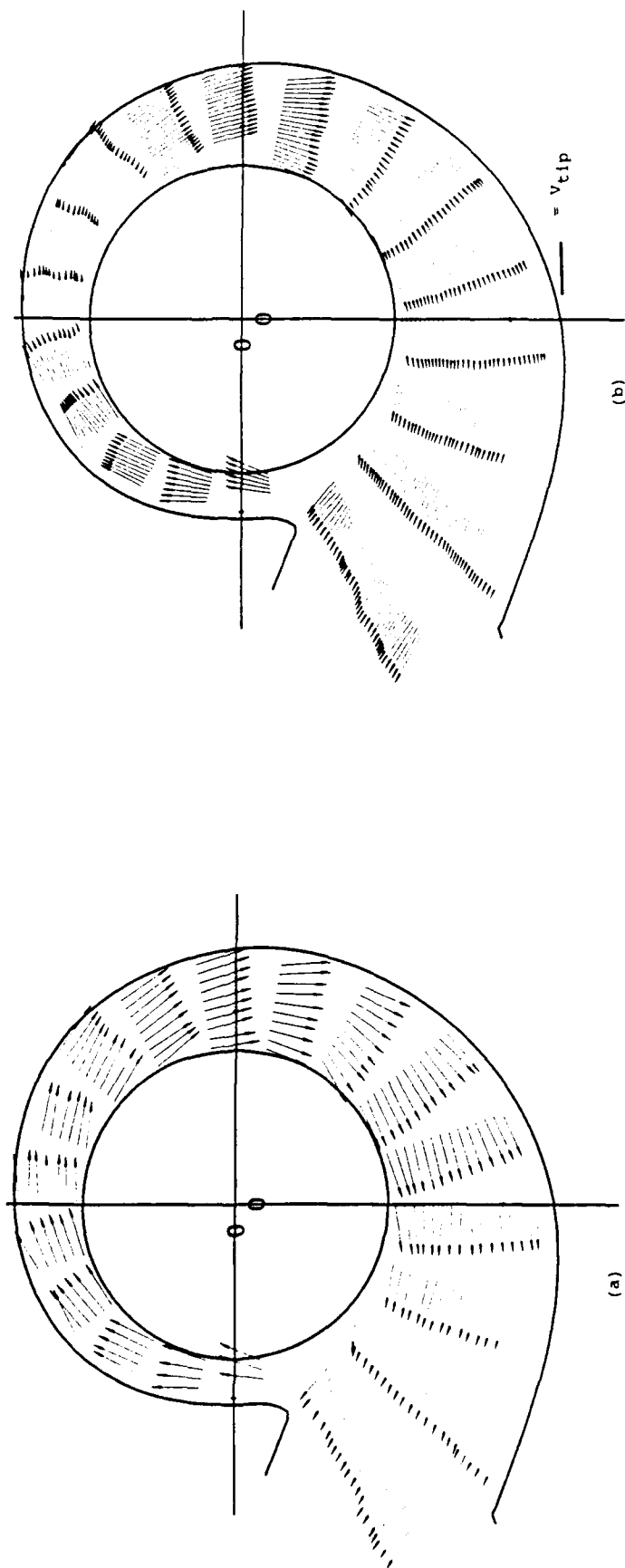


Figure 4.12 Velocity Vectors in Volute, $d/W = 0.930$
(a) Averaged Data (b) Interpolated Data

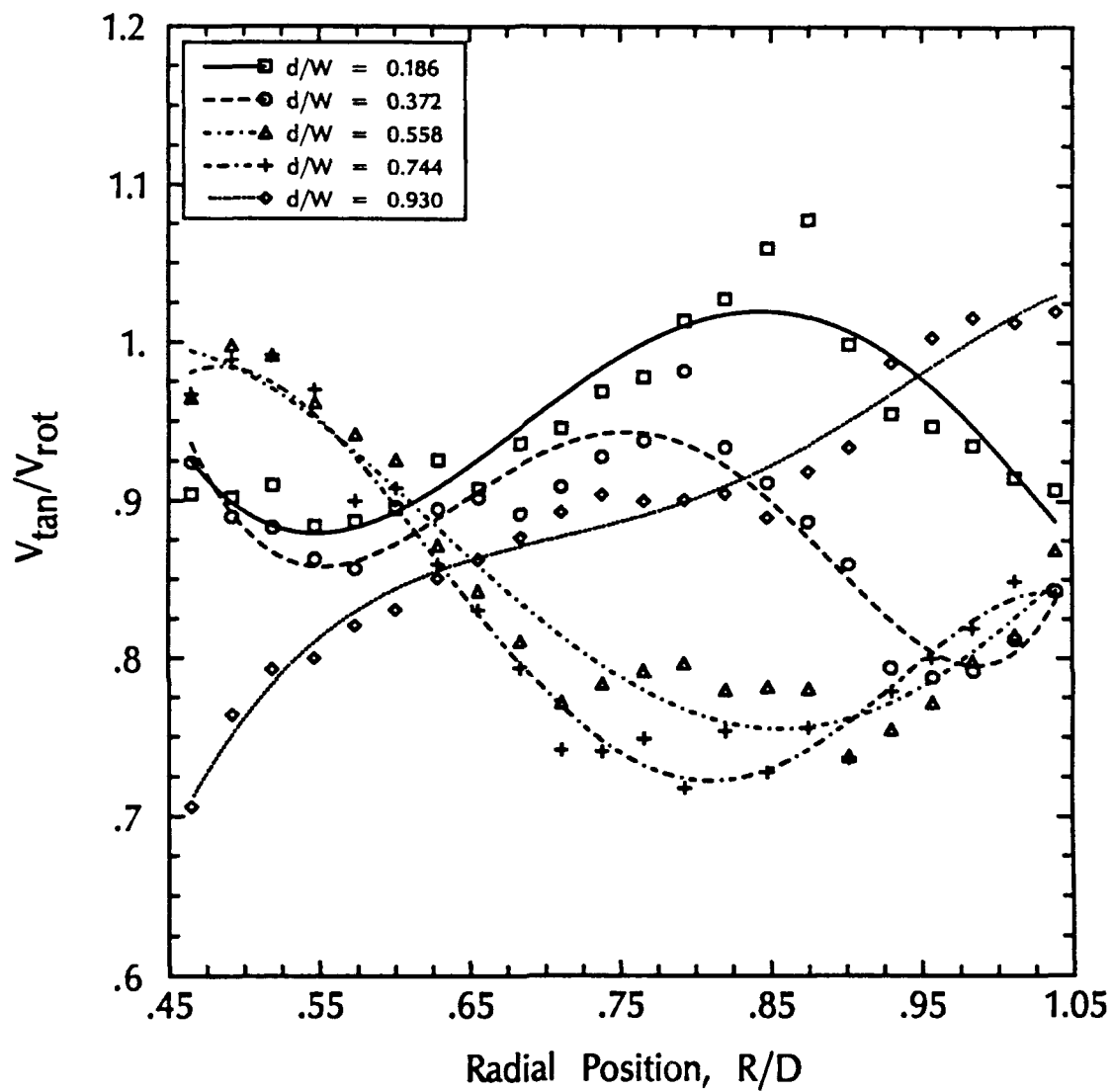


Figure 4.13 Tangential Velocity Profiles at $\theta = 320^\circ$

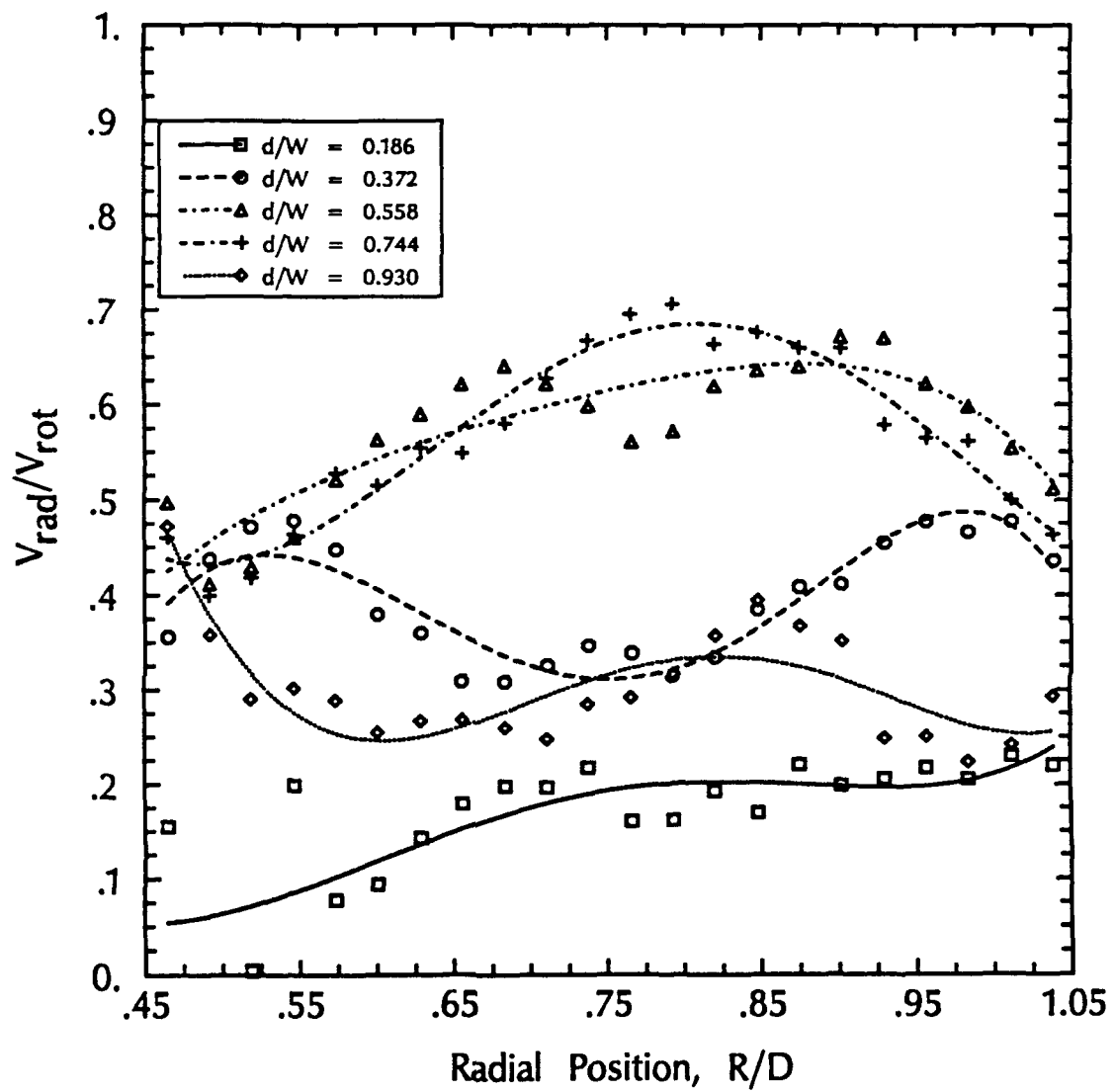


Figure 4.14 Radial Velocity Profiles at $\theta = 320^\circ$

axial locations $d/W = 0.558$ and $d/W = 0.744$ contains considerable radial velocity components. Upon closer examination of figure 4.13, it can be seen that the tangential velocity profiles at these two locations are similar to that of a free vortex flow. Specifically, the tangential velocity is inversely proportional to radial position. The data sets at the middle axial locations also indicate a diffusion process, as the magnitude of the tangential velocity component decreases with radial distance. The tangential velocity profiles for $d/W = 0.186$ and 0.372 indicate low magnitudes at the impeller periphery, presumably due to the vortex, shown in figure 4.8, which is present in this area.

At the volute discharge, the measured flow field has a high radial velocity component at the midspan locations. This can be observed through comparison of figures 4.13 and 4.14. The high radial velocity may be attributed to the flow leaving the volute and turning/expanding into the diffuser. The largely tangential flow of the outer locations tends to re-enter the volute flow at the cutoff, rather than exiting the unit.

4.3.2 Relative Velocity Field

In turbomachinery, the relative, or blade-fixed flow field often provides more useful performance information about performance than the absolute (inertial) flow field. Typically, the relative flow field at blade discharge is characterized by a "jet-wake" flow

profile. The present study was concerned with the entire volute flow, rather than only the flow at the blade discharge. In the PTV method, the absolute flow field data were taken at random times, as opposed to synchronized times, in order to determine the overall steady state characteristics. The relative flow field data can be determined by subtracting the tip velocity of the impeller from the tangential component of the absolute velocity vector. In equation form:

$$V_{rel} = V_{rad}r + (V_{tan} - V_{tip})\theta \quad (4.1)$$

In the image derotator experiment, qualitative information about the instantaneous relative velocity field through the blade passages was obtained. The following sections describe the relative flow as determined by these two methods.

As shown in figure 4.7, the absolute volute flow near the inlet ($d/W=0.186$) is largely tangential. Raj [9] and Yeager [10] have shown that the blade exit velocity profile in this region is nearly linear, thus indicating that little energy is being transferred from the impeller to the working fluid. It may be speculated that the near-inlet volute flow is induced in part by fluid entrainment caused by viscous stresses acting between the impeller blading and volute fluid. This zone may also contain considerable secondary flows such as Cau and Mandas [13] document. Figure 4.15 shows the steady state relative flow at axial location $d/W = 0.186$. The velocity vectors in the upper left quadrant

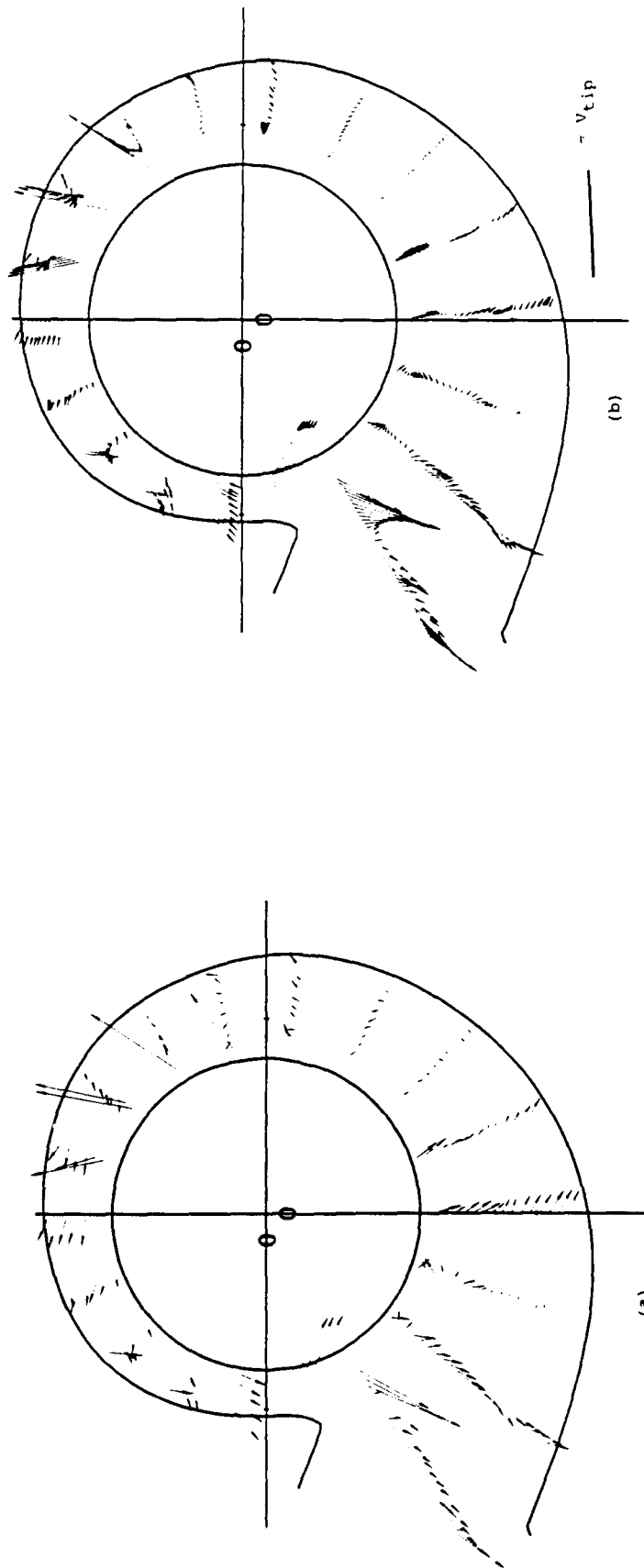


Figure 4.15 Relative Velocity Vectors in Volute, $d/W = 0.186$
(a) Averaged Data (b) Interpolated Data

clearly indicate that the flow is slower than the impeller tip speed. Further, the observed "re-entrant" flow is shown at the scroll cutoff. The majority of the velocity vectors indicate low radial velocity, with the exception being at the unit discharge.

The relative flow becomes more radial as the axial distance from inlet increases. This characteristic may be seen by comparison of the near discharge flow of figures 4.15 and 4.16, axial locations $d/W = 0.186$ and 0.372 , respectively. It appears that the majority of the radial energy transfer comes from the lower portion of the impeller, where velocity vectors indicate a predominantly radial flow. Similar to the near inlet flow, the upper left quadrant of figure 4.16 indicates velocities less than the impeller tip speed.

Figures 4.17 and 4.18 show the relative flow at axial locations $d/W = 0.558$ and $d/W = 0.744$, respectively. As shown, the volute flow is highly radial, which indicates radial energy transfer from the impeller to the fluid.

Figure 4.19 shows the relative velocity field behind the impeller. In agreement with the data shown in figure 4.14, the majority of the flow is tangential to the impeller periphery. It is also shown that the relative flow is slightly slower than the tip speed. At this location, a "re-entrant" flow is shown at the cutoff. However, this region is behind the impeller and the blades are not performing work on the fluid here. These data points thus indicate that the flow is oscillating in this area, rather than "re-entering" the impeller. It is presumed the sudden area contraction

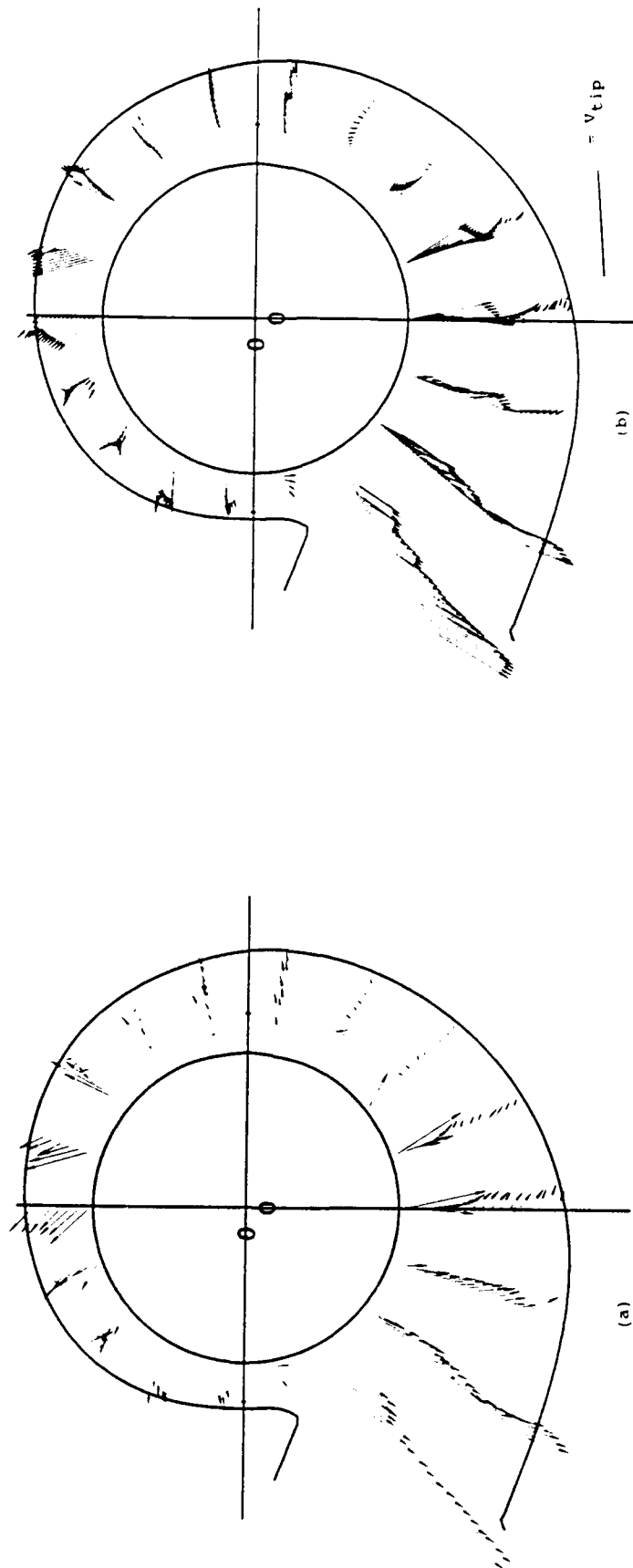


Figure 4.16 Relative Velocity Vectors in Volute, $d/W = 0.372$
 (a) Averaged Data (b) Interpolated Data

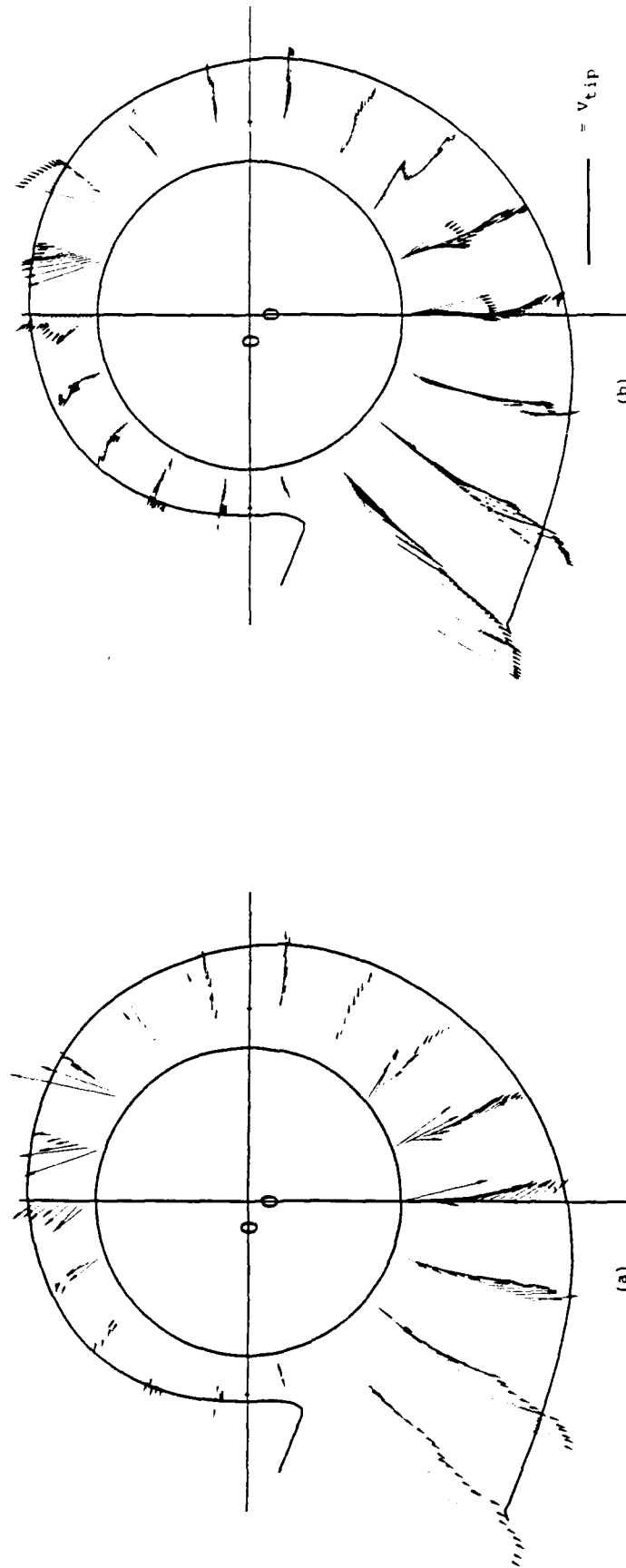


Figure 4.17 Relative Velocity Vectors in Volute, $d/W = 0.558$
 (a) Averaged Data (b) Interpolated Data

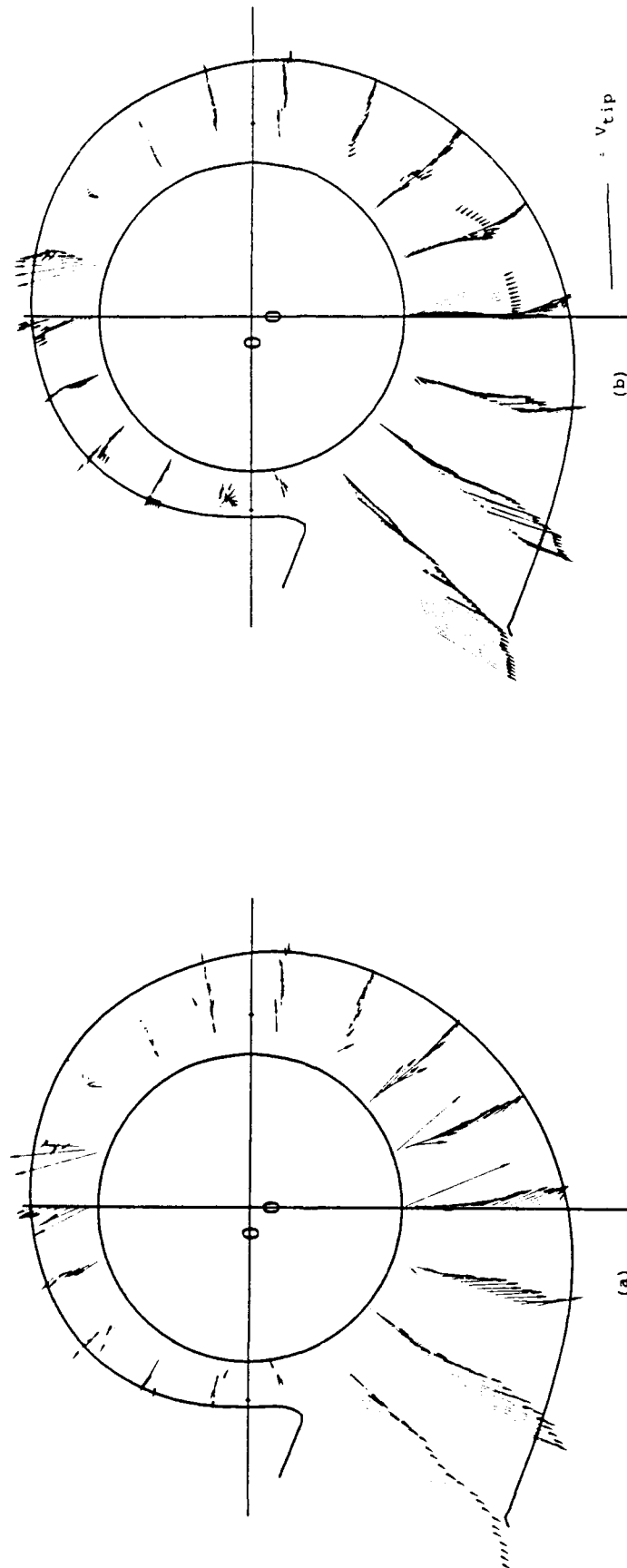


Figure 4.18 Relative Velocity Vectors in Volute, $d/W = 0.744$
 (a) Averaged Data (b) Interpolated Data

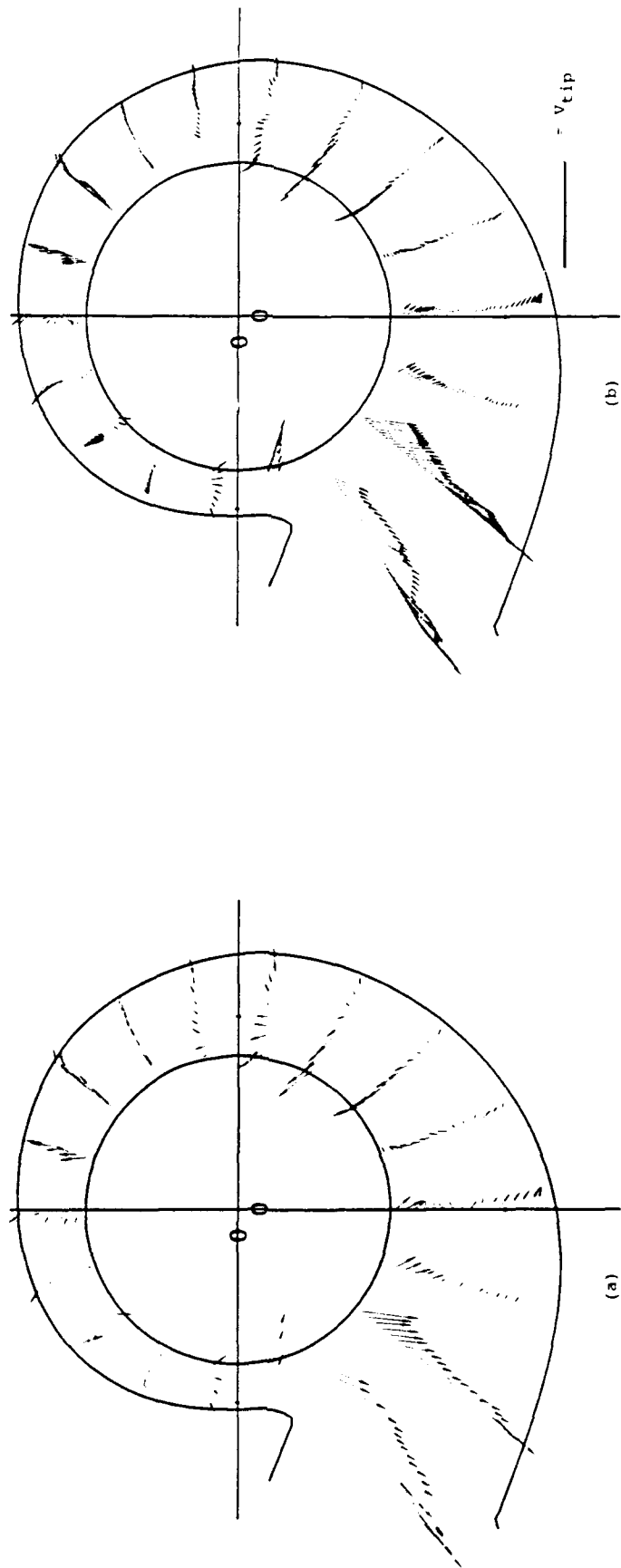


Figure 4.19 Relative Velocity Vectors in Volute, $d/W = 0.930$
 (a) Averaged Data (b) Interpolated Data

from discharge to cutoff forces the tangential volute flow inward instead of out through the discharge.

4.4 Visualization of the Relative Flow Field

The following sections document the relative flow over the hub region and within the impeller blade passages as visualized via the particle tracing and image derotator technique. Data is presented for operation in both inlet modes at axial locations $d/W = 0.186$ and $d/W = 0.372$.

4.4.1 Fresh Inlet Mode

The following sequences of photographs were taken with the inlet condition set to model the "fresh" mode. The exposure time was $1/8$ s. Successive photographs have some overlap in field of view. The angular locations are measured clockwise from the cutoff.

Figure 4.20 shows the cutoff relative flow at axial location $d/W = 0.186$. High incidence is the predominant flow characteristic. The presence of particle "spots" on the interior of the impeller slightly left of center (LOC) imply that the flow here has velocity $O(V_{tip})$. Observations of the flow from an inertial point of view indicate a re-entrant flow in this region, and the data presented in section 4.3 agree with the flow shown in figure 4.20. Thus, the

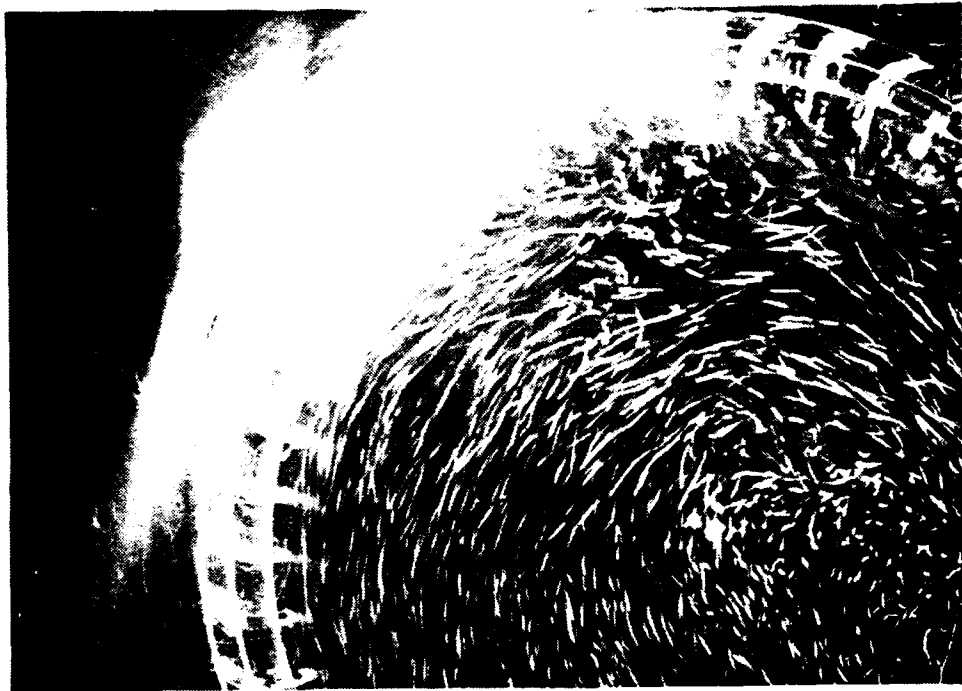


Figure 4.20 Visualization of the Cutoff Relative Flow
Inlet Mode: "fresh", $d/W = 0.186$

particle traces which indicate a local flow disturbance at the cutoff are interpreted as a re-entrant flow.

Figure 4.21 shows particle streak data which reemphasize the above argument. At the lower left interior of the impeller, particle streaks indicate poor flow through the blade passages. The flow paths in this region do not follow the vortex-like relative hub flow. At right, particle traces indicate a recirculating flow cell. The poor blade inlet flow generated by the chaotic hub flow results in poor flow through the blade passages. The effect of this is a volute flow with low kinetic energy and no obvious direction or structure.

Figure 4.22 shows the relative flow at $d/W = 0.186$ and $60^\circ < \theta < 200^\circ$. Slightly ROC, a rotating stall cell appears to be traced by the seed particles. This cell significantly disturbs the hub flow and subsequently results in poor blade inlet flow. The volute flow reflects poor blade performance as particle traces indicate low kinetic energy and no flow structure.

Figure 4.23 shows the relative flow at the location $110^\circ < \theta < 250^\circ$. A region of recirculation is found in the center of the figure. Particle traces indicate extensive blade passage flow separation which results in low through flow. The volute flow appears to have low kinetic energy.

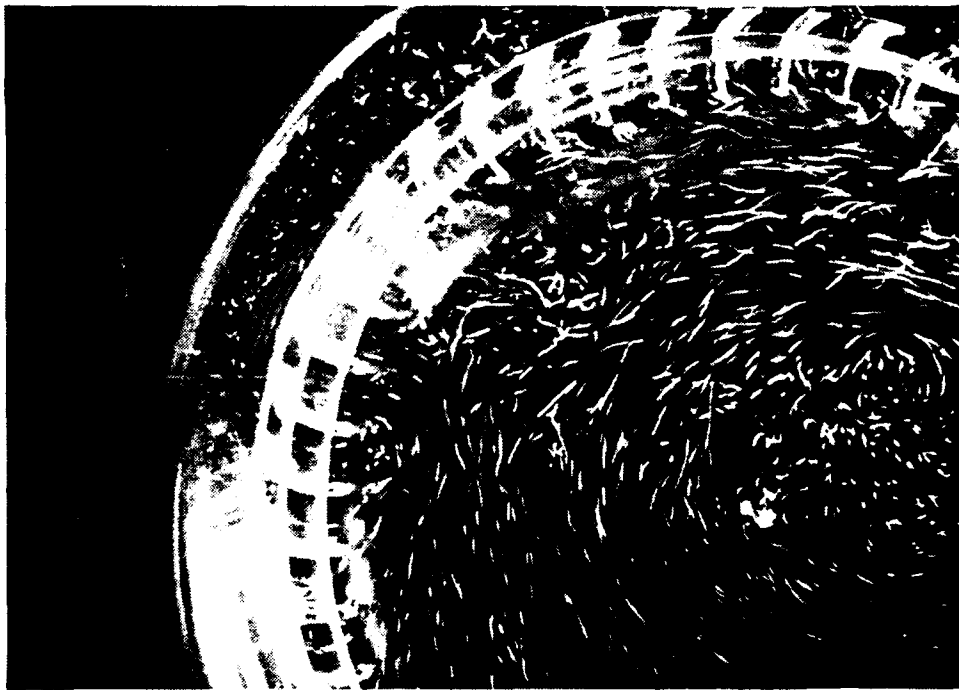


Figure 4.21 Visualization of the Relative Flow
Inlet Mode: "fresh", $d/W = 0.186$, $10^\circ < \theta < 150^\circ$

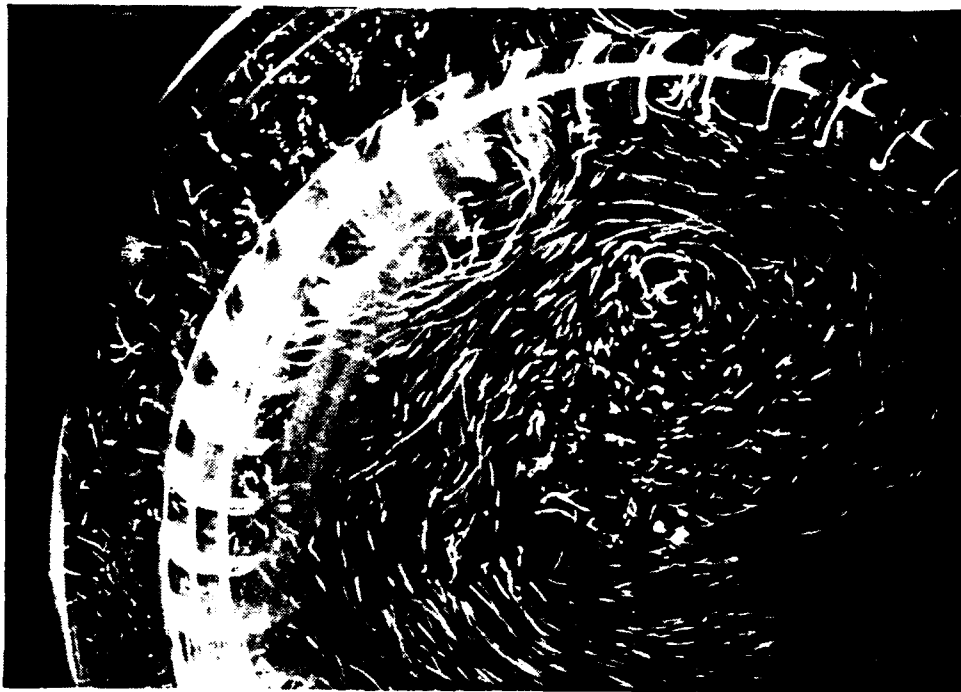


Figure 4.22 Visualization of the Relative Flow
Inlet Mode: "fresh", $d/W = 0.186$, $60^\circ < \theta < 200^\circ$

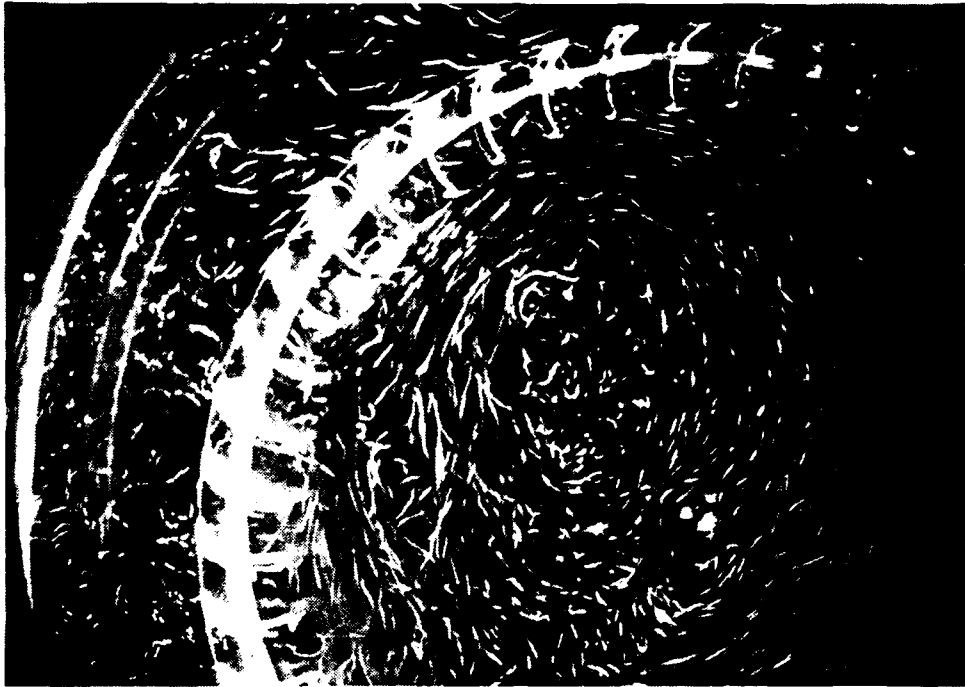


Figure 4.23 Visualization of the Relative Flow
Inlet Mode: "fresh", $d/W = 0.186$, $110^\circ < \theta < 250^\circ$

Figure 4.24 shows the flow at the location $160^\circ < \theta < 300^\circ$. The rotating stall cell is shown in the center of the figure, right side of the impeller. Blade passage stall is apparent at ROC locations, while the LOC particle streaks indicate a more streamline flow. The volute flow has low radial energy and no evidence of a "jet-wake" flow structure. Particle streaks indicate tangential flow at the impeller periphery. As documented in section 4.3, the volute flow reflects little or no energy addition from the impeller.

Figure 4.25 shows the flow in the region $260^\circ < \theta < 40^\circ$. In this figure, the volute discharge is at the bottom, center to right. Particle streaks over the hub region indicate a fairly uniform flow. The hub flow may be described as a vortex flow, opposite in direction to the direction of impeller rotation. The volute flow is turbulent at top, ROC. This visualization agrees with inertial observations which indicate trailing edge vortices in this region. No obvious jet-wake flow structure is present in this area.

The next sequence of photographs shows the relative flow at axial location $d/W = 0.372$, "fresh" inlet mode. The exposure time was fixed at $1/8s$. Figure 4.26 shows the relative flow at the discharge (lower left) and at the cutoff (top, LOC). Particle streaks trace out smooth pathlines at the discharge, and high incidence does not correlate with blade flow separation. A "jet-wake" flow may also be discerned at the discharge region. At the cutoff, a disturbance at the blade inlet is shown which may be indicative of re-entrant flow. The hub flow appears to be free of

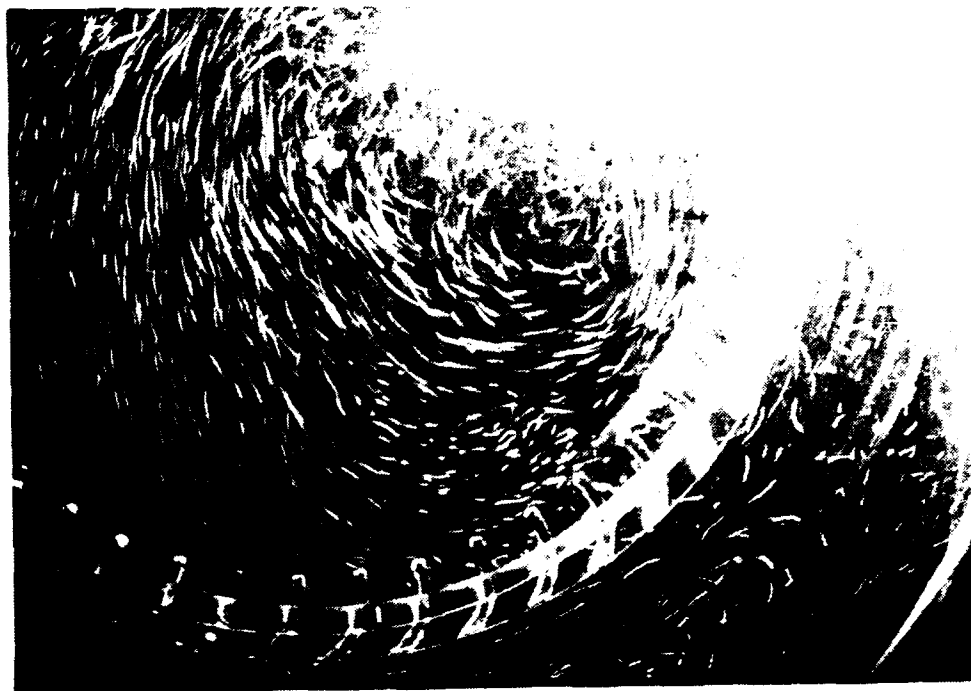


Figure 4.24 Visualization of the Relative Flow
Inlet Mode: "fresh", $d/W = 0.186$, $160^\circ < \theta < 300^\circ$

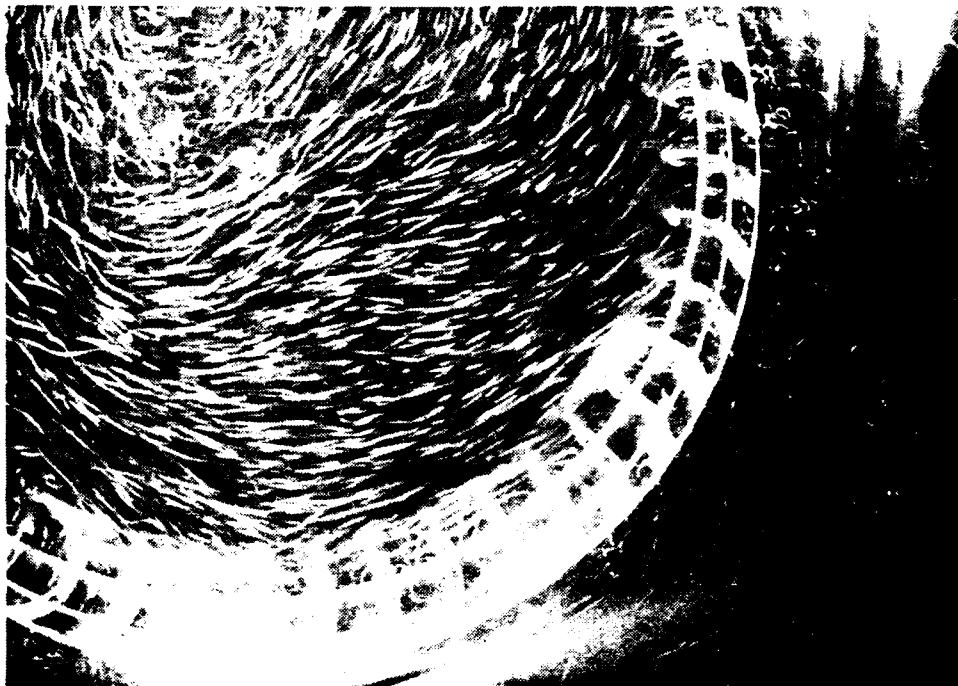


Figure 4.25 Visualization of the Relative Flow
Inlet Mode: "fresh", $d/W = 0.186$, $260^\circ < \theta < 40^\circ$



Figure 4.26 Visualization of the Cutoff Relative Flow
Inlet Mode: "fresh", $d/W = 0.372$

any large disturbances.

Figure 4.27 shows the relative flow at circumferential location $40^\circ < \theta < 180^\circ$. At the instant the photograph was taken, this region contained several stalled blade passages. The relative volute flow appears have significant radial velocity. This result agrees with the data shown in section 4.3. Similar to axial location $d/W = 0.186$, the hub flow generates high incidence which correlates with blade suction side flow separation.

Figure 4.28 shows the flow at the location $110^\circ < \theta < 250^\circ$. The flow contains all of the previously mentioned characteristics and the volute flow appears to be highly turbulent.

Figures 4.29 and 4.30 show the flow field at $160^\circ < \theta < 300^\circ$ and $210^\circ < \theta < 350^\circ$, respectively. Comparison of these two figures allows the transition from stalled blade passage flow to more efficient jet-wake flow to be observed. The upper ROC zone of figure 4.29 is an example of turbulent, separated flow in both the blade passages and volute. The lower blade passages of figure 4.29 and the majority of the particle traces in figure 4.30 indicate smooth, stream-like flow. The effect of smooth blade passage flow is the jet-wake structure evident in the volute flow. This suggests that the impeller is performing work on the fluid in this region. Through comparison of the two figures, it can be seen that the quality of hub flow significantly affects the blade passage and volute flow.

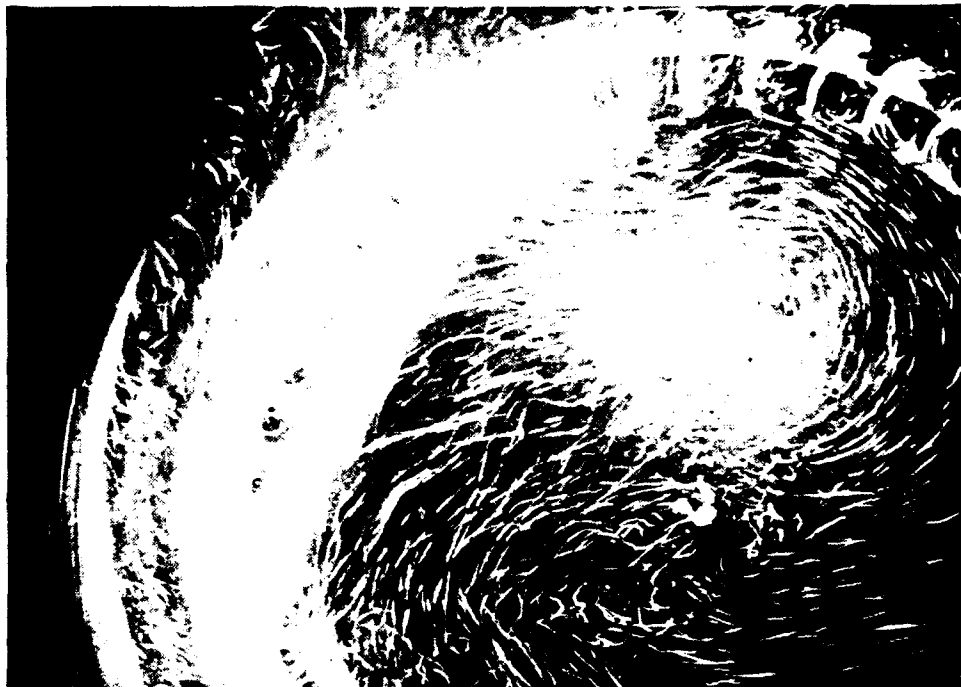


Figure 4.27 Visualization of the Relative Flow
Inlet Mode: "fresh", $d/W = 0.186$, $40^\circ < \theta < 180^\circ$



Figure 4.28 Visualization of the Relative Flow
Inlet Mode: "fresh", $d/W = 0.186$, $110^\circ < \theta < 250^\circ$

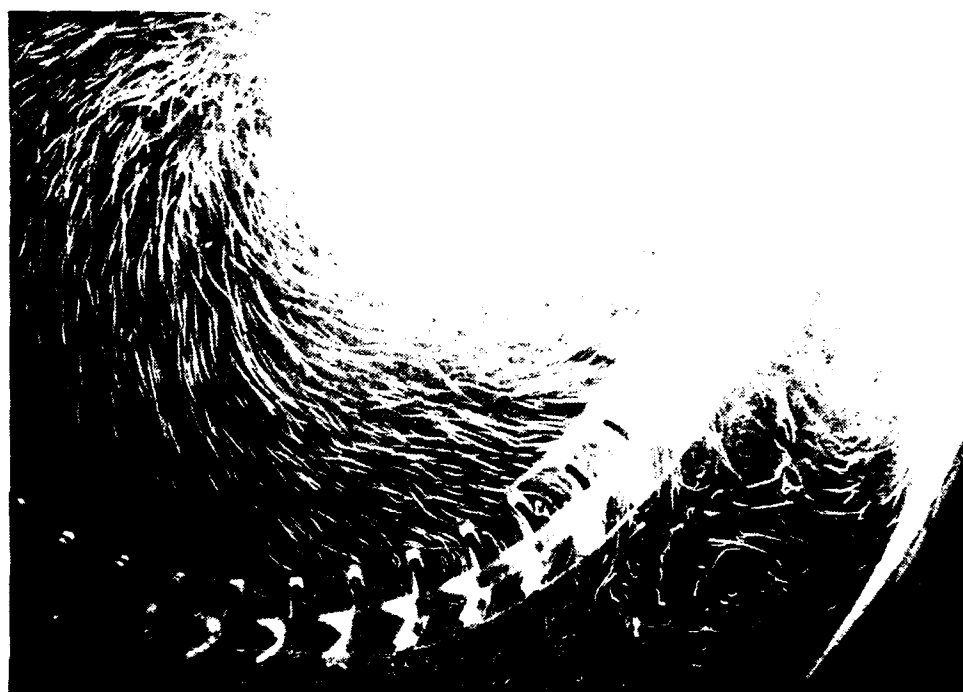


Figure 4.29 Visualization of the Relative Flow
Inlet Mode: "fresh", $d/W = 0.186$, $160^\circ < \theta < 300^\circ$

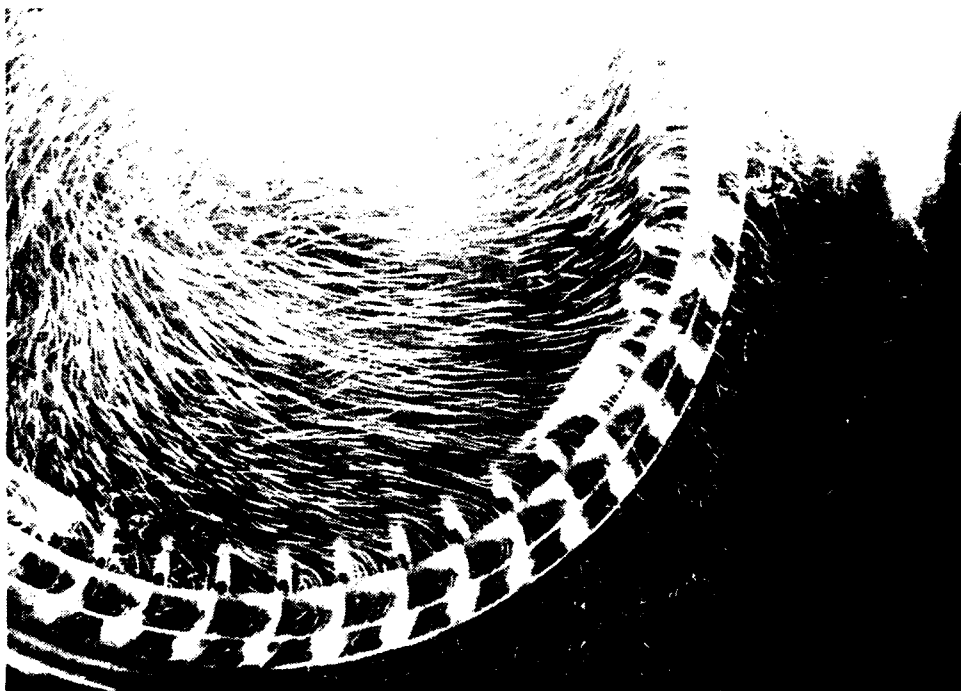


Figure 4.30 Visualization of the Relative Flow
Inlet Mode: "fresh", $d/W = 0.186$, $210^\circ < \theta < 350^\circ$

4.4.2 Recirc Inlet Mode

The next sequence of figures are 1/4 s exposure photographs of the relative flow field with the unit operating under "recirc" mode and the laser sheet positioned at $d/W = 0.186$. The volute casing is the bright outer arc.

Figure 4.31 shows the relative flow near the volute cutoff. The particle path traces over the hub region indicate that the flow is entering the blade passages with high incidence. This is the result of the inlet flow having little or no rotational velocity as compared to the blade rotational rate. In this region, high incidence correlates with separated flow over the blade suction side. The net effect of this condition is reduced throughflow and performance. The particle streak data indicates that the tangential velocity component of the fluid within the volute is highest at the impeller periphery and decreases with radial distance. Particle paths indicate a considerable radial velocity component, presumably due to the addition of radial energy by the impeller.

Figure 4.32 shows the relative flow at the circumferential location of $90^\circ < \theta < 200^\circ$ as measured in the direction of rotation, with the cutoff being 0° . Many of the same flow characteristics of figure 4.31 are shown at this location. However, particle path line data indicate that the incidence angles are not as great.

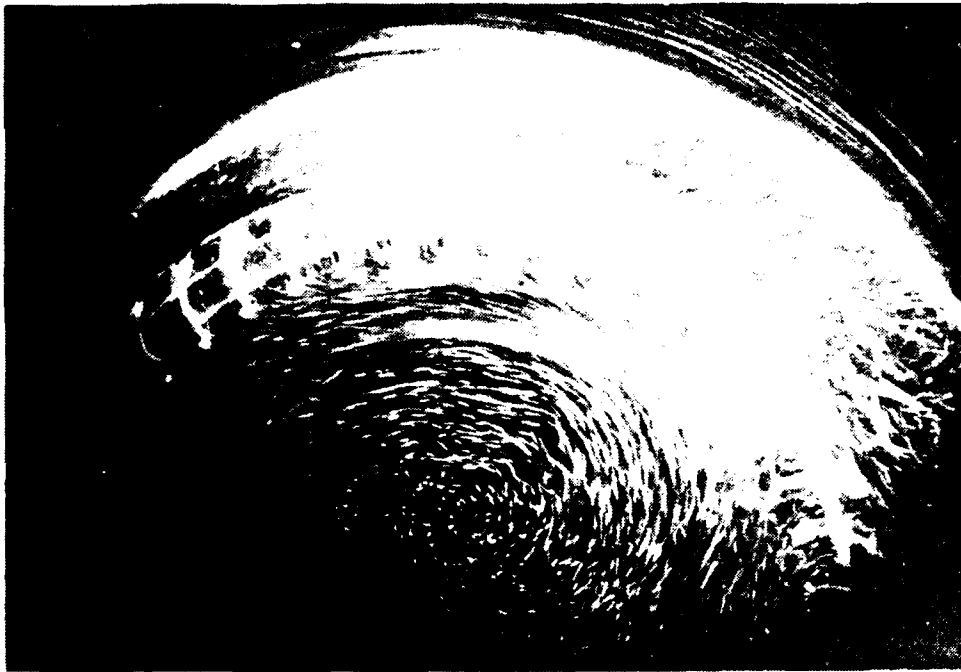


Figure 4.31 Visualization of the Cutoff Relative Flow,
Inlet Mode: "recirc", $d/W = 0.186$, $10^\circ < \theta < 150^\circ$

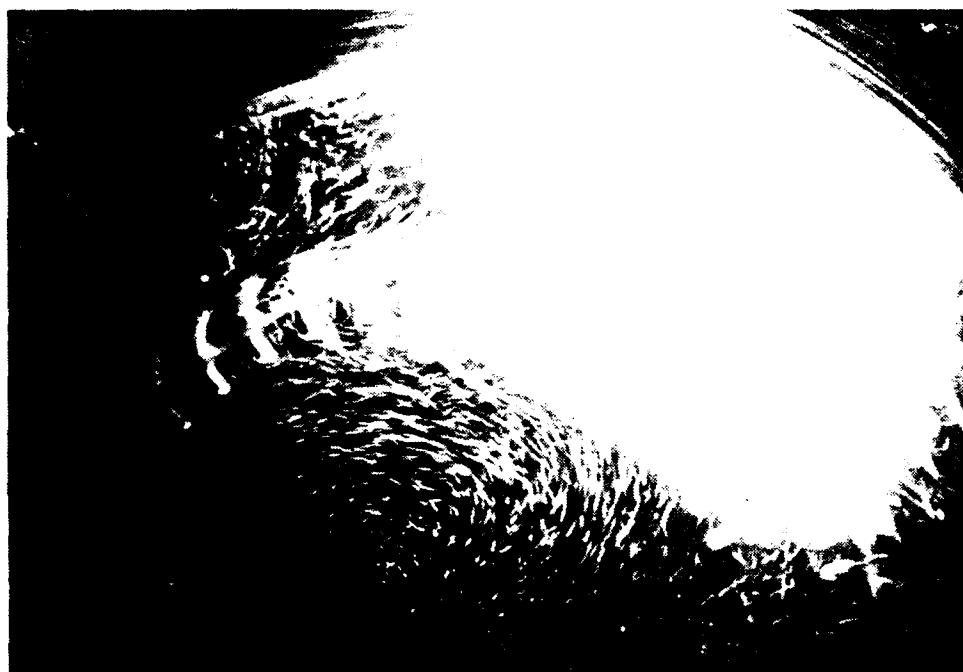


Figure 4.32 Visualization of the Relative Flow,
Inlet Mode: "recirc", $d/W = 0.186$, $90^\circ < \theta < 200^\circ$

Figure 4.33 shows the relative flow at $200^\circ < \theta < 310^\circ$. As shown, incidence values near $\theta = 200^\circ$ (patch of light region) are high, and are consistent with those shown in figure 4.32. It can be seen that incidence becomes more conducive to efficient flow with increasing θ . Particle path lines indicate good throughflow in blade passages at values greater than $\theta = 270^\circ$. The effect of this is most noticeable in the volute flow. In contrast to the previous figures, the relative flow in the volute is less chaotic and more stream-like. (note: the dark section is caused by the tank support structure impeding the optical path). The particle traces indicate that the high kinetic energy at the impeller periphery is being diffused upon mixing with the volute flow.

The final figure in this sequence, figure 4.34, shows the flow at $270^\circ < \theta < 20^\circ$. The cutoff is at the upper left corner, and the discharge is at bottom center. High incidence is traced by the particles; however, it appears that the incidence does not directly correlate with extensive blade suction side flow separation, as found in previous cases. Aerodynamic theory suggests that, among other phenomenon, flow separation will occur when fluid particles negotiate an adverse pressure gradient. Particle streak data indicate high incidence, but little blade separation. Therefore, the flow in this region of the volute may be passing through a favorable pressure gradient.



Figure 4.33 Visualization of the Relative Flow,
Inlet Mode: "recirc", $d/W = 0.186$, $200^\circ < \theta < 310^\circ$

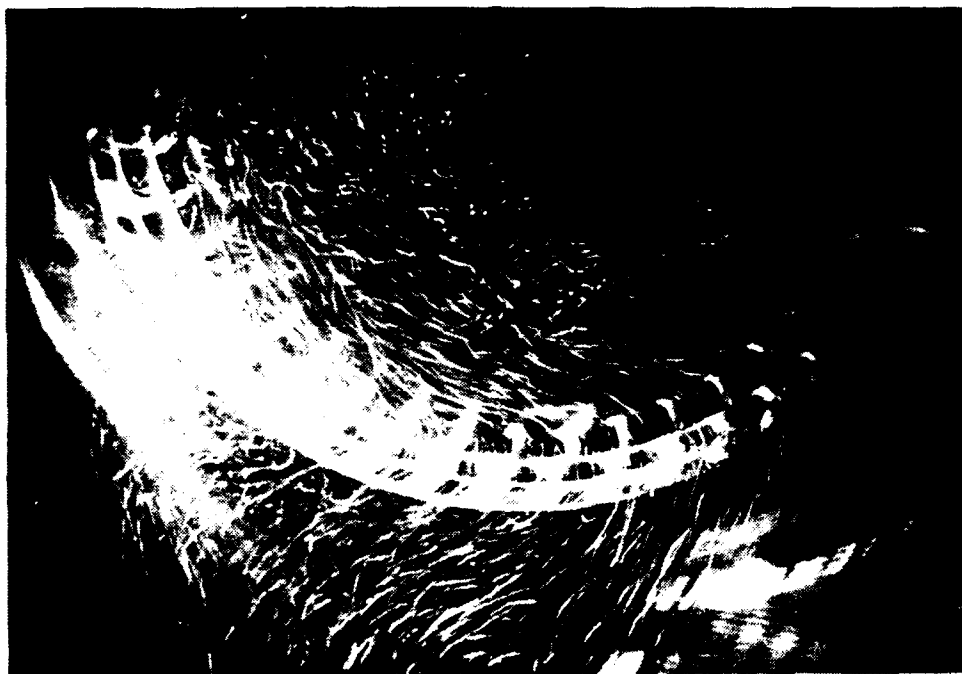


Figure 4.34 Visualization of the Relative Flow,
Inlet Mode: "recirc", $d/W = 0.186$, $270^\circ < \theta < 20^\circ$

The relative flow as visualized through the particle imaging and derotator technique at axial location $d/W = 0.372$, "recirc" mode is shown in the next sequence of figures. These photographs were taken with the camera exposure set at $1/8$ s. The bright patch of light is at circumferential location, $\theta = 220^\circ$.

Figure 4.35 shows the relative flow in the cutoff region. Directly at the cutoff, slightly LOC, several flow structures are present. The flow over the hub indicates high incidence which correlates with blade stall. The relative volute flow appears chaotic and turbulent. Particle streak data near the 4th through 6th (clockwise) blade passage indicate some type of flow anomaly. This local disturbance is believed to be indicative of re-entrant flow.

Figure 4.36 shows the relative flow paths of the region $45^\circ < \theta < 180^\circ$. As shown, the flow enters the blade passages with high incidence which correlates with suction side flow separation. The volute flow is characterized by the "jet-wake" flow structure typical of centrifugal impellers. The relative flow over the hub appears to emanate from a non-central location.

Figure 4.37 shows the relative flow in the region $90^\circ < \theta < 220^\circ$. The bright patch found at the right side of the photograph is the result of a small laser beam directed at $\theta = 220^\circ$. Again, high incidence correlates with extensive flow separation within the blade passages. As in figure 4.36, the jet-wake flow structure is an integral part of the volute flow.

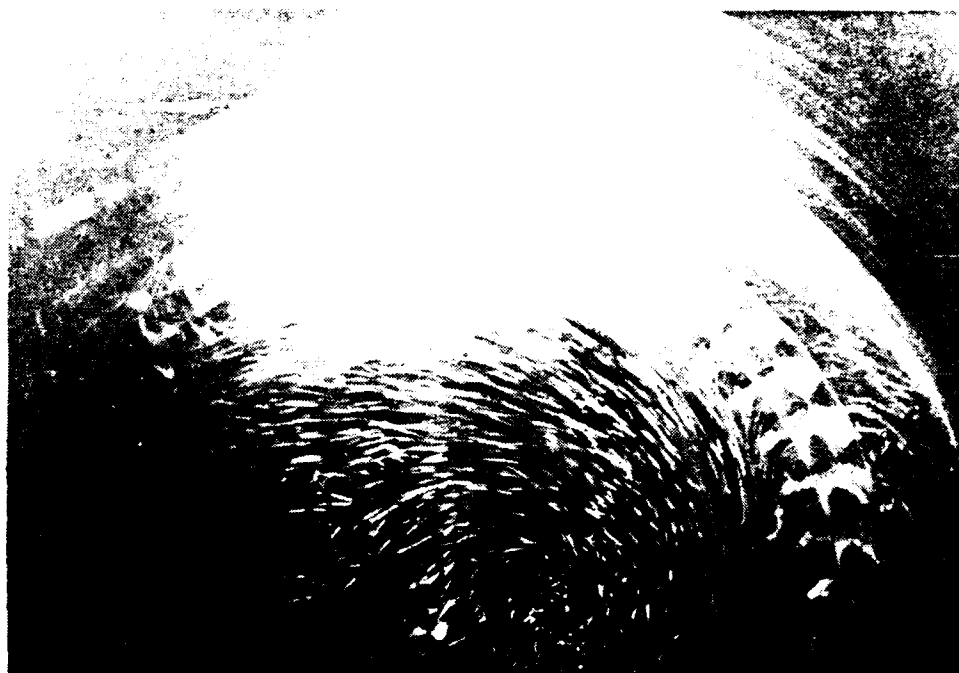


Figure 4.35 Visualization of the Cutoff Relative Flow
Inlet Mode: "recirc", $d/W = 0.372$

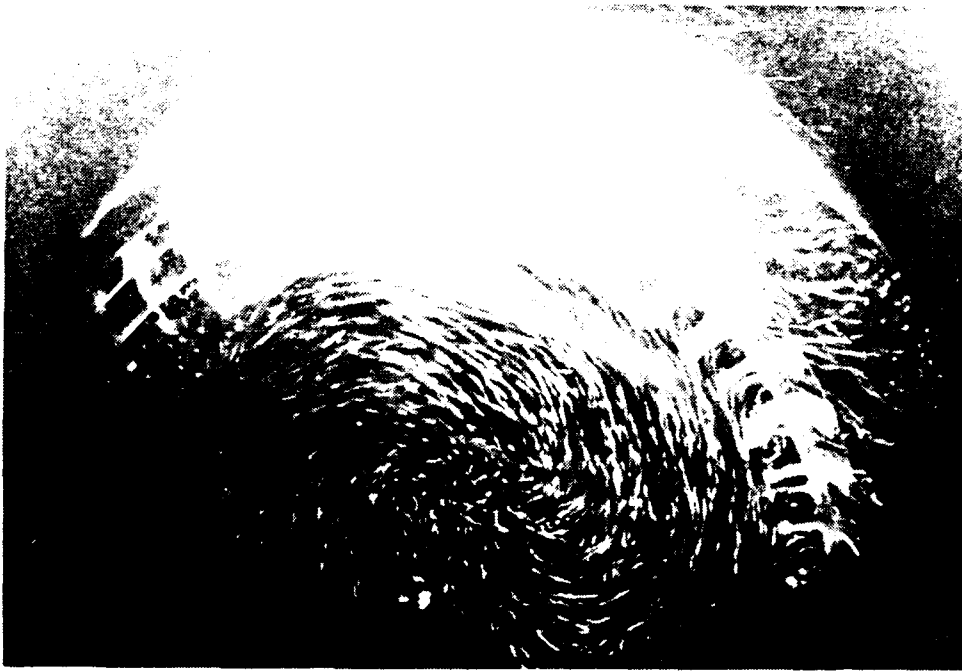


Figure 4.36 Visualization of the Relative Flow,
Inlet Mode: "recirc", $d/W = 0.372$, $45^\circ < \theta < 180^\circ$

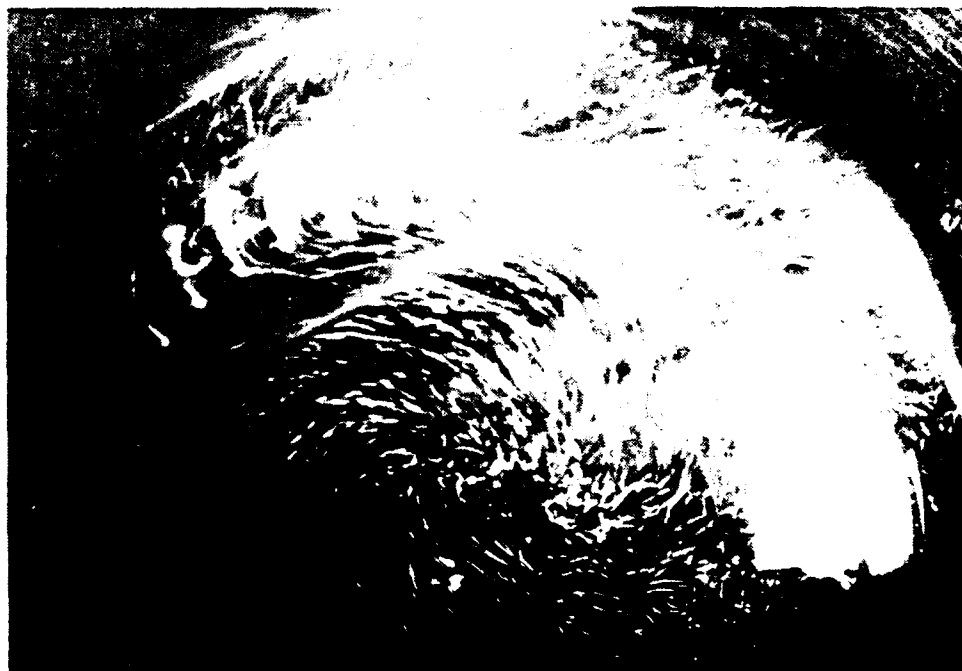


Figure 4.37 Visualization of the Relative Flow,
Inlet Mode: "recirc", $d/W = 0.372$, $90^\circ < \theta < 220^\circ$

Figure 4.38 shows the relative flow of the region $180^\circ < \theta < 325^\circ$. Particle path lines indicate that the flow over the hub has two distinct features. Right of center, the hub flow appears to have no obvious direction. This may be indicative of a rotating stall cell. Left of center, the hub flow appears to consist of fairly uniform, streamline movement. As shown, incidence angles clearly vary with circumferential location. The influence of the varying incidence angle is realized through comparison of the center and LOC blade passage flow. Extensive separated flow characterizes the center passages, while LOC passages contain more streamline flow.

The final figure in this sequence, figure 4.39, shows the relative flow at the blower discharge. Similar to previous figures, the jet-wake flow structure is present in the volute flow and varying incidence angles coincide with varying blade performance.

Figures 4.40 and 4.41 are plots of incidence angle as a function of angular distance from cutoff. This information was manually extracted from figures 4.20-4.39 and are believed to be $\pm 5^\circ$ accurate. Nonetheless, these plots are intended to provide the incidence trends a given blade would be subject to as it rotates in the volute. Incidence values of 90° indicate no throughflow was visualized by the technique. The trend lines are third order least square fits. Sharp incidence values should be considered as local instabilities rather than large measurement errors. By definition, the incidence is the angle the relative flow makes with the camber

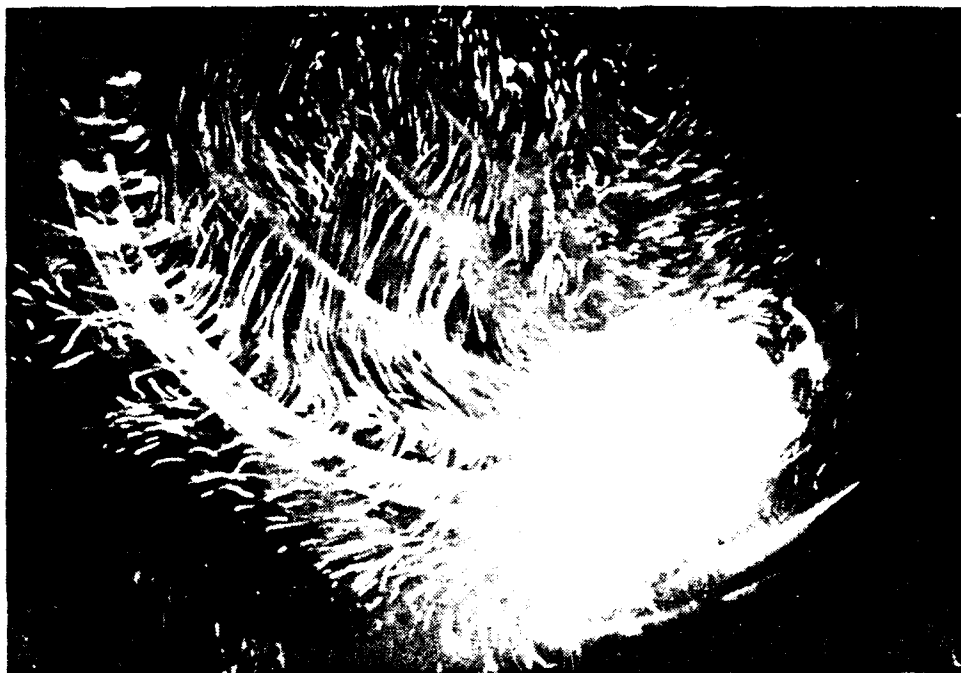


Figure 4.38 Visualization of the Relative Flow,
Inlet Mode: "recirc", $d/W = 0.372$, $180^\circ < \theta < 325^\circ$

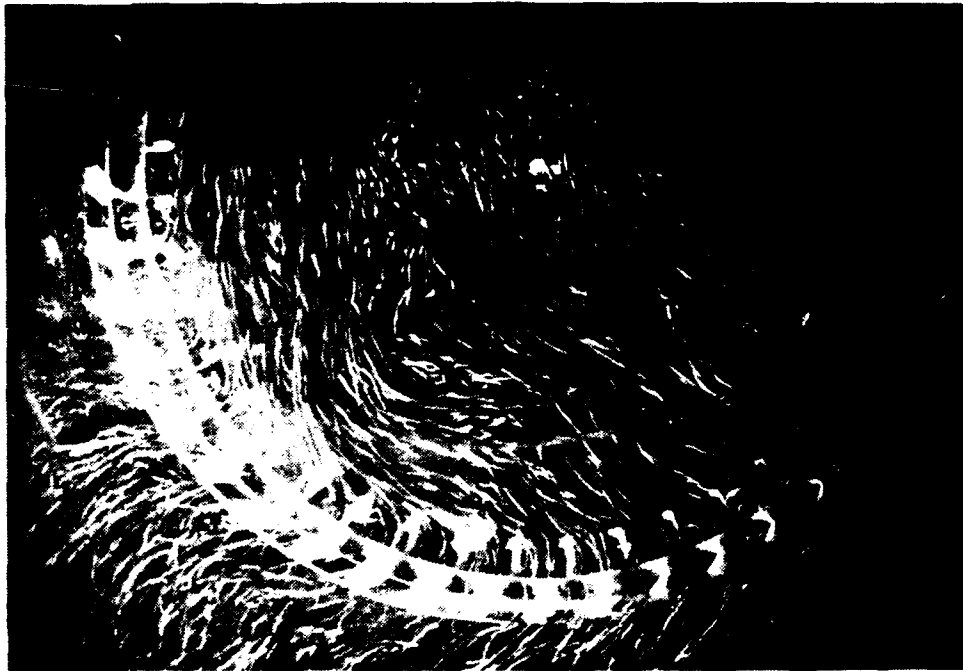


Figure 4.39 Visualization of the Discharge Relative Flow,
Inlet Mode: "recirc", $d/W = 0.372$, $90^\circ < \theta < 220^\circ$

line of the blade at the leading edge. The data for each condition were taken from one sequence of photographs rather than averaging values from several sequences. Because of the unsteady nature of the interior impeller flow field, it is believed that one sequence provides a better understanding of typical flow variations the blades experience during one revolution.

Figure 4.40 shows data obtained from photographs of the relative flow with the inlet condition set at "recirc". The incidence decreases with increasing angular distance, and always has a value greater than 20° . As shown, typical values from axial location $d/W = 0.372$ are less than those for $d/W = 0.186$. Average incidence values over one rotation for both conditions are approximately 46° (not including 90° values).

With the "fresh" inlet mode, the incidence variations are greater, as shown by figure 4.41. The 90° incidence values from $0^\circ < \theta < 150^\circ$ indicate that no flow was visualized through the blade passages. The data for $d/W = 0.372$ shows that the incidence at this location varies locally, due to the unsteady nature of the blade inlet flow. Average values for $d/W = 0.186$ and 0.372 are 56° and 46° , respectively.

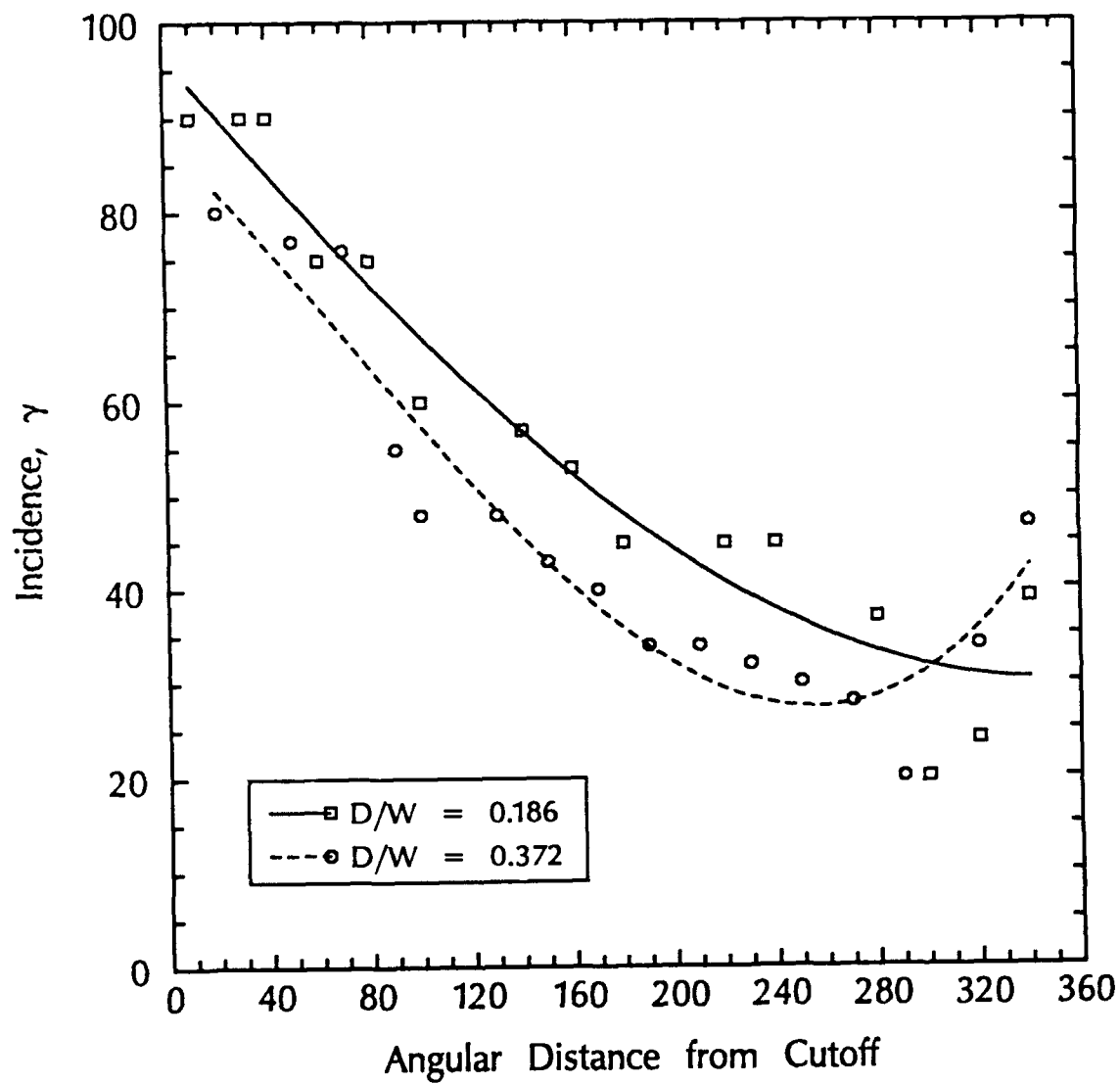


Figure 4.40 Circumferential Variation of Incidence Angle
Inlet Mode: "recirc"

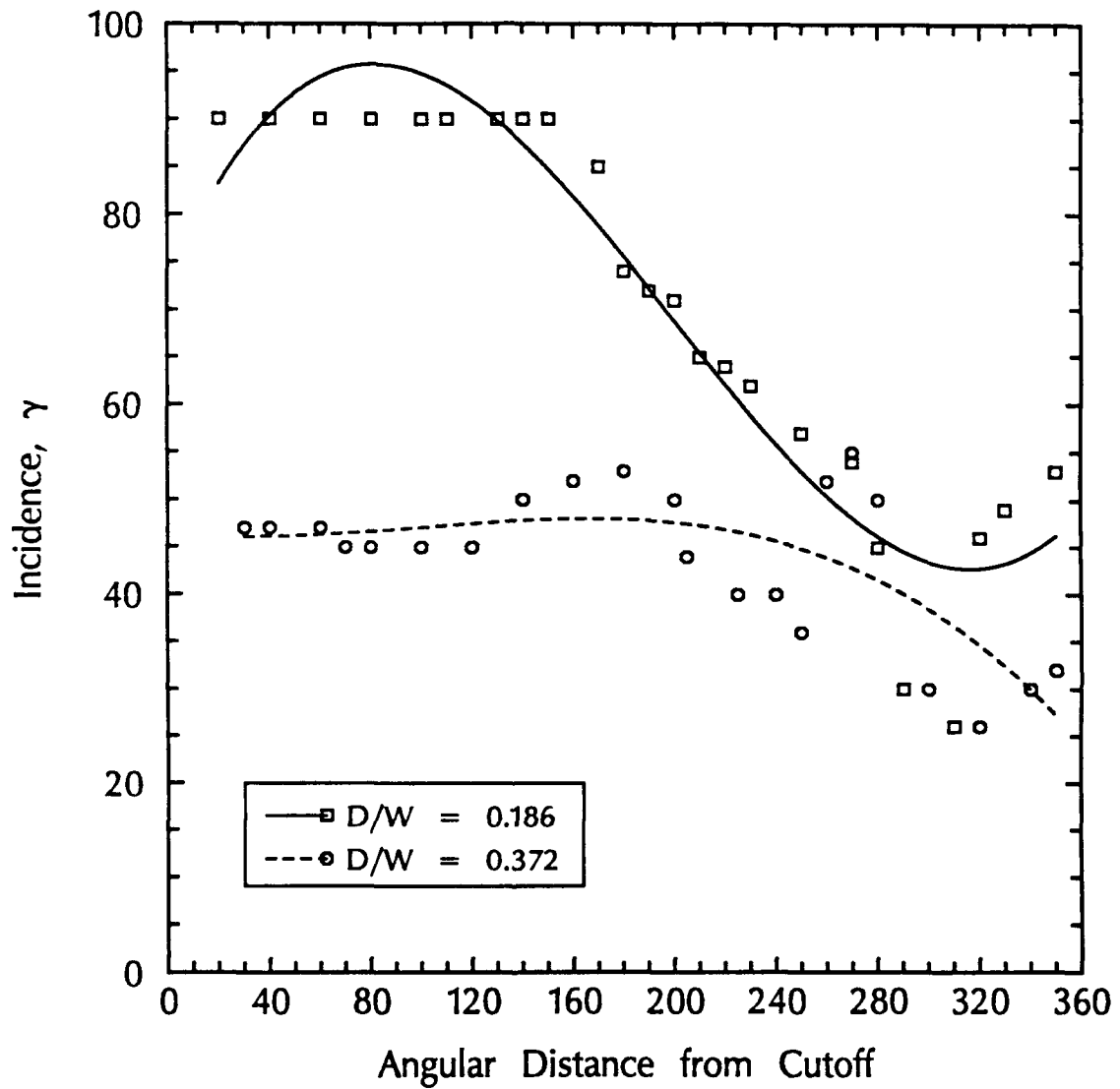


Figure 4.41 Circumferential Variation of Incidence Angle
Inlet Mode: "fresh"

Chapter 5

CONCLUSIONS

A systematic approach to determining the flow physics of an automotive heating, ventilating and air conditioning system was conducted. Both qualitative and quantitative experiments were conducted in order to provide comprehensive information about the flow mechanisms within the system. Dye flow visualization in a transparent automotive heating, ventilating, and air conditioning system determined inefficient flow regions within the ductwork. A particle tracking flow visualization study provided a method to acquire qualitative and quantitative information about the flow field of a typical forward-curved centrifugal impeller.

The dye visualization and particle visualization experiments were conducted in optically transparent test models which were mounted in a transparent plexiglas water tank. Dynamic and geometric similarity was maintained between air and water flow through Reynolds number scaling and pump flow modelling techniques. Due to the change in working fluid, lower model velocities were obtained in maintaining dynamically similar flow. The lower fluid velocities created an environment in which various flow visualization and data acquisition techniques could be implemented to identify and quantify the flow fields.

Dye visualization studies of the internal flow within the automotive heating, ventilating, and air conditioning system ductwork indicated a highly complex flow field. Sudden area

expansions, structures jutting into the flow path, and 90° bends created significant flow separation zones. Further, the dye visualization technique allowed identification of stagnant flow areas, shear layers and vortex shedding. Together, these flow structures are believed to result in system noise and significant aerodynamic losses.

Through particle tracking velocimetry and the use of an optical mechanical image derotation device, this research has shown the flow within an forward-curved centrifugal impeller to be unsteady and chaotic. The flow field is comprised of a re-entrant flow structure at the cutoff, volute flow which varies circumferentially as well as in the spanwise direction, and extensive blade passage flow separation. Through particle tracking velocimetry and image processing techniques, the volute flow was shown to be largely tangential at the inlet and backplate, and more radial at midspan locations. Such results indicate that: 1) the impeller is not effectively transferring energy to the fluid at the outer axial locations, and 2) the impeller blades are non-uniformly loaded across the span. It was shown that largely tangential volute flow correlated with a re-entrant flow structure at the cutoff. No re-entrant flow was documented for axial locations at which radial flow velocities were high. This result indicates that the radial velocity component of the volute flow field is a key element to blower performance.

The spanwise dependence of the flow in the $R-\theta$ plane indicates

that the impeller blades are not uniformly loaded across the span. This result is in agreement with previous work in which results indicate an "inactive" flow zone through the blade passages near the inlet, and higher through-flow near the blade root. Non-uniform spanwise blade loading is believed to be a contributing factor to low impeller efficiency.

Qualitative blade passage flow data obtained through the use of an optical mechanical image derotation device showed that the near inlet relative flow over the impeller hub created high angles of attack which varied with circumferential position. This characteristic of the flow was observed when operating the blower at either the "fresh" or "recirc" inlet mode. In a large portion of the impeller, high incidence angle correlated with complete blade passage flow stall. However, high incidence did not correlate with stall for blade passages near the volute discharge. Several conclusions may be drawn from this result. First, more energy is being transferred to the fluid near the discharge due to more efficient blade passage flow and lower head losses incurred by flow separation. As a result, a jet-wake flow structure characterized the near-impeller volute flow in this region. Second, the lack of flow separation indicates the fluid is not passing through an adverse pressure gradient, as might be the case in other regions. Last, the circumferential variation of blade performance indicates that the blades experience periodic loading fluctuations as they rotate in the volute. This fluctuation may induce flow noise, as

well as cause material fatigue problems.

In the absence of large disturbances, the relative hub flow appeared similar to a free vortex rotating opposite to the direction of rotation. Transient disturbances over the hub were shown to significantly affect the blade passage flow. The hub flow was also affected by the inlet condition. In the "recirc" mode, the hub flow appeared to emanate from a non-central location, presumably due to the non-axisymmetric inlet flow. Particle streaks in the volute flow indicated a high radial velocity component. The "fresh" inlet mode hub flow was shown to contain a large flow anomaly which was interpreted as a recirculating flow cell. This structure significantly affected the blade passage flow by locally altering the incidence angle.

Re-entrant flow at the cutoff was visualized for both inlet operating modes of the impeller. It was found that re-entrant flow occurs only at locations where the volute flow contained a very low radial velocity component. This flow indicates a complete flow reversal, and implies significant blade loading fluctuations.

In conclusion, analysis of the data suggests that several inefficient flow mechanisms are present within automotive heating, ventilating, and air conditioning systems. Complex ductwork and inefficient components lead to a flow field which contains poor flow areas in regard to both noise and aerodynamic performance. A large source of inefficiency and noise is the centrifugal impeller which moves the fluid. The bulk of kinetic energy transfer comes from the

root to midspan section of the impeller blades, while the inlet side of the blades operate inefficiently. This indicates that the blades are non-uniformly loaded across the span. In addition, the blades undergo periodic loading fluctuations due to the sudden area contraction zone found at the volute cutoff. Extensive unsteady blade flow separation may also be contributing to low impeller efficiencies. It is thus concluded that in order to increase automotive heating, ventilating, and air conditioning system flow performance while reducing noise generation, careful attention must be paid to the ductwork and impeller design. In particular, smoothing out sudden area contractions and sharp bends will improve noise generation and aerodynamic performance by reducing inefficient flow zones. In regard to the centrifugal blower unit, redesign of both impeller and volute is necessary to create a favorable pressure gradient for more efficient blade passage flow. More efficient flow through the impeller would result in reduced noise and higher performance.

5.1 Recommendations for Future Research

There are many areas of this research which could be extended. The strongly location-dependent impeller blade loading could be further studied by utilizing strain gauges to quantify force variations. Such experimental work would require performing measurements in the blade-fixed reference frame.

The research has shown high flow incidence to correlate with flow separation, and in some cases, blade stall. The results of this study have also shown that the impeller blades are non-uniformly loaded across the span. Redesign efforts aimed at improving the flow incidence angle, and improving span-wise blade loading would have two favorable results: a reduction in noise due to unsteady flow separation, and increased performance due to more efficient blade passage flow. Redesign of the volute casing to provide a more favorable pressure gradient may also improve blower performance.

The flow field in the ductwork of the heating, ventilating, and air conditioning system was shown to be highly complex. A systematic study to correlate noise generation to the flow structure over geometries typically found in heating, ventilating, and air conditioning systems would give designers cause-and-effect relationships which could help predict overall system noise generation.

REFERENCES

1. Osborne, W. C., Fans, New York, Pergamon Press Ltd., 1977
2. Neise, W. "Noise Reduction in Centrifugal Fans: A Literature Survey," J. of Sound and Vibration, (1976), 375-403
3. Embleton, T.F.W., "Experimental Study of Noise Reduction in Centrifugal Blowers," J. of the Acous. Soc. of America, vol. 35, 700-705, 1963
4. Stenning, A. H., "Rotating Stall and Surge," J. of Fluids Engineering, vol. 102, 14-20, Mar. 1980
5. Wright, T., Tzou, K.T.S., and Madhavan, S., "Flow in a Centrifugal Fan Impeller at Off-Design Conditions," J. of Eng. for Gas Turbines and Power, vol. 106, 913-919, Oct. 1984
6. Neise, W., "Fan Noise-Generation Mechanisms and Control Methods," Proc. of Internoise '88, Avignon, France, 30 Aug.-1 Sept., 1988
7. Neise, W., and Koopmann, G.H., "Active Source Cancellation of the Blade Tone Fundamental and Harmonics in Centrifugal Fans," Proc. of Internoise '88, Avignon, France, 30 Aug.-1 Sept., 1988
8. Lyons, L.A., and Platter, S., "Effect of Cutoff Configuration on Pure Tones Generated by Small Centrifugal Blowers," J. of the Acous. Soc. of America, vol. 35, 1455-1456, 1963
9. Raj, D, and Swim, W.B. "Measurements of the Mean Flow Velocity Fluctuations at the Exit of an FC Centrifugal Fan Rotor," ASME Symposium on Measurement Methods in Rotating components of Turbomachinery, (1980), p.43
10. Yeager, D.M., Measurement and Analysis of the Noise Radiated by Low Mach Number Centrifugal Blowers, PhD. Thesis, The Pennsylvania State University, Aug., 1987
11. Goulas, A., and Mealing, B., "Flow At The Tip Of A Forward Curved Centrifugal Fan," ASME Paper No. 84-GT-222, 1984
12. Kind, R.J., and Tobin, M.G., "Flow in a Centrifugal Fan of the Squirrel-Cage Type," ASME J. of Turbomachinery, vol. 112, 84-90, Jan. 1990
13. Cau, G., Mandas N., Manfrida, G., and Nurzia, F., "Measurements of Primary and Secondary Flows in an Industrial Forward-Curved Centrifugal Fan," J. of Fluids Engineering, vol. 109, (1987), 353-358

14. Stinebring, D.R., and Treaster, A.L., "The use of Fluorescent Mini-Tufts For Hydrodynamic Flow Visualization," Tech. Mem., ARL/PSU, Jan. 29, 1980
15. Wright, T., Madhaven, S., and DiRe, J., "Centrifugal Fan Performance with Distorted Inflows," J. of Eng. for Gas Turbines and Power, vol. 106, 895-900, Oct. 1984
16. Wright, T., Tzou, K.T.S., and Madhaven, S., "Flow in a Centrifugal Impeller at Off-Design Conditions," ASME Paper No. 82-GT-182, Oct. 1984
17. Senoo, Y., and Ishida, M., "Pressure Loss due to the Tip Clearance of Impeller Blades in Centrifugal and Axial Blowers," J. of Eng. for Gas Turbines and Power, vol. 108, 32-37, Jan. 1986
18. Wright, T., Tzou, K.T.S., Greaves, K.W., and Madhaven, S., "The Internal Flow Field and Overall Performance of a Centrifugal Impeller--Experiment and Prediction," ASME Paper No. 82-JPGC-GT-16, Oct. 1982
19. Whirlow, D.K., Goldschmied, F.R., and Farn, C.L.S., "Analysis of the Three-Dimensional Potential Flow of Centrifugal Draft Fans," EPRI Symposium on Power Plant Fans, EPRI Publication CS-2206, Oct. 1981
20. Swift, D.W. "Image Rotation Devices- A Comparative Survey," Optics and Laser Technology, 175-187, Aug. 1972
21. Shepherd, D. G. Principles of Turbomachinery. Toronto, Canada Cullier-Macmillan Canada Ltd., 1971
22. Shames, I.H., Mechanics of Fluids, New York, McGraw-Hill Book Company, 1962
23. Streeter, V. L., Fluid Mechanics New York, McGraw-Hill Book Company, 1962
24. Bruce, Edgar P., "The Design and Evaluation of Screens to Provide Multi-Cycle 20% Amplitude Sinusoidal Variations in the AFRF Rotor Inlet Axial Velocity Component," Applied Research Laboratory Internal Memorandum, File No. 74-16, Jan. 8, 1974
25. Treaster, A. L., and Yocum, A.M. "The Calibration and Application of five Hole Probes," ARL, ISA Transactions, vol. 18, no. 3, (1979)
26. Gharib, M., and Wilert, C. "Particle Tracing Revisited," AIAA paper 88-3776-cp, ND

27. Adamczyk, A.A, and Rimai, L., "2-D Particle Tracking Velocimetry (PTV): Technique and Image Processing Algorithms," Exp. in Fluids, vol. 6, 373-380, 1988
28. Yoshinaga, Y., Gyobu, I., Mishina, H., Koseki, F., and Nishida, H., "Aerodynamic Performance of a Centrifugal Compressor with Vaned Diffusers," J. of Fluids Engineering, vol. 102, 486-493, 1980
29. Merzkirch, W Flow Visualization, second edition New York, Harcourt Brace Jovanovich, 1987
30. Chang, P., "Separation of Flow," J. Fluids for Industry, Dec. 1961, 433-448
31. No Author, "The Use of Fans and Blowers and a Study of Noise in Air Moving Systems," Torin Corp. U.S, Torrington , Conn
32. Raj, D., and Swim, W.B. "Noise Generation in FC Centrifugal Fan Rotors," ASME, Fluid Trans. and Acs in the Power Industry, 289-299, n.d.
33. Paone, N., Riethmuller, M. L., and Van den Braembussche, R. A., "Experimental Investigation of the Flow in the Vaneless Diffuser of a Centrifugal Pump by Particle Image Displacement Velocimetry," Exp. in Fluids vol. 7, 371-378, 1989

Appendix A

UNCERTAINTY CONSIDERATIONS

The intent of the following sections is to provide an estimate of some of the uncertainties in the particle tracking technique. The effect of non-neutrally buoyant seed particles is examined first, followed by photographic and digitization uncertainties.

A.1 The Effect of Gravity on Velocity Measurements

To express the velocity variation due to gravity acting on a non-neutral particle, a free body analysis must be performed. The three forces acting on a seed are buoyancy, drag, and gravity. A free body diagram allows a relationship between the three:

$$F_B + F_D = F_G \quad (A.1)$$

The buoyancy force is proportional to the mass of the displaced fluid, while the gravitational force is proportional to the mass of the particle. As an estimate for drag on a sphere at low Reynolds' number, Stokes suggested:

$$F_D = 3\pi\mu V_{term}D \quad (A.2)$$

These forces may be manipulated to give an expression for the terminal velocity a particle may attain in a quiescent medium:

$$V_{\text{term}} = \frac{(\gamma - 1)gD^2}{18\nu} \quad (\text{A.3})$$

Where γ is specific gravity of the particle. Thus, for particles with a specific gravity of 1.02 seeding water at 20°C the terminal velocity is 0.0027 m/s. This constitutes only a .5% variance in a flow field with velocity magnitudes around 50 cm/s. Using the terminal velocity to determine Reynolds' number yields a value of 0(1), which justifies the stokes drag approximation.

A.2 Particle Response Time

Merzkirch [29] gives the response time of a seed particle as

$$\tau_p = D^2/18\nu \quad (\text{A.4})$$

For a seed diameter of 375 microns (average), determination of equation A.4 gives $\tau_p = 0.0078\text{s}$. In the particle tracing experiment, the primary fluid driving force operates at the blade passing frequency. Therefore, the characteristic time interval of the flow, τ_f , would be determined by:

$$\tau_f = 1/\#\text{blades} * \Omega \quad (\text{A.5})$$

At 22rpm, $\tau_f = 0.0099$. Because $\tau_p < \tau_f$, the error involved with particle response time is assumed small.

A.3 Image Acquisition Error

Errors in velocity vector position and magnitude arise due to non-orthogonal orientation of the optical path (from CCD camera) and laser light sheet, and optical aberrations within the camera lens. The error involved with lens aberrations is presumed small. Error due to positioning would be determined by:

$$E_{\text{camera}} = 1 - \text{abs}|\sin(\alpha - 90^\circ)| \quad (\text{A.6})$$

Alpha would be the angle between the CCD optical path and the LLS. Determination of A.6 for a 5° camera placement error gives an error less than 0.5% in velocity magnitude.

A.4 Image Processing Error

The filters applied to each image during the image processing data acquisition routine are a probable source of error. The error occurs when the processed particle trace is either larger or smaller than the original. The frame grabber had a 640 x 512 resolution and

for the duration of the experiment, had a 13 cm by 13 cm field of view (typical). Thus, a 1cm trace running parallel to the frame grabber's lowest resolution axis would contain 40 pixels along the longest length. On average, particle streaks were .7 cm in length, or 30 pixel units. The error due to an extra pixel about the periphery of a trace would be determined by:

$$E_{\text{trace}} = 2*75*(\text{pixels to cm calibration}) \quad (\text{A.7})$$

The factor of 75 corresponds to the chopper speed which is essential to velocity determination, the factor of 2 corresponds to the additional pixels at the trace periphery, and the calibration is image-dependent. For the above example, determination of A.7 amounts to 3.81 cm/s, or 7% of the tip velocity.

The Pennsylvania State University
Applied Research Laboratory
P.O. Box 30
State College, PA 16804